Distributed Excitations of Pulsed Photo-Conductive Sources: The Time Domain Analysis

Msc. Graduation Thesis

Laurens Faizal Elias Beijnen

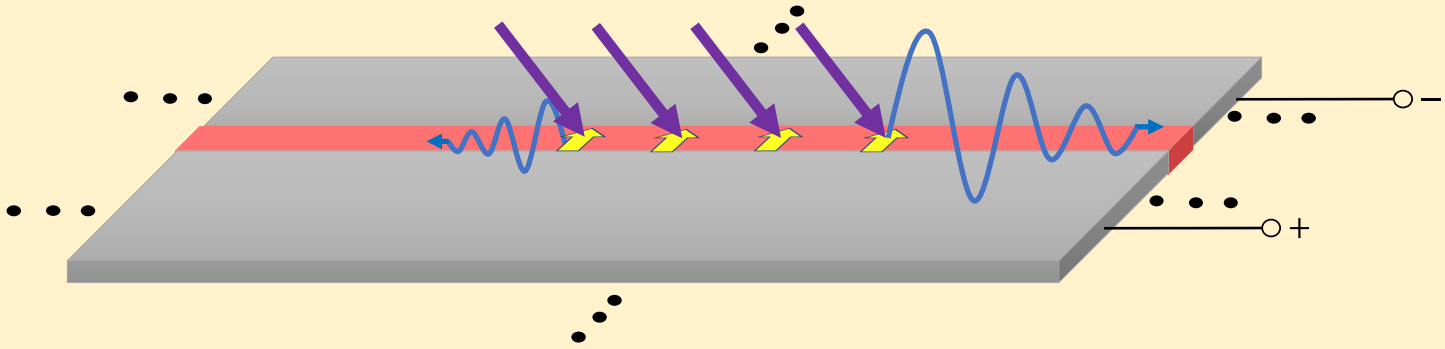

THz Sensing Group

TU Delft

Distributed Excitations of Pulsed Photo-Conductive Sources: The Time Domain Analysis

Msc. Graduation Thesis

by

Laurens Faizal Elias Beijnen

To obtain the degree of Master of Science,
at Delft University of Technology,
to be defended publicly on the 10th of November, 2023.

Project duration: September 2022 – October 2023
Thesis Committee: A. Neto, N. Llombart, A. Adam

Abstract

Distributed feeding in photo-conducting antennas (PCAs) leads to simple optical designs, less prone to overheating, as well to terahertz (THz) antennas that can operate non-dispersively over wide bandwidths. However, the efficient analysis of pulsed PCAs was so far limited to architectures characterized by feeds small with respect to the THz wavelengths. In this thesis, an efficient and rigorous procedure for the time domain analysis of an infinitely long slot antenna printed on photo conductive material and excited by a distributed pulsed laser is presented. The procedure is electromagnetically rigorous, and relies on spectral representations of the fields in both the frequency and spatial domains.

Acknowledgements

A journey this has been. Among others, it has been one of surprises, laughter, pondering and insights. I'm grateful for this period in which I got to learn so much. Without the people around me, the journey would have been much less pleasant. First of all, I want to thank mom and dad, my sisters Usha and Elisabeth, grandma and auntie Grace. You were there from the very beginning and have provided me with honesty, care and many memorable moments. I'm happy to have you in my life. I cannot forget about my dear nieces Mia and Lily. Seeing you grow and moving through life with the purest form of joy is truly something special. Also, I would very much like to thank my friends and other family members with whom I can have lots of fun but also reflect on what is going on in our lives in a safe space. May we continue to do so as long as we can, in good health.

This work would definitely not be anywhere near the level it is without my supervisor Andrea Neto. Thank you so much for all the meetings, sharing your experiences, laughter, advice and your immense amount of enthusiasm. I'm sure you will continue to inspire me in the future. I would also like to thank the other members of the photoconductive team, Nuria, Juan, Paolo, Martijn and Huasheng, for welcoming me with open arms, for the discussions and for helping me whenever I had questions. Many thanks as well to the office mates with whom I started this journey, Alexandros, Alexandra and Robbin, for making the days much more enjoyable. Finally, I would like to thank the entire THz Sensing Group for providing a warm, inspiring, fun atmosphere during this period. I'm lucky to be in your presence.

Laurens
Delft, October 2023

Contents

Chapter 1

Introduction

1.1 THz Systems

Over the past years the interest of researchers and industry in the emergence of terahertz (THz) technology has emerged. In the future the use of THz waves will certainly allow extremely high data rates in communication [1]. But already now the THz range has a special place in the spectrum due to the wide range of applications in non-destructive testing. Namely, the latter have been found in spectroscopy, security screening and imaging [2–5]. The wide bandwidth makes THz systems an excellent candidate for high-resolution imaging. For instance applications have been found in the quality-control of products for the pharmaceutical industry [3]. Also, the difference in response from multiple types of tissue to THz radiation provides useful criteria in medical diagnostics [4]. Finally, the spectral selectivity of materials is also useful for food inspection and the study of molecules [5]. Many of these applications rely on photoconductive antennas (PCAs) to generate the required THz waves. The basic working principles of photoconductive antennas will be elaborated upon in the next section.

1.2 Basic Working Principles of Photoconductive Antennas

Photocondcuctive antennas are based on the following principle which is illustrated in Fig. 1.1. A photoconductive material is placed within an antenna (e.g. the slot in Fig. 1.1) which is biased with a voltage, V_b. Initially, the material is not conductive and therefore no significant amount of current is flowing through it. Subsequently, a pulse of optical light illuminates the material. If the frequency of the light is appropriate, some of the energy from the pulse gets absorbed by the material and contributes to the promotion of electrons from the valence band to the conduction band. The concentration of electrons in the conduction band rises to a level proportional to the laser power and the material effectively becomes conductive. Therefore, a current can flow in the direction determined by the bias. However, due to the recombination of the promoted electrons, the material is only temporarily conductive. For photoconductive antennas, the material properties are such that the time-scale of the current is measured in picoseconds. Thus, the current acts as a source of THz radiation to be guided outward by the antenna. If the structure under investigation is a guiding one, the current can also act as a source of waves propagating within a confining structure (for example the voltage waves in Fig. 1.1).

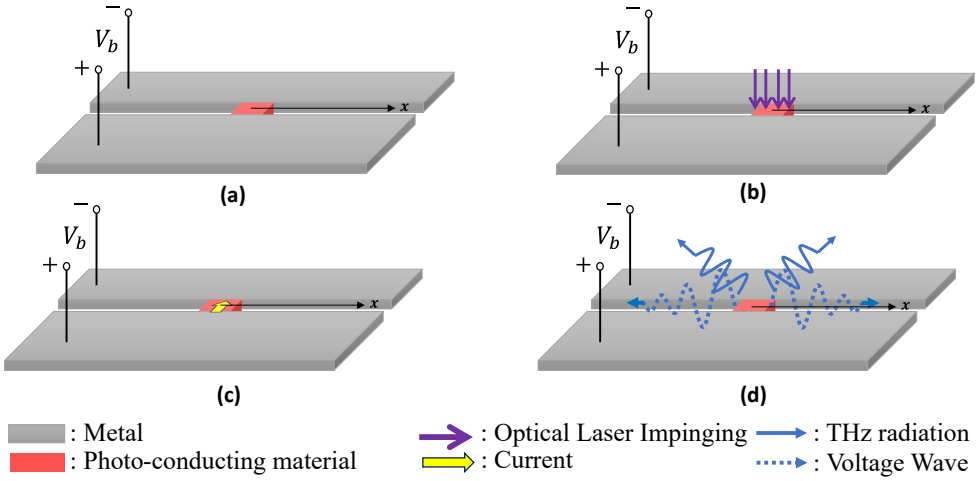

Figure 1.1: Basic working principle of photoconductive antennas. (a) Photoconducting material is placed within an antenna (in this case a slot) in which it is biased with a voltage V_b. (b) The material is excited with an optical laser, (c) which induces a current along the direction indicated by the bias. (d) This current acts as a source for THz radiation and guided waves in the structure.

1.3 State-of-the-Art in Photoconductive Antennas

1.3.1 Focused vs non-focused Excitation

Modelling of photoconductive antennas where an electrically small volume of photoconductive material is excited has seen quite some progression over the recent years. Several equivalent circuits have been proposed to describe the interaction between the photoconductive source and the antenna [6]. Unfortunately all attempts before 2020 include generators to be tuned by means of experiments, in order to provide accurate results. The first rigorous, electromagnetic derivation for the accurate characterization of pulsed photoconducting sources in comparison with the measurements, was developed in [7] and [8]. The circuit in [8] in fact solely consists of physical parameters of the system. A particularly striking aspect of [8] was the capacity to model a saturation effect typically seen in photoconductive antennas. At low power levels, the intensity of the THz pulse is proportional to the optical power incident on the material. However above a certain threshold, the intensity of the THz pulse radiated is known to saturate. Another advantage of the method described in [7] is its flexibility with respect to the type of antenna which is used, since the equivalent Norton generator it exploits can be connected to an arbitrary input impedance. This property shall be used extensively in this work. Furthermore, the circuit from [8] can even be applied to characterize a link between two photoconductive antennas as demonstrated in [9]. In this work the attention will be moved to the use of leaky wave supporting slotted structures as antennas [10, 11]. Fig. 1.1, shows a focused, lumped excitation on such slotted structure. It naturally excites two waves. One regressive wave moving to the left and one progressive wave moving to the right with respect to the feed. Since in most applications only one beam is desired, one can assume that any energy which is not directed toward a single predefined direction is effectively lost. To solve this problem, in practical realizations of these structures at microwave frequencies, either the effective useful bandwidth was sacrificed, [12] or, as in [13], a single beam was acquired by a fairly complex non-planar development of the ground plane. In this thesis, one of the main design goals was the efficient excitation of ultra short pulses by means of planar PCA slots. To this goal the distributed excitation of slots will be investigated.

For narrow band photo-mixing in [14], the authors successfully demonstrated that a distributed excitation over a coplanar waveguide (CPW) would give rise to the excitation of only the progressive CPW THz mode. This concept can also be applied to pulsed, photoconductive sources, as it will be clarified in this work. Specifically, one can obtain a single leaky wave beam, if the slot radiating structure is excited over an electrically long region.
Another reason to study in detail distributed PCA sources is that the excitation of electrically long photoconductive material regions has already been reported on numerous occasions. See for example [15], [16], [17] and [18]. However, a rigorous analysis of photoconductive antennas with a distributed excitation, has not been provided yet.

1.4 Scope of the Thesis

The work presented in this thesis is dedicated to the analysis of photoconductive slot antennas which are excited over a distributed region that can be electrically long. To arrive to that final goal, a few steps have to be taken. Multiple geometries shall be studied via rigorous marching-on-in-time procedures which allow one to observe the evolution over time of electric currents and electric field distributions. First, the case of an infinite slot which is excited by an electrically small photoconducting volume is discussed in Chapter 2. The procedure presented here is similar to the one investigated in [7], however, for the first time the results presented here explicitly take into account the fact that the input impedance of a realistic slot is variable in frequency. Accordingly, the time dependent contribution of the slot antenna Green's function is not approximated with a delta of Dirac as was implied in [7]. Secondly, in Chapter 3 findings on the interaction between two separated, electrically small photoconducting volumes within the slot are presented. The influence of the distance and the voltage wave time-of-arrival which respect to the time-varying conductivities will be discussed. In both Chapter 2 and 3, the relation between propagation of the guided mode in the slot and an associated transmission line equivalent circuit shall be explained. Finally, in Chapter 4 the formulation is extended to an infinite slot entirely filled with photoconducting material, which is excited over an electrically large region. In that Chapter one shall see how to effectively excite only the progressive THz wave. A summary of the findings and conclusions, together with recommendations for future work, is then presented in Chapter 5.

Chapter 2

Slot Antenna Fed by a Single Pulsed Photo Conducting Source

2.1 Formulation

2.1.1 Defining the Problem

Consider an infinite slot with a width W_y between two semi-infinite, non-magnetic, homogeneous media. "Medium 1" ($z < -W_z$) and "medium 2" ($z > 0$) have a relative permittivity of $\varepsilon_{r,1}$ and $\varepsilon_{r,2}$, respectively. A photoconducting gap is placed at the center of the slot with length equal to Δ and depth W_z. The structure is depicted in Figure 2.1. The gap is activated by an optical, pulsed laser that frees charged carriers. These carriers constitute a current along $\hat{y}$ because of the acceleration induced by the bias voltage V_b. In this chapter, the objective is to determine the induced voltage in the photoconducting gap, $v(t)$, as well as the voltage at all other positions along the slot, represented by $v(x,t)$.

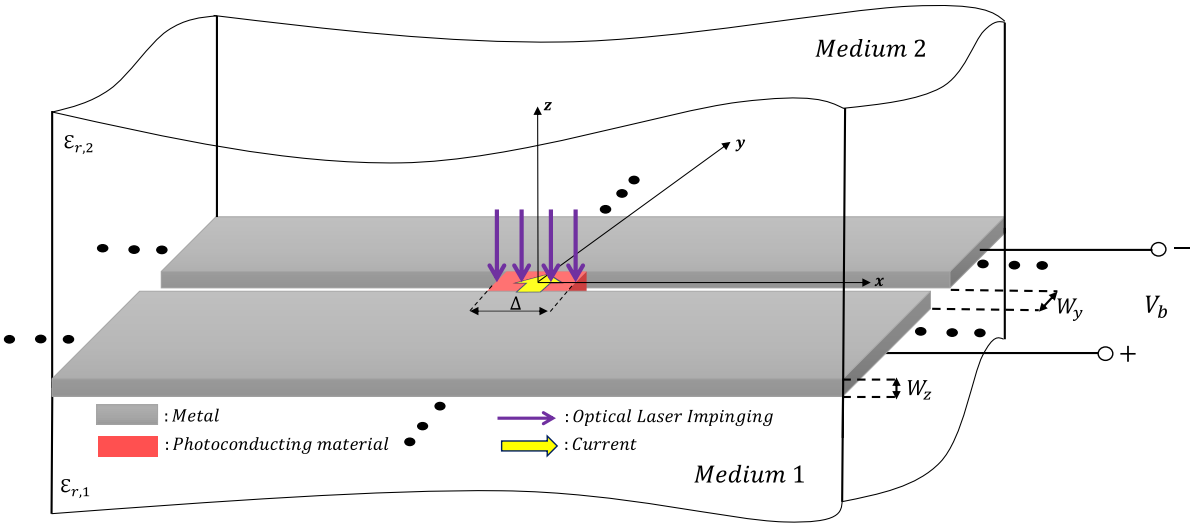

Figure 2.1: Infinite slot between two semi-infinite media with photoconducting material placed in the center. The photoconducting material has a length equal to Δ and depth W_z. Furthermore, the slot has a width W_y and it is biased with a constant voltage equal to V_b. The photoconducting gap is activated by an optical, pulsed laser. Adapted from [10].

As was shown in [7] and [8], the current flowing through the photoconducting gap (yellow arrow in Figure 2.1) is related to the voltage across the gap, $v_g(t)$, via the following constitutive relation

$$i(t) = I_F^{iv}\{t, v_g, \tilde{P}_{opt}\} = A\frac{q_e^2}{m_{e,GaAs}}\frac{W_z \cdot \Delta}{W_y}\int_{-\infty}^{t} e^{-4ln2\frac{t''^2}{\tau_p^2}}\int_{t''}^{t} e^{-\frac{t-t'}{\tau_s}} v_g(t')dt' e^{-\frac{t-t''}{\tau_c}} dt'' \tag{2.1a}$$

$$v_g(t) = V_b - v(t) \tag{2.1b}$$

$$A = \frac{\tilde{P}_{opt}}{hf_c}\frac{T_L}{\tau_p}\sqrt{\frac{4ln2}{\pi}}\frac{1}{Vol} \tag{2.1c}$$

where $q_e = 1.602{\cdot}10^{-19}$ [C] is the electron charge, f_c the central frequency of the laser and A indicates the peak rate at which charged carriers are generated. This peak rate is obtained via averaging over the dimensions

of the photoconducting gap to remove any spatial dependence. Furthermore, $\tilde{P}_{opt}$ is equal to the average optical power absorbed in the gap. The parameters τ_p, τ_c, τ_s, $m_{e,GaAs}$, T_L and other relevant quantities are described in Table 2.1 below [8]. For the remainder of this work, unless explicitly stated otherwise, the values indicated in Table 2.1 shall be adhered to.

Table 2.1: Parameters describing the laser, dielectric media and the photoconducting gap.

Parameter	Description	Value
λ_L	Wavelength Laser	780 $[nm]$
τ_p	Laser Pulse Full-Width-Half-Maximum (FWHM)	100 $[fs]$
T_L	Laser Repetition Time	12.5 $[ns]$
$\varepsilon_{r,1}$	Relative Permittivity Medium 1	1
$\varepsilon_{r,2}$	Relative Permittivity Medium 2	11.7
τ_c	Recombination Time	300 $[fs]$
τ_s	Scattering Time	8.5 $[fs]$
$m_{e,GaAs}$	Effective Mass Electron in Gallium Arsenide	$0.067 \cdot m_e$ [kg]

The current in Eq. 2.1 can be decomposed into an "impressed current", $i_{impr}(t)$, and "internal current", $i_{int}(t)$:

$$i(t) = I_F^{iv}\{t, v_g, \tilde{P}_{opt}\} = I_F^{iv}\{t, V_b, \tilde{P}_{opt}\} - I_F^{iv}\{t, v(t), \tilde{P}_{opt}\} = i_{impr}(t) - i_{int}(t). \tag{2.2}$$

Furthermore, the current, $i(t)$, flowing through the photoconducting gap is equal to the time-varying voltage, $v(t)$, convolved [7] with the "impulsive conductance" $g_l^{imp}(t)$,

$$i(t) = \int_{-\infty}^{t} v(t') g_l^{imp}(t-t')\,dt' = v(t) * g_l^{imp}(t) \overset{\mathscr{F}}{\Longleftrightarrow} I(\omega) = \frac{V(\omega)}{Z(\omega)} \tag{2.3a}$$

$$I(\omega) \overset{\mathscr{F}}{\Longleftrightarrow} i(t),\ V(\omega) \overset{\mathscr{F}}{\Longleftrightarrow} v(t),\ \frac{1}{Z(\omega)} \overset{\mathscr{F}}{\Longleftrightarrow} g_l^{imp}(t). \tag{2.3b}$$

In Eq. 2.3, $Z(\omega)$ represents the input impedance of the slot antenna. Unlike the bow-tie studied in [8], here $Z(\omega)$ can not be approximated with a constant resistance due to the dispersivity of the slot. Also, $\mathscr{F}$ indicates the Fourier transform going to and from the time-domain and the frequency domain. Since the time-domain functions considered in this work are real the following Fourier transform pair for time and frequency shall be adhered to [19]

$$\begin{aligned} F(\omega) &= \int_{-\infty}^{\infty} f(t) e^{-j\omega t}\,dt = \mathscr{F}\{f(t)\} \\ f(t) &= Re\Big\{\frac{1}{\pi}\int_0^{\infty} F(\omega) e^{j\omega t}\,d\omega\Big\} = \mathscr{F}^{-1}\{F(\omega)\}. \end{aligned} \tag{2.4}$$

The relations presented in Eq. 2.1, 2.2 and 2.3 are compactly expressed via the Norton equivalent circuit [7] in Fig. 2.2. This circuit point of view illustrates the interaction between a photoconducting feed and the antenna in which it is placed. One can picture this interaction as a current generator that divides its current, $i_{impr}(t)$, among its generator impedance and the antenna load.

To find the input impedance of the antenna, $Z(\omega)$, one first needs to consider the following relation [20] regarding the voltage along the slot as a function of space and frequency, $V(x,\omega) \overset{\mathscr{F}}{\Longleftrightarrow} v(x,t)$:

$$V(x,\omega) = \frac{1}{2\pi}\int_{-\infty}^{\infty} \frac{I_e(k_x,\omega)}{D(k_x,\omega)} e^{-jk_x x}\,dk_x \tag{2.5}$$

where $D(k_x,\omega)$ represents the longitudinal Green's function. It is equal to the following closed-form expression [10]

$$D(k_x,\omega) = \frac{1}{2k_0\zeta_0}\sum_{i=1}^{2}(k_i^2 - k_x^2)\, J_0\Big(\frac{W_y}{4}\sqrt{k_i^2-k_x^2}\Big)\, H_0^2\Big(\frac{W_y}{4}\sqrt{k_i^2-k_x^2}\Big), \quad k_i = k_0\sqrt{\varepsilon_{r,i}}. \tag{2.6}$$

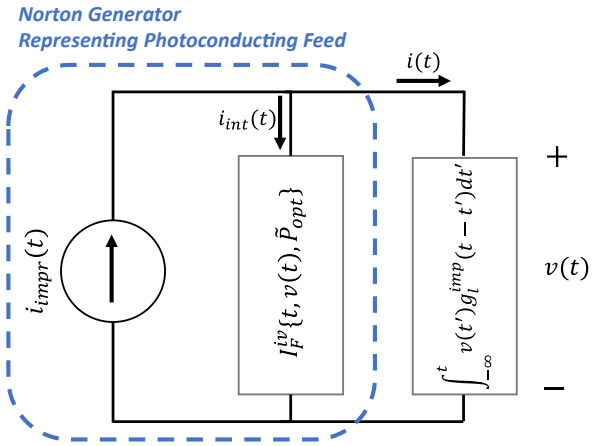

Figure 2.2: Norton equivalent circuit describing the interaction between a photoconducting feed and the input impedance of the antenna in which this feed is placed.

Furthermore, in Eq. 2.5, $I_e(k_x,\omega)$ represents the Fourier transform of the current exciting the slot, $i(t)$, divided by the length of the gap, Δ:

$$I_e(k_x,\omega) = \mathscr{F}\left\{\mathscr{F}_{spatial}\left\{\frac{i(t)\cdot rect(\frac{x}{\Delta})}{\Delta}\right\}\right\} = I(\omega)sinc\Big(\frac{k_x\Delta}{2}\Big). \tag{2.7}$$

In this chapter, spatial variations of the laser beam over a length Δ, slot width W_y and depth W_z are assumed to be small enough such that the electrons freed by optical excitation are uniformly distributed over the photoconducting gap [8]. Even though this implies a volumetric current, in this work the current distribution is considered to be planar (in the xy-plane). This is done because the formulation related to Eq. 2.5 requires a planar current distribution over x. This justifies the use of $rect(\frac{x}{\Delta})$ in Eq. 2.7, where $rect(x) = 1\forall|x| < 1/2$. Similar to $\mathscr{F}$, $\mathscr{F}_{spatial}$ indicates the Fourier transform going to and from the spatial-domain and the spectral domain. It refers to the following transformation pair

$$\begin{aligned} F(k_x) &= \int_{-\infty}^{\infty} f(x)e^{jk_xx}dx = \mathscr{F}_{spatial}\{f(x)\} \\ f(x) &= \frac{1}{2\pi}\int_{-\infty}^{\infty} F(k_x)e^{-jk_xx}dk_x = \mathscr{F}^{-1}_{spatial}\{F(k_x)\}. \end{aligned} \tag{2.8}$$

Additionally, Δ is small w.r.t. the wavelengths in the radiated THz spectrum such that spatial variations of the voltage over a length Δ are small. Therefore, the voltage induced by the activation of the photoconducting feed ($v(t)$ in Eq. 2.1, 2.2 and 2.3) can be defined as the average voltage over the gap region. Using Eq. 2.5, the average voltage in time domain can then be found as:

$$v(t) \equiv \mathscr{F}^{-1}\left\{\frac{1}{\Delta}\int_{-\Delta/2}^{\Delta/2} V(x,\omega)dx\right\} = \mathscr{F}^{-1}\left\{\frac{1}{2\pi}\int_{-\infty}^{\infty}\frac{I_e(k_x,\omega)}{D(k_x,\omega)}sinc\Big(\frac{k_x\Delta}{2}\Big)dk_x\right\}. \tag{2.9}$$

Finally, after combining the expressions given by Eq. 2.7 and 2.9, one finds the input impedance $Z(\omega)$ which is defined as the ratio of the average voltage and current [21]

$$Z(\omega) = \frac{\frac{1}{\Delta}\int_{-\Delta/2}^{\Delta/2} V(x,\omega)dx}{I(\omega)} = \frac{1}{2\pi}\int_{-\infty}^{\infty}\frac{sinc^2\Big(\frac{k_x\Delta}{2}\Big)}{D(k_x,\omega)}dk_x. \tag{2.10}$$

In Fig. 2.3, $Z(\omega)$, is shown for various combinations of Δ and W_y. In Fig. 2.3a, the input impedance is depicted for an infinite slot with $\Delta = 4.5\,\mu m$ and a width W_y ranging from $2.5\,\mu m$ to $10\,\mu m$. One can observe that with increasing width both the real and the imaginary part of the input impedance increases. In Fig. 2.3b, the width is kept at a constant $W_y = 10\,\mu m$ while Δ varies from $1.5\,\mu m$ to $4.5\,\mu m$. In this case, the real part barely changes as a function Δ while the imaginary part decreases with increasing Δ.

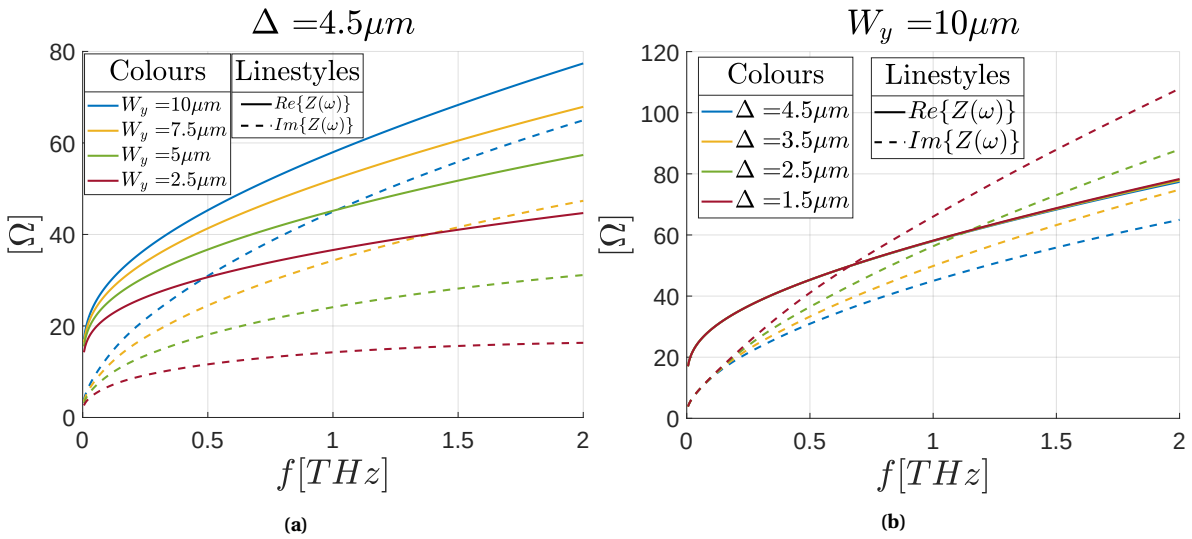

Figure 2.3: (a) Input impedance of the slot antenna for several widths W_y and (b) different lengths of the photoconducting gap Δ.

2.1.2 Voltage and Current Provided by the Source

Now that in Section 2.1.1 all relevant quantities have been described, one ought to combine Eq. 2.2 and 2.3 to obtain [7]

$$i_{impr}(t) - i_{int}(t) = \int_{-\infty}^{t} v(t') g_l^{imp}(t-t')dt' = v(t) * g_l^{imp}(t). \tag{2.11}$$

In Eq. 2.11 the voltage $v(t)$ is the unknown quantity for which the equation should be solved. As indicated in Eq. 2.1 and 2.2, the impressed current depends on the bias V_b, properties of the laser and material properties of the photoconducting gap. Since it doesn't depend on the unknown, $v(t)$, the impressed current $i_{impr}(t)$ is known beforehand. The internal current on the other hand, does depend on the time-varying voltage $v(t)$ via the constitutive relation in Eq. 2.1 ($i_{int}(t) = I_F^{iv}\{t, v(t), \tilde{P}_{opt}\}$) and is therefore not known.

Taking into account Eq. 2.3, Eq. 2.11 implies the following in the frequency domain

$$I(\omega) = I_{impr}(\omega) - I_{int}(\omega) = \frac{V(\omega)}{Z(\omega)} \tag{2.12a}$$

$$Z(\omega)I_{impr}(\omega) - Z(\omega)I_{int}(\omega) = V(\omega), \tag{2.12b}$$

with $I_{impr}(\omega) \overset{\mathscr{F}}{\Longleftrightarrow} i_{impr}(t)$ and $I_{int}(\omega) \overset{\mathscr{F}}{\Longleftrightarrow} i_{int}(t)$. To stay consistent with the methodologies adopted in subsequent chapters (the reason for this step will be elaborated upon in Chapter 3), both sides of Eq. 2.12b shall be divided by a "weighting function" $W(\omega)$

$$I_{impr}(\omega) \cdot \frac{Z(\omega)}{W(\omega)} - I_{int}(\omega) \cdot \frac{Z(\omega)}{W(\omega)} = \frac{V(\omega)}{W(\omega)}. \tag{2.13}$$

A weighting function is not unique. It only has to satisfy a few criteria as will be explained in Section 3.1.2. For Eq. 2.13, $W(\omega) = Z^2(\omega) = (Z(\omega))^2$ is chosen. It results in

$$\frac{I_{impr}(\omega)}{Z(\omega)} - \frac{I_{int}(\omega)}{Z(\omega)} = \frac{V(\omega)}{Z^2(\omega)}. \tag{2.14}$$

Performing an inverse Fourier transform on both sides of Eq. 2.14 to bring it back to the time-domain gives

$$i_{impr}(t) * h_{self}(t) - i_{int}(t) * h_{self}(t) = v(t) * h_{weight}(t) \tag{2.15a}$$

$$h_{self}(t) \overset{\mathscr{F}}{\Longleftrightarrow} \frac{1}{Z(\omega)}, \; h_{weight}(t) \overset{\mathscr{F}}{\Longleftrightarrow} \frac{1}{Z^2(\omega)}. \tag{2.15b}$$

One should note that $h_{self}(t)$ is equal to the impulsive conductance, $g_l^{imp}(t)$, and therefore represents the impulse response of the slot giving the current resultant from a voltage pulse. The next step involves applying a time-discretization to the time-domain functions involved in Eq. 2.15. Each function $f(t)$ shall be represented as follows [7]:

$$f(t) \cong \sum_{n=-\infty}^{\infty} f_n rect\Big(\frac{t-t_n}{\delta t}\Big),\ f_n = f(t_n) \tag{2.16a}$$

$$t_n = n\cdot\delta t - \frac{\delta t}{2},\ n \in \mathbb{I}. \tag{2.16b}$$

This way, a time-domain function is approximated as a summation of weighted (with weight f_n) rectangular basis functions centered around different, equally-spaced sample points t_n. As long as the time-step, δt, is sufficiently small compared to the relevant timescales (τ_p, τ_c, τ_s, decay rate of h_{self} and h_{weight}) then this is an accurate representation of the function.

In Appendix A, it is shown how after applying a time-discretization and analytically solving the inner integral, the impressed current at an observation time $t = t_m$ is found to be

$$i_{impr}(t_m) \cong A\cdot\delta t \frac{q_e^2}{m_{e,GaAs}} \frac{W_z\cdot\Delta}{W_y} V_b\cdot\tau_s \sum_{n=-\infty}^{m} e^{-4ln2\frac{t_n^2}{\tau_p^2}} \Big[1 - e^{-\frac{t_m-t_n}{\tau_s}}\Big] e^{-\frac{t_m-t_n}{\tau_c}}. \tag{2.17}$$

The expression in Eq. 2.17 allows for efficient numerical implementation. Such an implementation requires that the lower bound of the summation ($n = -\infty$ in Eq. 2.17) is taken low enough to make sure the function converges.
Furthermore, in Appendix B the continuous-time convolution (e.g. between $v(t)$ and $g_l^{imp}(t)$ in Eq. 2.11) of two signals $f(t)$ and $h(t)$, evaluated at an observation time $t = t_m$, is shown to be equal to a summation after applying time-discretization: $f(t_m) * h(t_m) \cong \delta t \sum_{n=-\infty}^{m} f(t_n)h(t_m - t_n)$. Implementing this discrete convolution in Eq. 2.15 for an observation time $t = t_m$ gives

$$\delta t \sum_{n=-\infty}^{m} i_{impr}(t_n)h_{self}(t_m - t_n) - \delta t \sum_{n=-\infty}^{m} i_{int}(t_n)h_{self}(t_m - t_n) = \delta t \sum_{n=-\infty}^{m} v(t_n)h_{weight}(t_m - t_n). \tag{2.18}$$

The internal current at a time t_m can be related to its value at a previous time-step, t_{m-1} , and the voltage $v(t_m)$ using the following update rule (demonstrated in Appendix C)

$$i_{int}(t_m) = e^{-\frac{\delta t}{\tau_c}} e^{-\frac{\delta t}{\tau_s}} \cdot i_{int}(t_{m-1}) + v(t_m)\cdot g(t_m) \tag{2.19a}$$

$$g(t_m) = A\cdot(\delta t)^2 \frac{q_e^2}{m_{e,GaAs}} \frac{W_z\cdot\Delta}{W_y} \sum_{n=-\infty}^{m} e^{-4ln2\frac{t_n^2}{\tau_p^2}} e^{-\frac{t_m-t_n}{\tau_c}}. \tag{2.19b}$$

The factor $g(t_m)$ relates current and voltage over time. Therefore it has the unit of conductance. In Eq. 2.18, the last terms of the summations ($n = m$) involving $i_{int}(t_n)$ and $v(t_n)$ ($\delta t\cdot i_{int}(t_m)h_{self}(0)$ and $\delta t\cdot v(t_m)h_{weight}(0)$, respectively) are separated and $i_{int}(t_m)$ is replaced with the expression from Eq. 2.19 to obtain

$$\begin{aligned}&\delta t \sum_{n=-\infty}^{m} i_{impr}(t_n)h_{self}(t_m - t_n) - \delta t \sum_{n=-\infty}^{m-1} i_{int}(t_n)h_{self}(t_m - t_n)\\ &-\delta t\cdot e^{-\frac{\delta t}{\tau_c}} e^{-\frac{\delta t}{\tau_s}} \cdot i_{int}(t_{m-1})h_{self}(0) - \delta t\cdot v(t_m)\cdot g(t_m)h_{self}(0) = \delta t \sum_{n=-\infty}^{m-1} v(t_n)h_{weight}(t_m - t_n) + \delta t\cdot v(t_m)h_{weight}(0).\end{aligned} \tag{2.20}$$

Dividing out δt and rearranging terms in Eq. 2.20 finally brings us to

$$v(t_m) = \frac{1}{h_{weight}(0) + g(t_m)h_{self}(0)} \Bigg\{ \sum_{n=-\infty}^{m} i_{impr}(t_n)h_{self}(t_m - t_n) - \sum_{n=-\infty}^{m-1} i_{int}(t_n)h_{self}(t_m - t_n) \\ - e^{-\frac{\delta t}{\tau_c}} e^{-\frac{\delta t}{\tau_s}} \cdot i_{int}(t_{m-1})h_{self}(0) - \sum_{n=-\infty}^{m-1} v(t_n)h_{weight}(t_m - t_n) \Bigg\}. \tag{2.21}$$

In Eq. 2.21, the voltage at a time t_m is related to voltages and internal currents from previous time-steps. It's also related to $i_{impr}(t)$, $h_{self}(t)$, $h_{weight}(t)$ and $g(t)$ which are considered to be known beforehand.

At a time t_{start}, before the laser arrives (e.g. $t_{start} = -0.3ps$), the internal current and the time-varying voltage can be put equal to zero since the gap hasn't been activated yet. Thus, one can calculate $v(t_{start})$ by putting all terms involving i_{int} and v equal to zero and keeping all the other terms in Eq. 2.21. Then, $v(t_{start})$ can be plugged into Eq. 2.19 to compute $i_{int}(t_{start})$. Subsequently, $v(t_{start})$ and $i_{int}(t_{start})$ can be used in Eq. 2.21 and 2.19 to find $v(t_{start+1})$ and $i_{int}(t_{start+1})$, which can be used to find $v(t_{start+2})$ and $i_{int}(t_{start+2})$... etc. Thus, via this marching-on-in-time procedure where one goes back and forth between Eq. 2.19 and 2.21 one can determine $v(t)$ and $i_{int}(t)$. Then the current through the antenna load in Fig. 2.2, $i(t)$, can also be found via Eq. 2.2.

2.1.3 Voltage Outside of the Source Region

Now that one has solved for the source quantities in Section 2.1.2, the voltage at locations outside of the source region, $v(x,t)$, can be determined.

The voltage shall be evaluated at discrete points along the slot: $x_k = k \cdot \delta x$, $k \in \mathbb{I}$. Similar to what was done in Eq. 2.9, the voltage at a location x_k is defined as its spatial average over the discretization length δx. Together with Eq. 2.5 this gives

$$V(x_k,\omega) \cong \left\{ \frac{1}{\delta x} \int_{x_k-\delta x/2}^{x_k+\delta x/2} V(x,\omega)dx \right\} = \frac{1}{2\pi} \int_{-\infty}^{\infty} \frac{I_e(k_x,\omega)}{D(k_x,\omega)} sinc\Big(\frac{k_x \delta x}{2}\Big) e^{-jk_x \cdot x_k} dk_x. \tag{2.22}$$

Combining the above expression with Eq. 2.7 one arrives to

$$V(x_k,\omega) = I(\omega) \cdot \frac{1}{2\pi} \int_{-\infty}^{\infty} \frac{sinc\Big(\frac{k_x\Delta}{2}\Big) sinc\Big(\frac{k_x\delta x}{2}\Big)}{D(k_x,\omega)} e^{-jk_x \cdot x_k} dk_x \equiv I(\omega)\tilde{Z}(x_k,\omega) \tag{2.23a}$$

$$\tilde{Z}(x_k,\omega) = \frac{1}{2\pi} \int_{-\infty}^{\infty} \frac{sinc\Big(\frac{k_x\Delta}{2}\Big) sinc\Big(\frac{k_x\delta x}{2}\Big)}{D(k_x,\omega)} e^{-jk_x \cdot x_k} dk_x. \tag{2.23b}$$

In Eq. 2.23, $\tilde{Z}(x_k,\omega)$ represents a mutual impedance that relates the average voltage at a position x_k, to the current generated by the source, $I(\omega)$, which is located in the region: $|x| \le \frac{\Delta}{2}$. In fact, $\tilde{Z}(x_k,\omega)$ only depends on the distance from the source, $|x_k|$, instead of the observed position itself, x_k (demonstrated in Appendix D). Similar to what was done in Eq. 2.13 and 2.14, both sides of Eq. 2.23 are now divided by the weighting function $\tilde{Z}^2(0,\omega) = (\tilde{Z}(0,\omega))^2 = \tilde{Z}^2(x_k = 0,\omega)$

$$\frac{V(x_k,\omega)}{\tilde{Z}^2(0,\omega)} = I(\omega) \cdot \frac{\tilde{Z}(x_k,\omega)}{\tilde{Z}^2(0,\omega)}. \tag{2.24}$$

Notice that Eq. 2.24 is very similar to Eq. 2.14 ($I(\omega) = I_{impr}(\omega) - I_{int}(\omega)$) but now it's being solved for a position x_k. Taking an inverse Fourier transform on both sides of Eq. 2.24 to go to the time-domain results in

$$v(x_k,t) * \tilde{h}_{weight}(t) = i(t) * \tilde{h}_{mutual}(x_k,t) \tag{2.25a}$$

$$\tilde{h}_{weight}(t) \overset{\mathscr{F}}{\Longleftrightarrow} \frac{1}{\tilde{Z}^2(0,\omega)}, \quad \tilde{h}_{mutual}(x_k,t) \overset{\mathscr{F}}{\Longleftrightarrow} \frac{\tilde{Z}(x_k,\omega)}{\tilde{Z}^2(0,\omega)}, \tag{2.25b}$$

with $i(t)$ being the source current that was obtained in Section 2.1.2. Even though it is not straightforward to give an interpretation to $\tilde{h}_{mutual}$ itself, $\mathscr{F}^{-1}\{\tilde{Z}(x_k,\omega)\}$ does have a physical interpretation. It represents an

impulse response that relates the average voltage observed at a position x_k, $v(x_k,t)$, to the source current $i(t)$ (which is centered around $x=0$).

In Fig. 2.4 the time-domain signals $h_{weight}(t)$ ($\tilde{h}_{weight}(t)$ is very similar to $h_{weight}(t)$ so not shown), $h_{self}(t)$ and $\tilde{h}_{mutual}(x_k,t)$ for different positions x_k are shown. Notice how all these signals show a similar behaviour: first the signal is quite stagnant, afterwards a peak occurs followed by a decay towards zero. Actually, the decay after the peak goes even below zero. This is the start of a long, slow oscillation around zero (not shown in the graphs for visibility of the peaks). Furthermore, all signals show some behaviour before $t=0$. The segments before zero shown in Fig. 2.4 are also part of long, slow oscillations around zero. Such inaccuracies happen because these functions have been obtained via an inverse Fourier transform implemented numerically. Numerical implementations of the inverse Fourier transforms often lead to signals which oscillate around the correct value, even for negative times. These values at negative times are not taken into account since the formulations given in Section 2.1.2 and 2.1.3 only utilize positive times for the signals presented in Fig. 2.4. One should observe that $\tilde{h}_{mutual}(x_k,t)$, gives a shifted and attenuated signal for increasing x_k due to the elevated propagation times and attenuation associated with larger distances.

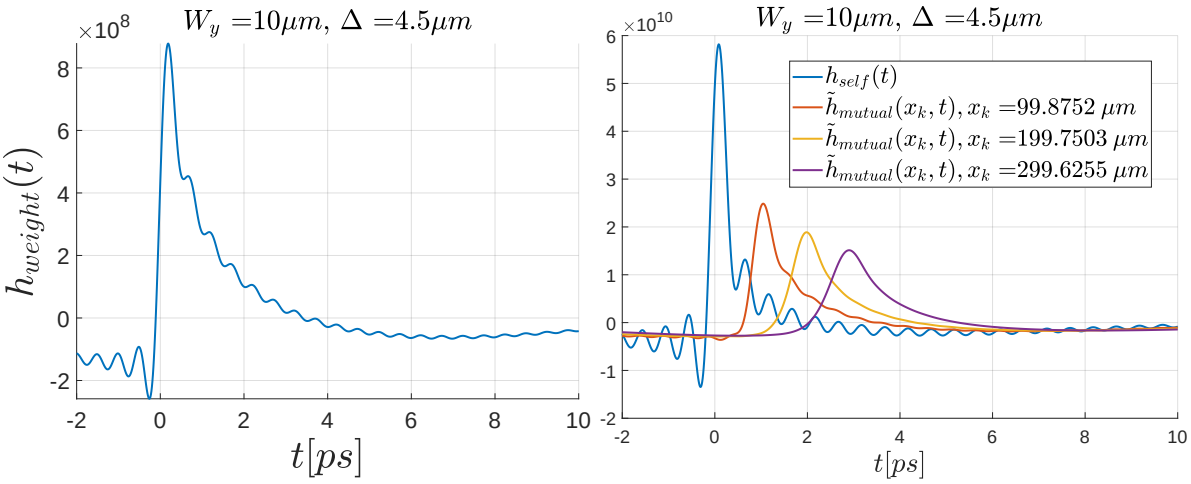

Figure 2.4: Time-domain signals (a) h_{weight}, (b) $h_{self}(t)$ and $\tilde{h}_{mutual}(x_k,t)$ for different positions x_k. For an infinite slot with $W_y = 10\,\mu m$ and $\Delta = 4.5\,\mu m$.

Evaluating Eq. 2.25 at an observation time $t = t_m$ and applying a time-discretization to the convolution of the signals brings us to

$$\delta t \sum_{n=-\infty}^{m} v(x_k,t_n)\tilde{h}_{weight}(t_m-t_n) = \delta t \sum_{n=-\infty}^{m} i(t_n)\tilde{h}_{mutual}(x_k,t_m-t_n). \tag{2.26}$$

Finally, after dividing out δt, rearranging terms and separating the last term of the summation involving $v(x_k,t_n)$ in Eq. 2.26 one has found an update rule for the voltage along the slot.

$$v(x_k,t_m) = \frac{\sum_{n=-\infty}^{m} i(t_n)\tilde{h}_{mutual}(x_k,t_m-t_n) - \sum_{n=-\infty}^{m-1} v(x_k,t_n)\tilde{h}_{weight}(t_m-t_n)}{\tilde{h}_{weight}(0)}. \tag{2.27}$$

Again, before the laser arrives, $v(t)$ is considered to be zero. Thus, if a time instance $t_m = t_{start}$ is early enough such that the laser hasn't arrived yet, $v(x_k,t_{start})$ can be found via Eq. 2.27 by putting the summation involving $v(x_k,t_n)$ on the right-hand side equal to zero. Subsequently, $v(x_k,t_{start})$ ought to be plugged into Eq. 2.27 to obtain $v(x_k,t_{start+1})$, which can be used to find $v(x_k,t_{start+2})$... and so on. By implementing this marching-on-in-time procedure for every position x_k the voltage along the entire slot as a function of time is obtained.

2.2 Transmission Line Equivalent Circuit

The integrand of the integral representing the input impedance of the slot given by Eq. 2.10 consists of two polar singularities [10] at $k_x = \pm k_{xp}$. The position of the poles are a function of frequency, so $k_{xp} \equiv k_{xp}(\omega)$. The influence and meaning of these polar singularities are highlighted in this section.

First, a first-order Taylor expansion of $D(k_x,\omega)$ in Eq. 2.6 around the two poles is performed

$$D(k_x) \approx D(k_{xp}) + (k_x - k_{xp})D'(k_{xp}) = (k_x - k_{xp})D'(k_{xp}), \qquad expansion\ around\ k_{xp} \tag{2.28a}$$
$$D(k_x) \approx D(-k_{xp}) + (k_x - -k_{xp})D'(-k_{xp}) = -(k_x + k_{xp})D'(k_{xp}), \quad expansion\ around\ -k_{xp}. \tag{2.28b}$$

In Eq. 2.28 the properties $D(\pm k_{xp}) = 0$, $D(k_x) = D(-k_x)$ and $D'(-k_{xp}) = -D'(k_{xp})$ [10] have been used. From the integrand in Eq. 2.10, one can add and subtract the same term: $sinc^2\Big(\frac{k_x\Delta}{2}\Big)\Big(\frac{1}{(k_x-k_{xp})D'(k_{xp})} + \frac{-1}{(k_x+k_{xp})D'(k_{xp})}\Big)$. This gives the following

$$\begin{aligned} Z(\omega) &= \frac{1}{2\pi}\int_{-\infty}^{\infty} \frac{sinc^2\Big(\frac{k_x\Delta}{2}\Big)}{D(k_x,\omega)}dk_x \\ &= \frac{1}{2\pi}\int_{-\infty}^{\infty} \frac{sinc^2\Big(\frac{k_x\Delta}{2}\Big)}{D(k_x,\omega)} - sinc^2\Big(\frac{k_x\Delta}{2}\Big)\Big(\frac{1}{(k_x-k_{xp})D'(k_{xp})} + \frac{-1}{(k_x+k_{xp})D'(k_{xp})}\Big)dk_x \\ &+ \frac{1}{2\pi}\int_{-\infty}^{\infty} sinc^2\Big(\frac{k_x\Delta}{2}\Big)\Big(\frac{1}{(k_x-k_{xp})D'(k_{xp})} + \frac{-1}{(k_x+k_{xp})D'(k_{xp})}\Big)dk_x. \end{aligned} \tag{2.29}$$

Notice that the denominators of the additional fractions in Eq. 2.29 are equal to the expansions given by Eq. 2.28. Therefore, in the limit $k_x \to \pm k_{xp}$, one of these fractions will be equal to $\frac{sinc^2\left(\frac{k_x\Delta}{2}\right)}{D(k_x,\omega)}$. Thus, in the integral containing the term $\frac{sinc^2\left(\frac{k_x\Delta}{2}\right)}{D(k_x,\omega)}$, the polar contributions are cancelled out which allows for a faster convergence during numerical implementation. Moreover, the second integral containing only the fractions with the expansions can be evaluated analytically. To see that, first one should note that the factor containing the fractions with the expansions can be simplified as follows (involving a few algebraic steps not shown here): $\frac{1}{(k_x-k_{xp})D'(k_{xp})} + \frac{-1}{(k_x+k_{xp})D'(k_{xp})} = \frac{2k_{xp}}{(k_x^2-k_{xp}^2)D'(k_{xp})}$. Combining this with Eq. 2.29, one arrives to

$$Z(\omega) = \frac{1}{2\pi}\int_{-\infty}^{\infty}\Big(\frac{1}{D(k_x,\omega)} - \frac{2k_{xp}}{(k_x^2-k_{xp}^2)D'(k_{xp})}\Big)sinc^2\Big(\frac{k_x\Delta}{2}\Big)dk_x + \frac{1}{2\pi}\int_{-\infty}^{\infty}\frac{2k_{xp}}{(k_x^2-k_{xp}^2)D'(k_{xp})}sinc^2\Big(\frac{k_x\Delta}{2}\Big)dk_x. \tag{2.30}$$

The second integral which does not involve $D(k_x,\omega)$ has an analytical, closed-form solution [22]

$$\frac{1}{2\pi}\int_{-\infty}^{\infty}\frac{2k_{xp}}{(k_x^2-k_{xp}^2)D'(k_{xp})}sinc^2\Big(\frac{k_x\Delta}{2}\Big)dk_x = \frac{1}{\Delta}\frac{1}{D'(k_{xp})}\frac{2}{k_{xp}}\Big(sinc\Big(\frac{k_{xp}\Delta}{2}\Big)-1\Big) - j\frac{1}{D'(k_{xp})}sinc^2\Big(\frac{k_{xp}\Delta}{2}\Big). \tag{2.31}$$

The following, short-hand notation shall be adopted for the several terms involved

$$Z_{rem}^{dyn}(\omega) \equiv \frac{1}{2\pi}\int_{-\infty}^{\infty}\Big(\frac{1}{D(k_x,\omega)} - \frac{2k_{xp}}{(k_x^2-k_{xp}^2)D'(k_{xp})}\Big)sinc^2\Big(\frac{k_x\Delta}{2}\Big)dk_x$$
$$Z_{pole}^{int}(\omega) \equiv \frac{1}{\Delta}\frac{1}{D'(k_{xp})}\frac{2}{k_{xp}}\Big(sinc\Big(\frac{k_{xp}\Delta}{2}\Big)-1\Big), \quad Z_{pole}^{ext}(\omega) \equiv -j\frac{1}{D'(k_{xp})}sinc^2\Big(\frac{k_{xp}\Delta}{2}\Big), \quad Z_{rem}(\omega) \equiv Z_{rem}^{dyn}(\omega) + Z_{pole}^{int}(\omega). \tag{2.32}$$

Combining Eq. 2.30, 2.31 and 2.32 brings us now to

$$Z(\omega) = Z_{rem}^{dyn}(\omega) + Z_{pole}^{int}(\omega) + Z_{pole}^{ext}(\omega) = Z_{rem}(\omega) + Z_{pole}^{ext}(\omega). \tag{2.33}$$

The equivalent circuit in Fig. 2.2 can also be depicted in a slightly different manner as shown in Fig. 2.5 below. In this representation $z_g(t) = \mathscr{F}^{-1}\{Z_g(\omega)\} = \mathscr{F}^{-1}\left\{\frac{V(\omega)}{I_{int}(\omega)}\right\}$ and $z(t) = \mathscr{F}^{-1}\{Z(\omega)\} = \mathscr{F}^{-1}\left\{\frac{V(\omega)}{I(\omega)}\right\}$. It is important to point out that the quantities $z_g(t)$ and $Z_g(\omega)$ can only be obtained after the circuit has been solved in the time-domain. After one has solved the circuit for $v(t)$ and $i_{int}(t)$, their Fourier transforms can be computed to subsequently find the generator impedance.

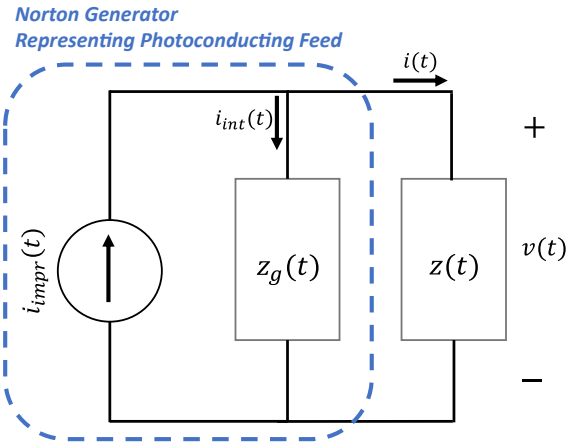

Figure 2.5: Norton equivalent circuit describing the interaction between a photoconducting feed and the antenna in which this feed is placed. The inverse Fourier transforms of the generator impedance and the input impedance of the antenna are denoted by $z_g(t)$ and $z(t)$, respectively.

Utilizing the decomposition stated in Eq. 2.33 gives the circuit depicted in Fig. 2.6

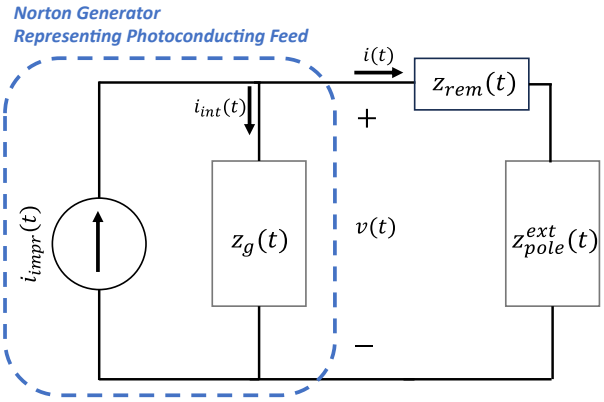

Figure 2.6: Norton equivalent circuit describing the interaction between a photoconducting feed and the antenna in which this feed is placed. The input impedance of the antenna is decomposed in a remainder term and a pole contribution, $z_{rem}(t)$ and $z^{ext}_{pole}(t)$, respectively.

with $z_{rem}(t) = \mathscr{F}^{-1}\{Z_{rem}(\omega)\}$ and $z^{ext}_{pole}(t) = \mathscr{F}^{-1}\{Z^{ext}_{pole}(\omega)\}$. The term $Z^{ext}_{pole}(\omega)$ can be actually be regarded as the input impedance seen from one side of a transformer that couples the feed to two infinite, parallel transmission lines [21]. This is illustrated in Fig. 2.7. The transmission lines have a characteristic impedance of $Z_{0,s} = -\frac{2j}{D'_s(k_{xp})}$ and the transformer has a turns ratio $n_\delta = sinc(\frac{k_{xp}\Delta}{2})$ [21].

Going back to Eq. 2.24, it implies $V(x_k,\omega) = I(\omega)\tilde{Z}(x_k,\omega)$. For sufficiently large distances from the source (e.g. $|x_k| = 100\mu m$), the mutual impedance can be approximated with its residue

$$\tilde{Z}(x_k,\omega) = \frac{1}{2\pi}\int_{-\infty}^{\infty} \frac{sinc\left(\frac{k_x\Delta}{2}\right)sinc\left(\frac{k_x\delta x}{2}\right)}{D(k_x,\omega)} e^{-jk_x\cdot x_k}\,dk_x \cong -j\frac{sinc\left(\frac{k_{xp}\Delta}{2}\right)sinc\left(\frac{k_{xp}\delta x}{2}\right)}{D'(k_{xp},\omega)} e^{-jk_{xp}\cdot|x_k|}, \quad |x_k|\ large. \tag{2.34}$$

The absolute value of x_k is used to take into account a switch of pole locations when the sign of x_k changes. For the voltage this gives

$$V(x_k,\omega) \cong I(\omega)\cdot -j\frac{sinc\left(\frac{k_{xp}\Delta}{2}\right)sinc\left(\frac{k_{xp}\delta x}{2}\right)}{D'(k_{xp},\omega)}e^{-jk_{xp}\cdot|x_k|}, \quad |x_k|\ large. \tag{2.35}$$

The expression in Eq. 2.35 contains a complex exponential where the exponent has a propagation constant k_{xp} multiplied with a distance, $|x_k|$. Also, the exponential is multiplied with complex amplitude $I(\omega)\cdot -j\frac{sinc\left(\frac{k_{xp}\Delta}{2}\right)sinc\left(\frac{k_{xp}\delta x}{2}\right)}{D'(k_{xp},\omega)}$. This indicates a voltage wave with the mentioned complex amplitude, propagating along a transmission line with propagation constant k_{xp}.

The residue of the mutual impedance, in combination with the equivalent circuit of Fig. 2.7 suggests a mental picture (when sufficiently far away from the source). In this mental picture the photoconducting feed can be seen as a current source that excites voltage waves. These waves propagate to the left and to the right of the source. These waves propagate via the transmission lines shown in Fig. 2.7. Since k_{xp} depends on the frequency, so does the characteristic impedance $Z_{0,s}$. This means that the different frequency components of the voltage waves see a different impedance of the transmission line. Moreover, k_{xp} has both a real and an imaginary part that differ over frequency. Thus, different frequency components of the voltage waves have a different propagation speed and they do not experience the same degree of attenuation as they move.

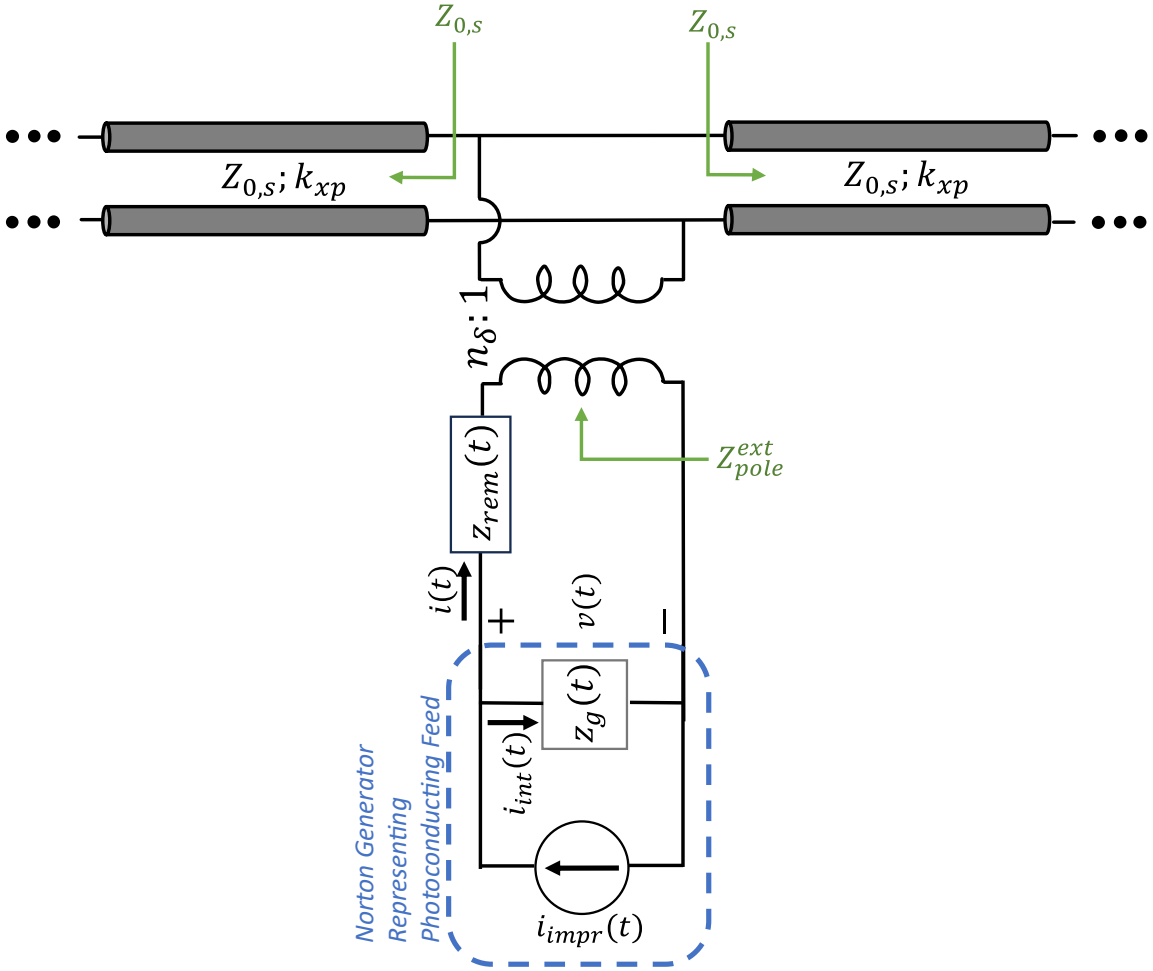

Figure 2.7: Transmission line equivalent circuit describing the interaction between a photoconducting feed and the antenna in which this feed is placed. The input impedance of the antenna is decomposed in a remainder term ($z_{rem}(t)$) and a pole contribution. The pole contribution is regarded as a transformer coupled to two infinite, parallel transmission lines. The transformer has a turns ratio n_δ. Furthermore, the transmission line has a characteristic impedance $Z_{0,s}$ and a propagation constant k_{xp}.

In Fig. 2.8 the real and imaginary part of the propagation constant k_{xp}, normalized to the free-space wavenumber k_0, are shown as a function of frequency. The values shown are for a slot with a width $W_y = 10\,\mu m$.

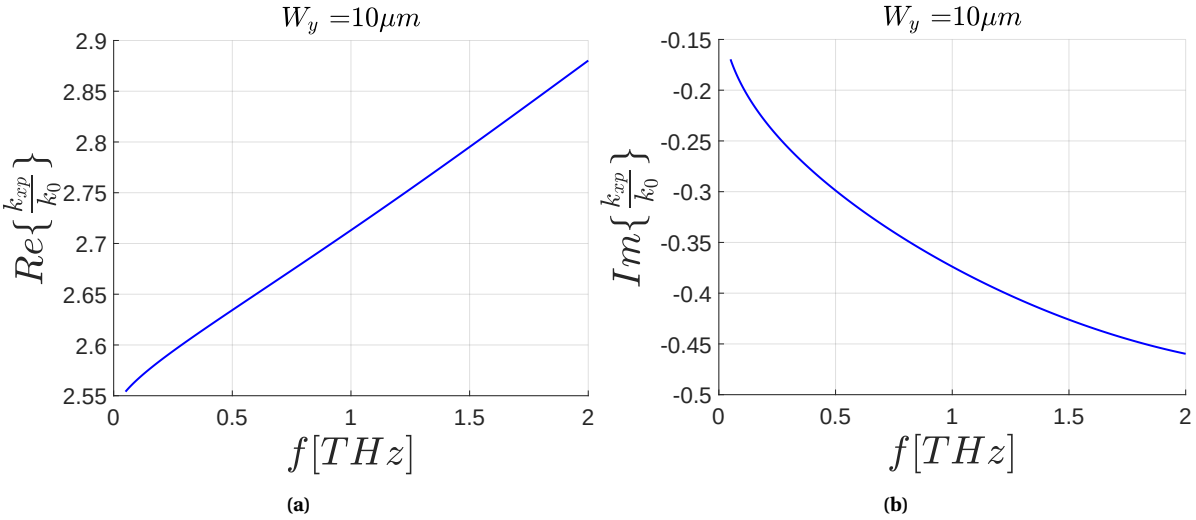

Figure 2.8: (a) Real and (b) imaginary part of the propagation constant k_{xp} versus frequency. In both graphs, $W_y = 10\mu m$ and the values are normalized to the free-space wavenumber k_0.

From Fig. 2.8a one can deduce that the higher frequencies propagate slower along the slot. Furthermore, Fig. 2.8b indicates that the higher frequencies attenuate more compared to the lower frequencies as they propagate.

2.3 Results of the Marching-On Procedure

2.3.1 Norton Generator Impedance

After solving for the time-domain quantities using the marching-on procedures in Sections 2.1.2 and 2.1.3, the generator impedance of the Norton equivalent circuit can be obtained using the Fourier transforms of the internal current and the voltage at the source since $Z_g(\omega) = \frac{V(\omega)}{I_{int}(\omega)}$. In Fig. 2.9 below $Z_g(\omega)$ is shown for several combinations of the average optical power absorbed in the gap, $\tilde{P}_{opt}$, and the width of the slot W_y.

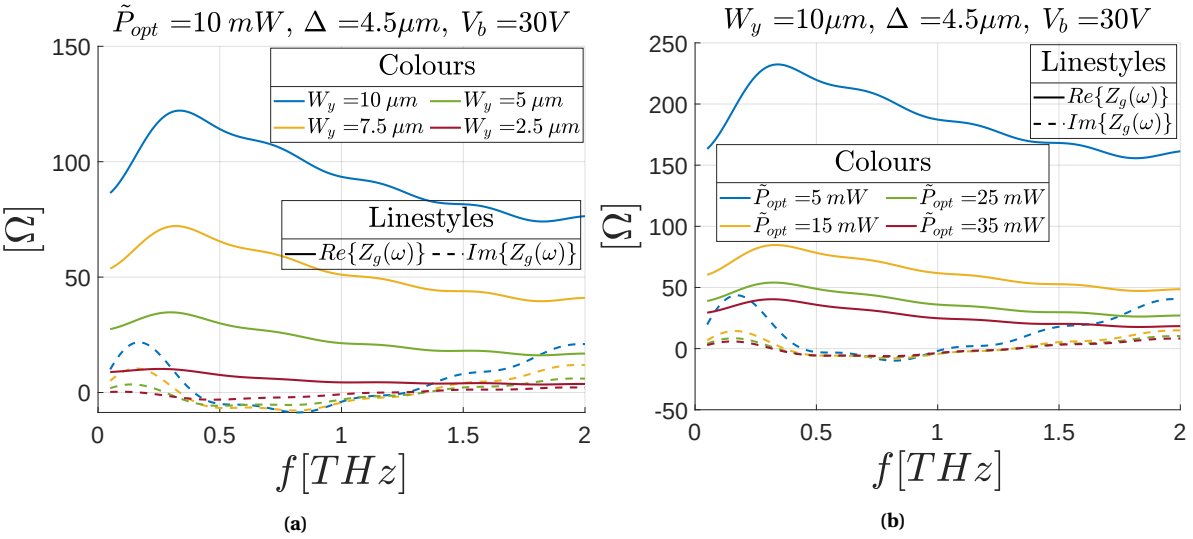

Figure 2.9: (a) Generator impedance of the Norton equivalent circuit representing the photoconducting gap for several widths W_y and (b) different amounts of optical power $\tilde{P}_{opt}$.

In Fig. 2.9a, where the optical power is set to $\tilde{P}_{opt} = 10\,mW$, one can observe that an increase of the slot width leads to an increase in the real and imaginary part of $Z_g(\omega)$.
Furthermore, in Fig. 2.9b the width is equal to $W_y = 10\,\mu m$ and the optical power varies. In this case an increase in optical power results in a decreasing real and imaginary part of the generator impedance. In both Fig. 2.9a and 2.9b, the imaginary part of $Z_g(\omega)$ stays mostly around zero Ohm with some relatively small peaks around 0.2 THz and 2 THz.

2.3.2 Voltage and Current in the Photo Conducting Gap

The impressed current, internal current and the current through the antenna load are shown in Fig. 2.10 for two cases. The differences lie in the optical power and the width of the slot. In Fig. 2.10a $W_y = 2.5\,\mu m$ and $\tilde{P}_{opt} = 10\,mW$ while in Fig. 2.10b $W_y = 10\,\mu m$ and $\tilde{P}_{opt} = 35\,mW$.

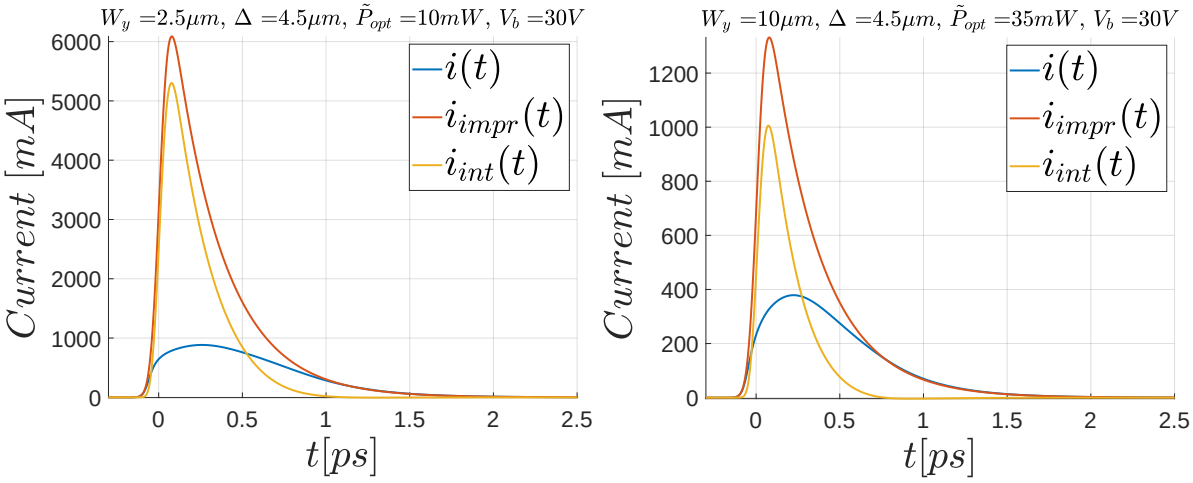

Figure 2.10: Impressed current, internal current and current through the antenna load for (a) $W_y = 2.5\,\mu m$ and $\tilde{P}_{opt} = 10\,mW$ and (b) for $W_y = 10\,\mu m$ and $\tilde{P}_{opt} = 35\,mW$. In both figures $\Delta = 4.5\,\mu m$ and $V_b = 30\,V$.

In both figures most of the impressed current goes towards the internal current. This is the case because the generator impedance is significantly lower compared to the input impedance of the antenna for most of the bandwidth. To see this, one ought to compare Fig. 2.3 and 2.9 for the cases depicted in Fig. 2.10. On the contrary, in Fig. 2.11a most of the impressed current goes towards the antenna load current.

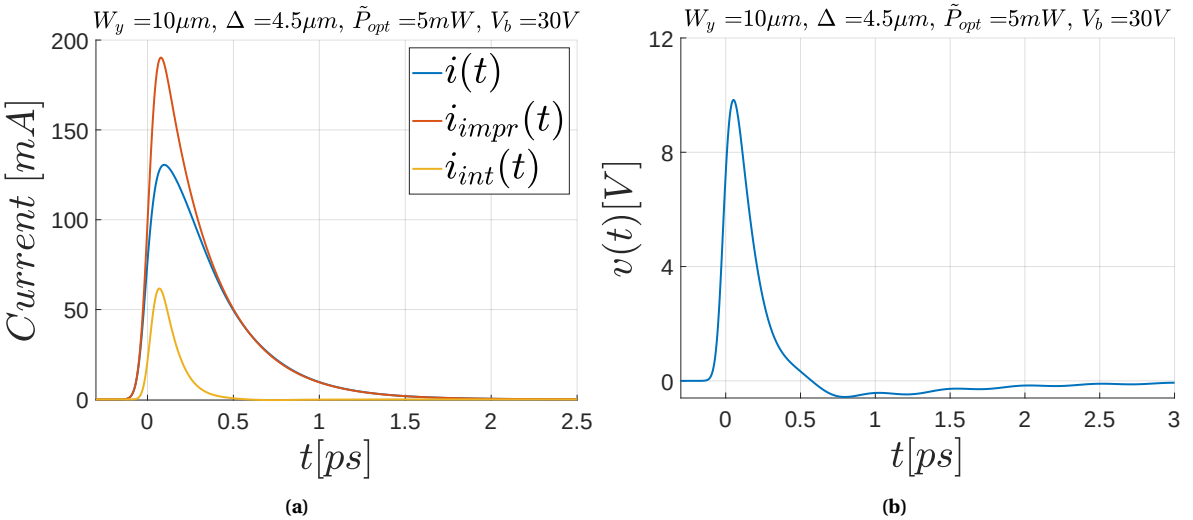

Figure 2.11: (a) Impressed current, internal current and current through the antenna load for $W_y = 10\,\mu m$, $\Delta = 4.5\,\mu m$, $\tilde{P}_{opt} = 5\,mW$ and $V_b = 30\,V$. (b) Time-varying voltage across the photoconducting gap for the same situation.

Comparing Fig. 2.3b and 2.9b for $\Delta = 4.5\,\mu m$ and $\tilde{P}_{opt} = 5\,mW$ one should observe that the generator impedance is larger than the antenna input impedance across the band. This explains why in the current division of the Norton equivalent circuit, most of the current goes towards the antenna load. One ought to keep in mind that maximum current transfer does not imply maximum power transfer towards the load. Maximum power transfers requires the generator impedance and the load to be conjugate matched over the considered bandwidth. Furthermore, in Fig. 2.11b the time-varying voltage $v(t)$ corresponding to the currents in Fig. 2.11a is shown.

In Fig. 2.12 the Fourier transforms of the currents in Fig. 2.10a and 2.11a are depicted. In both cases, the spectra have their maximum at the lower frequencies. However, varying the width and the optical power does seem to significantly influence the rate of decay in the spectra. For example, the decay of the load current until 1 THz is much steeper in Fig. 2.12b compared to Fig. 2.12a. This can be attributed to the corresponding impedances in Fig. 2.3 and 2.9 showing significantly different behaviour.

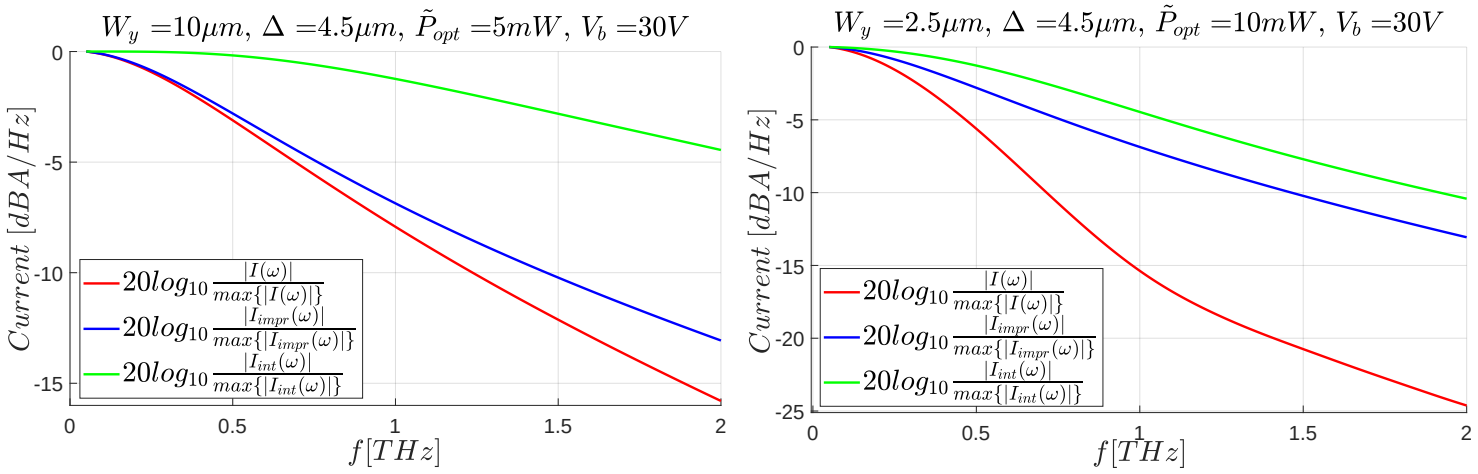

(a) **(b)**

Figure 2.12: Fourier transform of the impressed current, internal current and current through the antenna load for (a) $W_y = 10\,\mu m$, $\tilde{P}_{opt} = 5\,mW$ and (b) $W_y = 2.5\,\mu m$, $\tilde{P}_{opt} = 10\,mW$. In both cases $\Delta = 4.5\,\mu m$ and $V_b = 30\,V$.

After having obtained the voltages and currents in the time-domain, one can insert their Fourier transforms in Eq. 2.12a to check whether this original equation (which doesn't include a weighting function) is satisfied. The results of this procedure for the quantities in Fig. 2.11 are illustrated in Fig. 2.13 below.

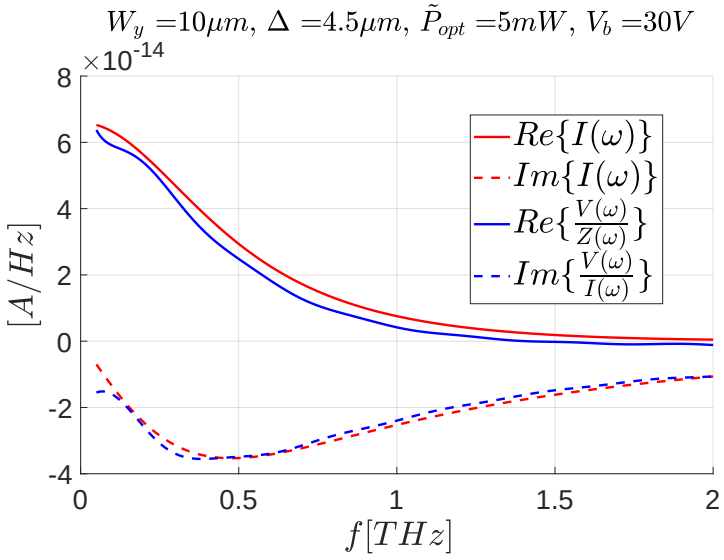

Figure 2.13: The Fourier transforms of $i(t)$ and $v(t)$ ($I(\omega)$ and $V(\omega)$, respectively) from Fig. 2.11 have been inserted in Eq. 2.12a to examine whether this original equation is satisfied.

Essentially, the real part and the imaginary part of the left-hand side and right-hand side of Eq. 2.12a are being compared. There's quite a decent match between the two sides of Eq. 2.12a, especially for the imaginary part. Any discrepancies are most likely related to numerical inaccuracies such as a finite simulation time in combination with a non-zero spacing between the frequency points considered.

2.3.3 Voltage Propagation Along the Slot

The propagation of the voltage waves along the slot is illustrated in Fig. 2.14 (same parameters as in Fig. 2.11). It shows the voltage as a function of position for different time-instances. One can see that initially, the wave emerges at the center ($x = 0\,\mu m$) and afterwards it splits into two equal wavefronts which are moving to the left and right, away from the feed. Furthermore, Fig. 2.14 shows how the waves attenuate as they move over time. When significantly far away from the source, the residue contribution of the mutual impedance accurately represents the coupling to the feed as indicated in Eq. 2.35. In this case, the attenuation is mainly due to the imaginary part of the propagation constant k_{xp} which is depicted in Fig. 2.8b.

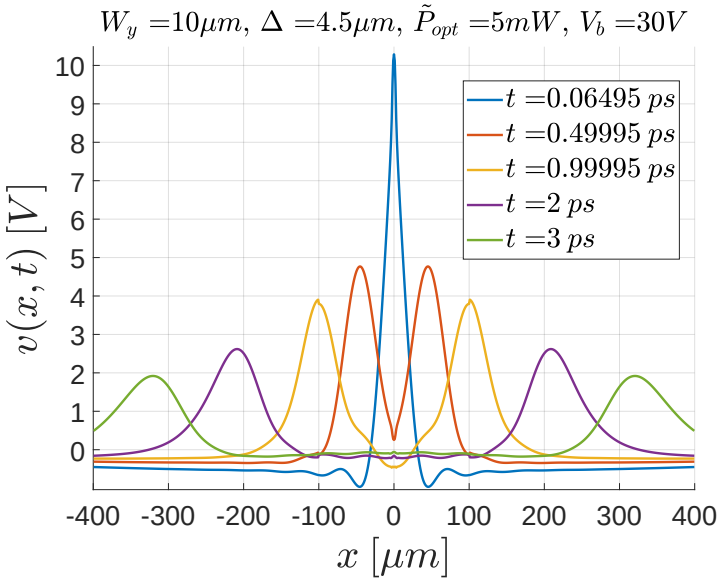

Figure 2.14: Voltage along the slot as a function of position evaluated at different time-instances.

Another perspective is given in Fig. 2.15 where the voltage versus time is depicted for different positions along the slot.

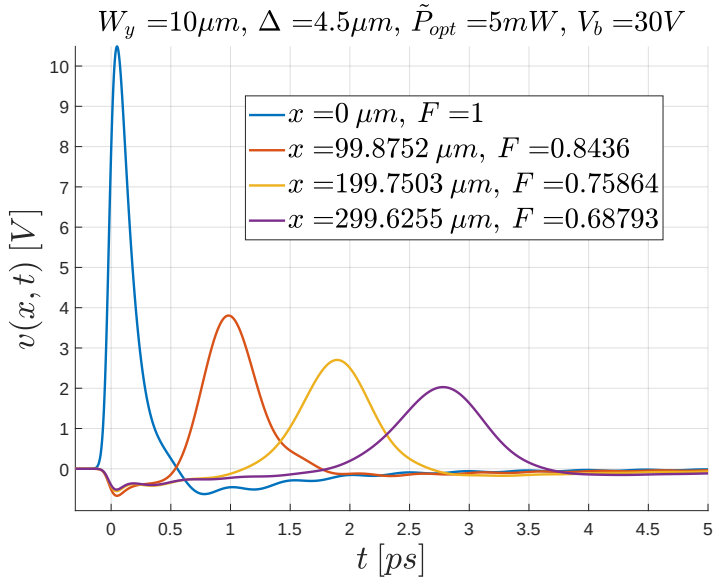

Figure 2.15: Voltage as a function of time evaluated at different positions along the slot.

Also in this graph the attenuation is visible. Furthermore, since the different frequency components of the voltage wave do not have the same velocity and attenuation according to Fig. 2.8, the shape of the wave changes as it propagates along the slot. This distortion can be quantified using the fidelity factor F (also indicated in Fig. 2.15). The following definition for the fidelity factor related to a signal $s_t(t)$ and a reference $s_r(t)$ is used [23]:

$$F = \max_{\tau} \frac{\int_{-\infty}^{\infty} s_t(t) s_r(t-\tau)\, dt}{\sqrt{\int_{-\infty}^{\infty} |s_t(t)|^2 dt \cdot \int_{-\infty}^{\infty} |s_r(t)|^2 dt}}. \tag{2.36}$$

The fidelity factor indicates how similar the two signals are in terms of shape (so scaling or a time-shift doesn't affect the outcome). In Fig. 2.15, the reference is the voltage at $x = 0\,\mu m$. In the figure one can see that the fidelity decreases for larger distances. This happens because the shape of the wave changes more and more as it propagates due to the dispersivity in terms of propagation velocity and attenuation mentioned earlier.

Chapter 3

Slot Antenna Fed by Two Pulsed Photo Conducting Sources

3.1 Formulation

3.1.1 Defining the Problem

Consider an infinite slot with a width W_y between two semi-infinite, non-magnetic, homogeneous media. "Medium 1" ($z < -W_z$) and "medium 2" ($z > 0$) have a relative permittivity of $\varepsilon_{r,1}$ and $\varepsilon_{r,2}$, respectively. Two photoconducting gaps are placed in the slot at locations $x_{f1} = -\frac{d_x}{2}$ and $x_{f2} = \frac{d_x}{2}$. Both gaps have a length equal to Δ and depth W_z. The structure is depicted in Figure 3.1. The gaps are activated by optical, pulsed lasers that free charged carriers. These carriers constitute a current along $\hat{y}$ because of the acceleration induced by the bias voltages. At the center of the slot, perpendicular to its axis, there's a small separation between the metals of length d_{gap}. This gap enables one to control the structure with separate bias voltages for the two feeds, $V_{b,1}$ and $V_{b,2}$. The capacitance related to this separation is considered to be high enough such that at all frequencies considered, the associated impedance is essentially zero. Therefore, the gap shall not be taken into account for the electromagnetic formulation. It's purpose is only to allow one to possibly use different biases for the feeds. In this chapter, the objective is to determine the induced voltages in the photoconducting gap central positions, $v(x_{f1}, t)$ and $v(x_{f2}, t)$, as well as the voltage at all other positions along the slot, represented by $v(x, t)$.

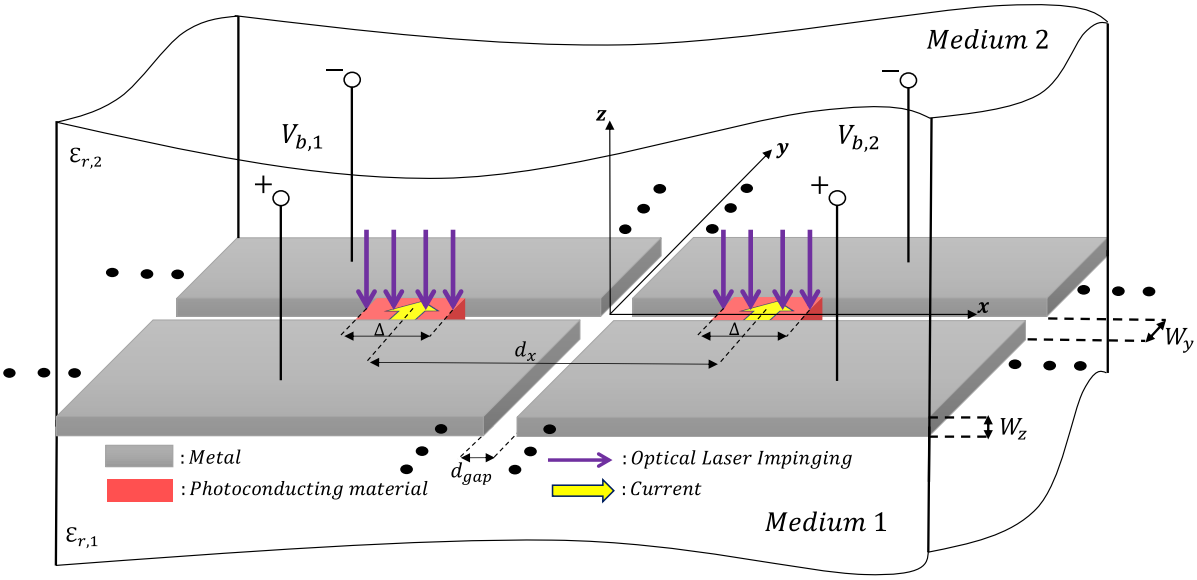

Figure 3.1: Infinite slot with a width W_y between two semi-infinite media with photoconducting material placed at $x_{f1} = -\frac{d_x}{2}$ and $x_{f2} = \frac{d_x}{2}$. The photoconducting material has a length equal to Δ and depth W_z. The photoconducting gaps are activated by optical, pulsed lasers. Adapted from [10].

In Fig. 3.2 the $xy-$plane of the infinite slot (without gap) from Fig. 3.1 is shown. Moreover, Fig. 3.2 also indicates that each photoconducting feed has its own Norton equivalent circuit assigned to it. This implies that the feeds do not necessarily have the same impressed current, internal current and generator impedance. A slightly adjusted version of Eq. 2.17 shall be used to evaluate the impressed currents $i_{impr,1}(t)$ and $i_{impr,2}(t)$:

$$i_{impr,j}(t_m) \cong A \cdot \delta t \frac{q_e^2}{m_{e,GaAs}} \frac{W_z \cdot \Delta}{W_y} V_{b,j} \cdot \tau_s \sum_{n=-\infty}^{m} e^{-4ln2\frac{(t_n - t_{delay,j})^2}{\tau_p^2}} \left[1 - e^{-\frac{t_m - t_n}{\tau_s}}\right] e^{-\frac{t_m - t_n}{\tau_c}}, \quad j \in \{1,2\}. \tag{3.1}$$

The expression in Eq. 3.1 gives one the flexibility to adjust the bias voltage and the moment of optical excitation for each feed separately. This flexibility is embedded in Eq. 3.1 via the parameters $V_{b,j}$ and $t_{delay,j}$ respectively.

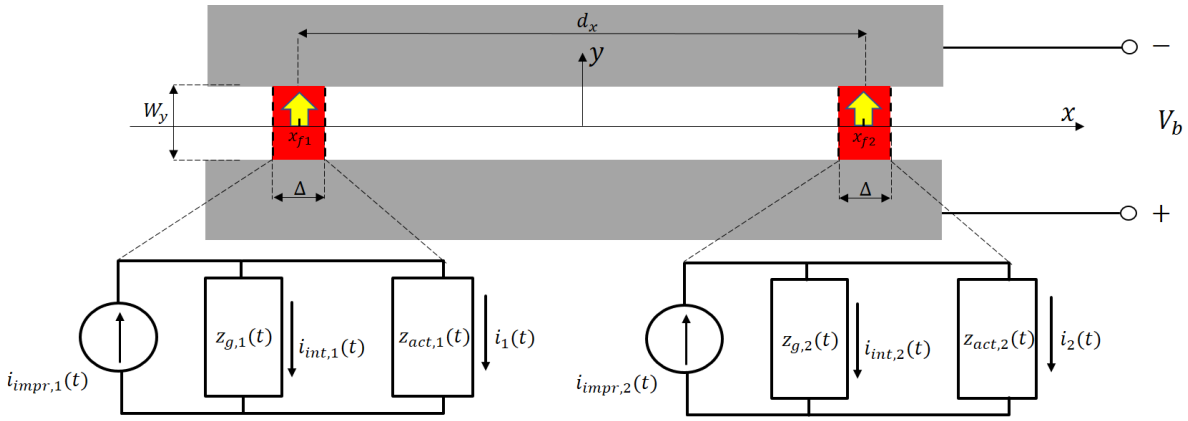

Figure 3.2: $xy-$plane of the infinite slot depicted in Fig. 3.1. Each photoconducting feed has its own Norton equivalent circuit assigned to it.

One ought to keep in mind that the laser is spread out over time according to the term $e^{-4ln2\frac{(t_n - t_{delay,j})^2}{\tau_p^2}}$ with $t_{delay,j}$ the moment at which the peak of the laser pulse arrives. How one would be able to adjust the optical excitation delay for each feed separately in practice is not discussed in this chapter. Additionally, each feed now has its own "active" antenna load impedance. The load impedances are active because they will depend on the excitations of both feeds. These load impedances can differ per feed.
Furthermore, it is important to note that Eq. 2.5 still holds. However in this chapter, the Fourier transform related to the current, $I_e(k_x,\omega)$, shall be a bit different as will be detailed in Section 3.1.2.

3.1.2 Voltage and Current Provided by the Sources

Utilizing the same reasoning that was applied in Section 2.1.1, the voltages at the feeds are defined as the spatial average of the voltage distributions over the gap lengths. Together with Eq. 2.5 this gives

$$V(x_s,\omega) \equiv \left\{\frac{1}{\Delta}\int_{x_s-\Delta/2}^{x_s+\Delta/2} V(x,\omega)dx\right\} = \frac{1}{2\pi}\int_{-\infty}^{\infty} \frac{I_e(k_x,\omega)}{D(k_x,\omega)} sinc\left(\frac{k_x\Delta}{2}\right) e^{-jk_x \cdot x_s} dk_x, \quad x_s \in \{x_{f1}, x_{f2}\}. \tag{3.2}$$

Also here, spatial variations of the laser beam over a length Δ are considered small enough such that the currents provided by the feeds are constant over the gap lengths. Thus, the Fourier transform of the currents divided by the gap length ($I_e(k_x,\omega)$ in Eq. 2.5), is equal to

$$\begin{aligned} I_e(k_x,\omega) &= \frac{1}{\Delta}\mathscr{F}\left\{\mathscr{F}_{spatial}\left\{i_1(t)\cdot rect\left(\frac{x-x_{f1}}{\Delta}\right) + i_2(t)\cdot rect\left(\frac{x-x_{f2}}{\Delta}\right)\right\}\right\} \\ &= I_1(\omega) sinc\left(\frac{k_x\Delta}{2}\right) e^{jk_x\cdot x_{f1}} + I_2(\omega) sinc\left(\frac{k_x\Delta}{2}\right) e^{jk_x\cdot x_{f2}}, \end{aligned} \tag{3.3}$$

where $I_1(\omega) \overset{\mathscr{F}}{\Longleftrightarrow} i_1(t)$ and $I_2(\omega) \overset{\mathscr{F}}{\Longleftrightarrow} i_2(t)$. The currents $i_1(t)$ and $i_2(t)$ represent the antenna load currents which are indicated in Fig. 3.2 in the Norton circuits and as yellow arrows. Combining Eq. 3.2 with Eq. 3.3, one arrives to

$$
\begin{aligned}
V(x_s,\omega) &= I_1(\omega)\cdot\frac{1}{2\pi}\int_{-\infty}^{\infty}\frac{sinc^2\left(\frac{k_x\Delta}{2}\right)}{D(k_x,\omega)}e^{-jk_x(x_s-x_{f1})}dk_x + I_2(\omega)\cdot\frac{1}{2\pi}\int_{-\infty}^{\infty}\frac{sinc^2\left(\frac{k_x\Delta}{2}\right)}{D(k_x,\omega)}e^{-jk_x(x_s-x_{f2})}dk_x \\
&\equiv I_1(\omega)Z(x_s-x_{f1},\omega) + I_2(\omega)Z(x_s-x_{f2},\omega) \\
Z(x,\omega) &\equiv \frac{1}{2\pi}\int_{-\infty}^{\infty}\frac{sinc^2\left(\frac{k_x\Delta}{2}\right)}{D(k_x,\omega)}e^{-jk_x x}dk_x.
\end{aligned}
\tag{3.4}
$$

For example when $x_s = x_{f1}$, $Z(x_s - x_{f1},\omega) = Z(0,\omega) = \frac{1}{2\pi}\int_{-\infty}^{\infty}\frac{sinc^2\left(\frac{k_x\Delta}{2}\right)}{D(k_x,\omega)}dk_x$. This is equal to the input impedance of the slot which is shown in Fig. 2.3 in Section 2.1.1. The figure shows that it's a function that increases over frequency in the considered bandwidth. When solving Eq. 3.4 in the time-domain, the inverse Fourier transform $\mathscr{F}^{-1}$ is required which entails integrating $Z(0,\omega)$ over frequency. However, based on Fig. 2.3 one would say that integrating until $2\,THz$ does not lead to an accurate evaluation of the integral since the figure suggest that $Z(0,\omega)$ has a significant amount of spectral content above $2\,THz$. Even so, integrating over higher frequencies will not be considered an option for two reasons:

- The width the slot, W_y, ought to be small w.r.t. the wavelength [10] for the formulation of the infinite slot presented in Eq. 2.5 and 2.6 to be valid. For example when $W_y = 10\,\mu m$, the slot width is approximately a quarter of the wavelength in medium 2 ($\varepsilon_{r,2} = 11.7$) at $2\,THz$ so including higher frequencies is not allowed.
- The photoconducting material itself is not fast enough for the associated currents and voltages to contain dynamics above $2THz$. Thus, it would be inappropriate to consider higher frequencies when formulating a method to solve for these currents and voltages. For example in Fig. 2.12b, at 2 THz the Fourier transform of the internal current is more than 10 dB below its maximum.

To mitigate the issues mentioned above, both sides of Eq. 3.4 shall be divided by the weighting function $W(\omega) = Z^2(0,\omega)$. This weighting function is chosen because as a result of the division by $W(\omega)$, $Z(x_s - x_{f1},\omega)$ and $Z(x_s - x_{f2},\omega)$ are now $\sim \frac{1}{Z(0,\omega)}$ which has most of its spectral content below $2THz$. An additional benefit would be that $\mathscr{F}\{\frac{1}{Z(0,\omega)}\}$ is more causal than $\mathscr{F}\{Z(0,\omega)\}$. Namely, in Fig. 2.4b the peak in the impulse response of $h_{self} = \mathscr{F}\{\frac{1}{Z(0,\omega)}\}$ occurs after $t = 0$ which would not have been the case for $\mathscr{F}\{Z(0,\omega)\}$ (when integrating until $2\,THz$). Note that it was not strictly necessary to utilize the weighting function in Chapter 2 since in Eq. 2.12a $\frac{1}{Z(0,\omega)}$ is already present. It was done for a fairer comparison and to stay consistent with the adopted methodologies in this chapter and the next one. Dividing both sides of Eq. 3.4 by $W(\omega) = Z^2(0,\omega)$ brings us to

$$
\frac{V(x_s,\omega)}{Z^2(0,\omega)} = I_1(\omega)\frac{Z(x_s-x_{f1},\omega)}{Z^2(0,\omega)} + I_2(\omega)\frac{Z(x_s-x_{f2},\omega)}{Z^2(0,\omega)}. \tag{3.5}
$$

The Norton circuits in Fig. 3.2 indicate that $i_1(t) = i_{impr,1}(t) - i_{int,1}(t)$ and $i_2(t) = i_{impr,2}(t) - i_{int,2}(t)$. In the frequency domain this implies $I_1(\omega) = I_{impr,1}(\omega) - I_{int,1}(\omega)$ and $I_2(\omega) = I_{impr,2}(\omega) - I_{int,2}(\omega)$. It produces

$$
\frac{V(x_s,\omega)}{Z^2(0,\omega)} = I_{impr,1}(\omega)\frac{Z(x_s-x_{f1},\omega)}{Z^2(0,\omega)} - I_{int,1}(\omega)\frac{Z(x_s-x_{f1},\omega)}{Z^2(0,\omega)} + I_{impr,2}(\omega)\frac{Z(x_s-x_{f2},\omega)}{Z^2(0,\omega)} - I_{int,2}(\omega)\frac{Z(x_s-x_{f2},\omega)}{Z^2(0,\omega)}. \tag{3.6}
$$

Performing an inverse Fourier transform on both sides of Eq. 3.6 to move towards the time-domain gives

$$
\begin{aligned}
v(x_s,t) * h_{weight}(t) = {} & i_{impr,1}(t) * h_{mutual}(x_s - x_{f1},t) - i_{int,1}(t) * h_{mutual}(x_s - x_{f1},t) \\
& + i_{impr,2}(t) * h_{mutual}(x_s - x_{f2},t) - i_{int,2}(t) * h_{mutual}(x_s - x_{f2},t),
\end{aligned}
\tag{3.7}
$$

with $h_{weight} \overset{\mathscr{F}}{\Longleftrightarrow} \frac{1}{Z^2(0,\omega)}$ and $h_{mutual}(x,t) \overset{\mathscr{F}}{\Longleftrightarrow} \frac{Z(x,\omega)}{Z^2(0,\omega)}$. Similar to what was done in Section 2.1.2, Eq. 3.7 shall be evaluated at an observation time $t = t_m$ and the time-signals are discretized so the convolution becomes a summation. One arrives to

$$\begin{aligned}
&\delta t \sum_{n=-\infty}^{m} v(x_s,t_n)h_{weight}(t_m-t_n) = \\
&\delta t \sum_{n=-\infty}^{m} i_{impr,1}(t_n)h_{mutual}(x_s-x_{f1},t_m-t_n) - \delta t \sum_{n=-\infty}^{m} i_{int,1}(t_n)h_{mutual}(x_s-x_{f1},t_m-t_n) \\
+&\delta t \sum_{n=-\infty}^{m} i_{impr,2}(t_n)h_{mutual}(x_s-x_{f2},t_m-t_n) - \delta t \sum_{n=-\infty}^{m} i_{int,2}(t_n)h_{mutual}(x_s-x_{f2},t_m-t_n).
\end{aligned} \tag{3.8}$$

Dividing out δt and separating the last terms ($n=m$) of the summations involving $v(x_s,t_n)$, $i_{int,1}(t_n)$ and $i_{int,2}(t_n)$ gives

$$\begin{aligned}
&\sum_{n=-\infty}^{m-1} v(x_s,t_n)h_{weight}(t_m-t_n) + v(x_s,t_m)h_{weight}(0) = \\
&\sum_{n=-\infty}^{m} i_{impr,1}(t_n)h_{mutual}(x_s-x_{f1},t_m-t_n) - \sum_{n=-\infty}^{m-1} i_{int,1}(t_n)h_{mutual}(x_s-x_{f1},t_m-t_n) - i_{int,1}(t_m)h_{mutual}(x_s-x_{f1},0) \\
+&\sum_{n=-\infty}^{m} i_{impr,2}(t_n)h_{mutual}(x_s-x_{f2},t_m-t_n) - \sum_{n=-\infty}^{m-1} i_{int,2}(t_n)h_{mutual}(x_s-x_{f2},t_m-t_n) - i_{int,2}(t_m)h_{mutual}(x_s-x_{f2},0).
\end{aligned} \tag{3.9}$$

The update rule given in Eq. 2.19 is also applicable here, after some slight adjustments. In Appendix C, one ought to replace $i_{int}(t)$, $v(t)$ and $e^{-4ln2\frac{t''^2}{\tau_p^2}}$ with $i_{int}(x_s,t)$, $v(x_s,t)$ and $e^{-4ln2\frac{(t''-t_{delay}(x_s))^2}{\tau_p^2}}$ respectively, in Eq. C.1. Afterwards one can perform exactly the same steps that are described in remaining parts of Appendix C to arrive to

$$i_{int}(x_s,t_m) = e^{-\frac{\delta t}{\tau_c}} e^{-\frac{\delta t}{\tau_s}} \cdot i_{int}(x_s,t_{m-1}) + v(x_s,t_m)\cdot g(x_s,t_m) \tag{3.10a}$$

$$g(x_s,t_m) = A\cdot(\delta t)^2 \frac{q_e^2}{m_{e,GaAs}} \frac{W_z\cdot\Delta}{W_y} \sum_{n=-\infty}^{m} e^{-4ln2\frac{\left(t_n-t_{delay}(x_s)\right)^2}{\tau_p^2}} e^{-\frac{t_m-t_n}{\tau_c}}, \tag{3.10b}$$

Where $x_s \in \{x_{f1}, x_{f2}\}$ (as stated earlier), $i_{int,1}(t_m) \equiv i_{int}(x_{f1},t_m)$ and $i_{int,2}(t_m) \equiv i_{int}(x_{f2},t_m)$.
Furthermore, the short-hand notations $(a\star b)(t_m) \equiv \sum_{n=-\infty}^{m} a(t_n)b(t_m-t_n)$,
$(a\star b)(t_{m-1}) \equiv \sum_{n=-\infty}^{m-1} a(t_n)b(t_m-t_n)$ and $h_{mutual}(x,t) \equiv h_{mutual}^{x}(t)$ shall be adopted where needed for brevity of the expressions. Incorporating this with Eq. 3.9 results in

$$\begin{aligned}
&\sum_{n=-\infty}^{m-1} v(x_s,t_n)h_{weight}(t_m-t_n) + v(x_s,t_m)h_{weight}(0) = \\
&(i_{impr,1}\star h_{mutual}^{x_s-x_{f1}})(t_m) - (i_{int,1}\star h_{mutual}^{x_s-x_{f1}})(t_{m-1}) - e^{-\frac{\delta t}{\tau_c}} e^{-\frac{\delta t}{\tau_s}} \cdot i_{int,1}(t_{m-1}) h_{mutual}^{x_s-x_{f1}}(0) - v(x_{f1},t_m)\cdot g(x_{f1},t_m) h_{mutual}^{x_s-x_{f1}}(0) \\
+&(i_{impr,2}\star h_{mutual}^{x_s-x_{f2}})(t_m) - (i_{int,2}\star h_{mutual}^{x_s-x_{f2}})(t_{m-1}) - e^{-\frac{\delta t}{\tau_c}} e^{-\frac{\delta t}{\tau_s}} \cdot i_{int,2}(t_{m-1}) h_{mutual}^{x_s-x_{f2}}(0) - v(x_{f2},t_m)\cdot g(x_{f2},t_m) h_{mutual}^{x_s-x_{f2}}(0).
\end{aligned} \tag{3.11}$$

Bringing all terms containing voltages at the observation time t_m to the left-hand side and the remaining terms to the right-hand side produces

$$\begin{aligned}
&v(x_s,t_m)h_{weight}(0) + v(x_{f1},t_m)\cdot g(x_{f1},t_m) h_{mutual}^{x_s-x_{f1}}(0) + v(x_{f2},t_m)\cdot g(x_{f2},t_m) h_{mutual}^{x_s-x_{f2}}(0) = \\
&(i_{impr,1}\star h_{mutual}^{x_s-x_{f1}})(t_m) - (i_{int,1}\star h_{mutual}^{x_s-x_{f1}})(t_{m-1}) - e^{-\frac{\delta t}{\tau_c}} e^{-\frac{\delta t}{\tau_s}} \cdot i_{int,1}(t_{m-1}) h_{mutual}^{x_s-x_{f1}}(0) \\
+&(i_{impr,2}\star h_{mutual}^{x_s-x_{f2}})(t_m) - (i_{int,2}\star h_{mutual}^{x_s-x_{f2}})(t_{m-1}) - e^{-\frac{\delta t}{\tau_c}} e^{-\frac{\delta t}{\tau_s}} \cdot i_{int,2}(t_{m-1}) h_{mutual}^{x_s-x_{f2}}(0) - \sum_{n=-\infty}^{m-1} v(x_s,t_n)h_{weight}(t_m-t_n).
\end{aligned} \tag{3.12}$$

Since $x_s \in \{x_{f1}, x_{f2}\}$, Eq. 3.12 actually represents two equations. One for $x_s = x_{f1}$ and for $x_s = x_{f2}$. In these equations, $v(x_{f1}, t_m)$ and $v(x_{f2}, t_m)$ are the unknown quantities to be solved for. The system of equations from Eq. 3.12 can be compactly expressed via matrices and vectors:

$$\Big[h_{weight}(0)\boldsymbol{I} + \boldsymbol{H}(t_m)\Big]\boldsymbol{v}(t_m) = \boldsymbol{C_{impr}}(t_m) - \boldsymbol{C_{int}}(t_{m-1}) - \boldsymbol{C_{weight}}(t_{m-1}). \tag{3.13}$$

Where the matrices and vectors are defined in the following manner

$$\boldsymbol{v}(t_m) = \begin{bmatrix} v(x_{f1}, t_m) \\ v(x_{f2}, t_m) \end{bmatrix}, \quad \boldsymbol{I} = \begin{bmatrix} 1 & 0 \\ 0 & 1 \end{bmatrix}, \quad \boldsymbol{H}(t_m) = \begin{bmatrix} g(x_{f1}, t_m)h_{self}(0) & g(x_{f2}, t_m)h^{d_x}_{mutual}(0) \\ g(x_{f1}, t_m)h^{d_x}_{mutual}(0) & g(x_{f2}, t_m)h_{self}(0) \end{bmatrix} \tag{3.14a}$$

$$\boldsymbol{C_{impr}}(t_m) = \begin{bmatrix} (i_{impr,1} \star h_{self})(t_m) + (i_{impr,2} \star h^{d_x}_{mutual})(t_m) \\ (i_{impr,1} \star h^{d_x}_{mutual})(t_m) + (i_{impr,2} \star h_{self})(t_m) \end{bmatrix} \tag{3.14b}$$

$$\boldsymbol{C_{int}}(t_{m-1}) = \begin{bmatrix} (i_{int,1} \star h_{self})(t_{m-1}) + (i_{int,2} \star h^{d_x}_{mutual})(t_{m-1}) + e^{-\frac{\delta t}{\tau_c}} e^{-\frac{\delta t}{\tau_s}} \cdot \left[i_{int,1}(t_{m-1})h_{self}(0) + i_{int,2}(t_{m-1})h^{d_x}_{mutual}(0)\right] \\ (i_{int,1} \star h^{d_x}_{mutual})(t_{m-1}) + (i_{int,2} \star h_{self})(t_{m-1}) + e^{-\frac{\delta t}{\tau_c}} e^{-\frac{\delta t}{\tau_s}} \cdot \left[i_{int,1}(t_{m-1})h^{d_x}_{mutual}(0) + i_{int,2}(t_{m-1})h_{self}(0)\right] \end{bmatrix} \tag{3.14c}$$

$$\boldsymbol{C_{weight}}(t_{m-1}) = \begin{bmatrix} \sum_{n=-\infty}^{m-1} v(x_{f1}, t_n)h_{weight}(t_m - t_n) \\ \sum_{n=-\infty}^{m-1} v(x_{f2}, t_n)h_{weight}(t_m - t_n) \end{bmatrix}. \tag{3.14d}$$

In Eq. 3.14, $h_{self}(t)$ appears because $h_{mutual}(x,t)$ reduces to $h_{self}(t)$ when $x = 0$. Also, when the spatial argument x is not equal to zero, $h_{mutual}(x,t)$ reduces to $h_{mutual}(d_x,t)$ in Eq. 3.14 since $h_{mutual}(x,t) \overset{\mathscr{F}}{\Longleftrightarrow} \frac{Z(x,\omega)}{Z^2(0,\omega)}$ and $Z(\pm(x_{f1} - x_{f2}),\omega) = Z(|x_{f1} - x_{f2}|,\omega) = Z(d_x,\omega)$ (demonstrated in Appendix D). The system presented in Eq. 3.13 can be solved for $\boldsymbol{v}(t_m)$ by the inverting the 2 x 2 matrix $h_{weight}(0)\boldsymbol{I} + \boldsymbol{H}(t_m)$:

$$\boldsymbol{v}(t_m) = \Big(h_{weight}(0)\boldsymbol{I} + \boldsymbol{H}(t_m)\Big)^{-1}\Big[\boldsymbol{C_{impr}}(t_m) - \boldsymbol{C_{int}}(t_{m-1}) - \boldsymbol{C_{weight}}(t_{m-1})\Big]. \tag{3.15}$$

Also here, before the lasers arrive, the time-varying voltages and the internal currents at the photoconducting gaps ($v(x_{f1},t)$, $v(x_{f2},t)$, $i_{int,1}(t)$ and $i_{int,2}(t)$) are considered to be zero. Thus, if a time instance $t_m = t_{start}$ is early enough such that the lasers haven't arrived yet, $\boldsymbol{v}(t_{start})$ can be found via Eq. 3.15 by putting $\boldsymbol{C_{weight}}(t_{m-1})$ and $\boldsymbol{C_{int}}(t_{m-1})$ equal to zero. This can be done since those vectors only contain voltage terms and internal current terms related to times before $t_m = t_{start}$. Subsequently, one should apply the update rule for the internal currents at the feeds to obtain $i_{int,1}(t_{start})$ and $i_{int,2}(t_{start})$. Then, $\boldsymbol{v}(t_{start})$, $i_{int,1}(t_{start})$ and $i_{int,2}(t_{start})$ can be combined with Eq. 3.15 to find $\boldsymbol{v}(t_{start+1})$ which can be used to acquire $i_{int,1}(t_{start+1})$ and $i_{int,2}(t_{start+1})$. One can utilize these quantities to obtain $\boldsymbol{v}(t_{start+2})$... and so on. Continuing this marching-on-in-time procedure one can fully obtain $\boldsymbol{v}(t)$, $i_{int,1}(t)$ and $i_{int,2}(t)$. Afterwards, the load currents can be found since $i_1(t) = i_{impr,1}(t) - i_{int,1}(t)$ and $i_2(t) = i_{impr,2}(t) - i_{int,2}(t)$ (impressed currents are known beforehand via Eq. 3.1).

3.1.3 Voltage Outside of the Source Regions

Now that one has solved for the source quantities in Section 3.1.2, the voltage at locations outside of the source regions, $v(x,t)$, can be determined.

Also here, the voltage shall be evaluated at discrete points along the slot: $x_k = k \cdot \delta x$, $k \in \mathbb{I}$. The voltage at a location x_k is defined as its spatial average over the discretization length δx. Thus, Eq. 2.22 still holds. However, the Fourier transform related to the current, $I_e(k_x,\omega)$, is different in this chapter and it is given by Eq. 3.3. Combining Eq. 2.22 and Eq. 3.3 produces

$$
\begin{aligned}
V(x_k,\omega) &= I_1(\omega)\cdot\frac{1}{2\pi}\int_{-\infty}^{\infty}\frac{sinc\left(\frac{k_x\Delta}{2}\right)sinc\left(\frac{k_x\delta x}{2}\right)}{D(k_x,\omega)}e^{-jk_x\cdot(x_k-x_{f1})}dk_x + I_2(\omega)\cdot\frac{1}{2\pi}\int_{-\infty}^{\infty}\frac{sinc\left(\frac{k_x\Delta}{2}\right)sinc\left(\frac{k_x\delta x}{2}\right)}{D(k_x,\omega)}e^{-jk_x\cdot(x_k-x_{f2})}dk_x \\
&\equiv I_1(\omega)\tilde{Z}(x_k-x_{f1},\omega) + I_2(\omega)\tilde{Z}(x_k-x_{f2},\omega) \\
\tilde{Z}(x,\omega) &\equiv \frac{1}{2\pi}\int_{-\infty}^{\infty}\frac{sinc\left(\frac{k_x\Delta}{2}\right)sinc\left(\frac{k_x\delta x}{2}\right)}{D(k_x,\omega)}e^{-jk_xx}dk_x.
\end{aligned}
\tag{3.16}
$$

In Eq. 3.16, $\tilde{Z}(x_k-x_{f1},\omega)$ and $\tilde{Z}(x_k-x_{f2},\omega)$ represent mutual impedances that relate the average voltage at a position x_k, to the currents generated at x_{f1} and x_{f2}, respectively. In fact, $\tilde{Z}(x_k-x_{f1},\omega)$ and $\tilde{Z}(x_k-x_{f2},\omega)$ depend only on the distances to the sources $|x_k-x_{f1}|$ and $|x_k-x_{f2}|$, respectively (discussed in Appendix D). For similar reasons as in Section 3.1.2, both sides of Eq. 3.16 are divided the weighting function $\tilde{Z}^2(0,\omega) = (\tilde{Z}(0,\omega))^2 = (\tilde{Z}(x=0,\omega))^2$. This gives

$$
\frac{V(x_k,\omega)}{\tilde{Z}^2(0,\omega)} = I_1(\omega)\cdot\frac{\tilde{Z}(x_k-x_{f1},\omega)}{\tilde{Z}^2(0,\omega)} + I_2(\omega)\cdot\frac{\tilde{Z}(x_k-x_{f2},\omega)}{\tilde{Z}^2(0,\omega)}. \tag{3.17}
$$

Next, an inverse Fourier transform on both sides of Eq. 3.17 is performed to move towards the time-domain. It results in

$$
v(x_k,t) * \tilde{h}_{weight}(t) = i_1(t) * \tilde{h}_{mutual}(x_k-x_{f1},t) + i_2(t) * \tilde{h}_{mutual}(x_k-x_{f2},t), \tag{3.18}
$$

where $\tilde{h}_{weight}(t) \overset{\mathscr{F}}{\Longleftrightarrow} \frac{1}{\tilde{Z}^2(0,\omega)}$ and $\tilde{h}_{mutual}(x,t) \overset{\mathscr{F}}{\Longleftrightarrow} \frac{\tilde{Z}(x,\omega)}{\tilde{Z}^2(0,\omega)}$. Also, $i_1(t)$ and $i_2(t)$ are the source currents that were obtained in Section 3.1.2. Even though it is not straightforward to give an interpretation to $\tilde{h}_{mutual}$ itself, $\mathscr{F}^{-1}\{\tilde{Z}(x_k-x_s,\omega)\}$, $x_s \in \{x_{f1},x_{f2}\}$ does have a physical interpretation. It represents an impulse response that relates the average voltage observed at a position x_k, $v(x_k,t)$, to a source current located at x_s. Evaluating Eq. 3.18 at an observation time $t=t_m$ and applying a time-discretization to the convolution of the signals brings us to

$$
\delta t\sum_{n=-\infty}^{m} v(x_k,t_n)\tilde{h}_{weight}(t_m-t_n) = \delta t\sum_{n=-\infty}^{m} i_1(t_n)\tilde{h}_{mutual}(x_k-x_{f1},t_m-t_n) + \delta t\sum_{n=-\infty}^{m} i_2(t_n)\tilde{h}_{mutual}(x_k-x_{f2},t_m-t_n). \tag{3.19}
$$

Finally, after dividing out δt, rearranging terms and separating the last term of the summation involving $v(x_k,t_n)$ in Eq. 3.19 one has found an update rule for the voltage along the slot

$$
\begin{aligned}
v(x_k,t_m) = \frac{1}{\tilde{h}_{weight}(0)}\Bigg\{ &\sum_{n=-\infty}^{m} i_1(t_n)\tilde{h}_{mutual}(x_k-x_{f1},t_m-t_n) + \sum_{n=-\infty}^{m} i_2(t_n)\tilde{h}_{mutual}(x_k-x_{f2},t_m-t_n) \\
&- \sum_{n=-\infty}^{m-1} v(x_k,t_n)\tilde{h}_{weight}(t_m-t_n)\Bigg\}.
\end{aligned}
\tag{3.20}
$$

Before the laser arrives, $v(x_{f1},t)$ and $v(x_{f2},t)$ are considered to be zero. Therefore, the time-varying voltage $v(x_k,t)$ at other locations along the slot is also zero before arrival of the laser since the voltage waves originate from the feeds. Thus, if a time instance $t_m = t_{start}$ is early enough such that the laser hasn't arrived yet, $v(x_k,t_{start})$ can be found via Eq. 3.20 by putting the summation involving $v(x_k,t_n)$ on the right-hand side equal to zero. Subsequently, $v(x_k,t_{start})$ ought to be plugged into Eq. 3.20 to obtain $v(x_k,t_{start+1})$, which can be used to find $v(x_k,t_{start+2})$... and so on. By implementing this marching-on-in-time procedure for every position x_k the voltage along the entire slot as a function of time is obtained.

3.2 Transmission Line Equivalent Circuit

Also for the case of two photoconducting feeds within an infinite slot, a transmission line equivalent circuit can be formulated. To realize that, let's consider Eq. 3.4 with $x_s = x_{f1}$

$$V(x_{f1},\omega) = I_1(\omega)Z(0,\omega) + I_2(\omega)Z(d_x,\omega), \tag{3.21}$$

where $Z(d_x,\omega) = Z(x_{f1}-x_{f2},\omega) = Z(|x_{f1}-x_{f2}|,\omega)$ (see Appendix D). In Fig. 3.3 the real and imaginary part of the mutual impedance $Z(d_x,\omega)$ is shown for several distances d_x. The results are presented for a slot with a width $W_y = 10\,\mu m$ and a feed length $\Delta = 4.5\,\mu m$. For both the real and the imaginary part, the mutual impedance consists of decaying oscillations in the frequency domain. The amplitudes of these oscillations decrease with increasing distance. Therefore, a voltage which is related to a current at a distances d_x via $Z(d_x,\omega)$, couples less to that current when the distance increases. Furthermore, one should note that the oscillations in Fig. 3.3 decay with increasing frequency because higher frequencies attenuate more when they propagate according to Fig. 2.8b. Thus, those frequencies are less able to couple voltage and currents at a certain distance from one another along the slot.

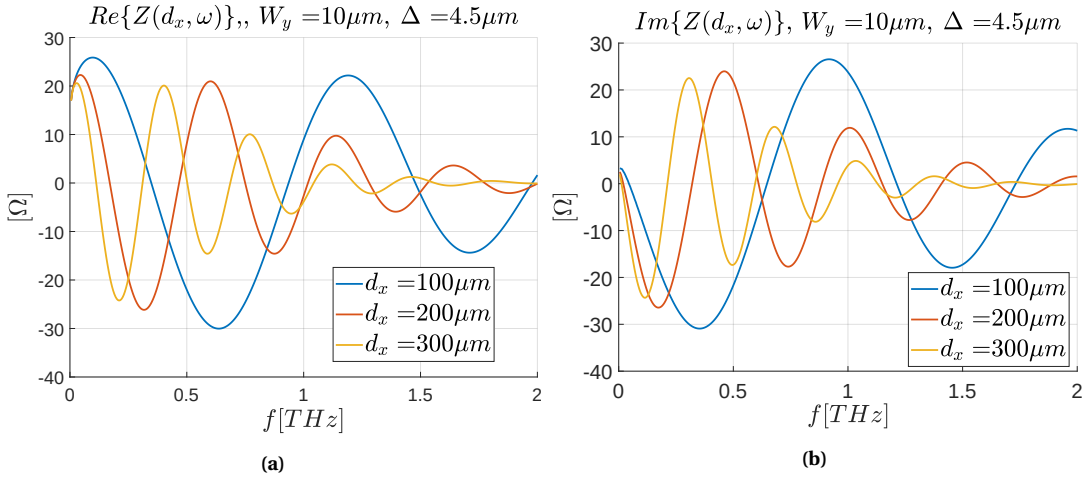

Figure 3.3: (a) Real and (b) imaginary of the mutual impedance of an infinite slot for several distances d_x. The slot has a width $W_y = 10\,\mu m$ and the feeds have a length $\Delta = 4.5\,\mu m$.

According to Eq. 3.21, the voltage at x_{f1}, $V(x_{f1},\omega)$, couples to the current at x_{f1} via the term $I_1(\omega)Z(0,\omega)$. In Section 2.2 it was already shown that the input impedance $Z(0,\omega)$ can be regarded as the impedance seen from one side of a transformer that couples the feed to two infinite, parallel transmission lines. The transmission lines have a characteristic impedance of $Z_{0,s} = -\frac{2j}{D'_s(k_{xp})}$ and the transformer has a turns ratio $n_\delta = sinc(\frac{k_{xp}\Delta}{2})$ [21]. This led to the equivalent circuit depicted in Fig. 2.7. However when there are two feeds, there is an additional term, $I_2(\omega)Z(d_x,\omega)$. If the distance between the feeds, d_x, is sufficiently large then the the mutual impedance $Z(d_x,\omega)$ can be approximated with its residue contribution

$$Z(d_x,\omega) = \frac{1}{2\pi}\int_{-\infty}^{\infty} \frac{sinc^2\left(\frac{k_x\Delta}{2}\right)}{D(k_x,\omega)} e^{-jk_x d_x} dk_x \cong -j\frac{sinc^2\left(\frac{k_{xp}\Delta}{2}\right)}{D'(k_{xp},\omega)} e^{-jk_{xp}\cdot d_x}, \quad d_x\ large. \tag{3.22}$$

For the voltage at x_{f1} this gives

$$V(x_{f1},\omega) \cong I_1(\omega)Z(0,\omega) + I_2(\omega)\cdot -j\frac{sinc^2\left(\frac{k_{xp}\Delta}{2}\right)}{D'(k_{xp},\omega)} e^{-jk_{xp}\cdot d_x}, \quad d_x\ large. \tag{3.23}$$

The term with d_x in Eq. 3.23 contains a complex exponential where the exponent has a propagation constant k_{xp} multiplied with the distance between the feeds, d_x. Also, the exponential is multiplied with $I_2(\omega)\cdot -j\frac{sinc^2\left(\frac{k_{xp}\Delta}{2}\right)}{D'(k_{xp},\omega)}$. This indicates a voltage wave with complex amplitude $I_2(\omega)\cdot -j\frac{sinc^2\left(\frac{k_{xp}\Delta}{2}\right)}{D'(k_{xp},\omega)}$, propagating along a transmission line with propagation constant k_{xp}. This propagation constant is the same as for the transmission lines which are presented in Fig. 2.7. This indicates that the feed at x_{f1} couples to the feed at x_{f2} via a propagating voltage wave along a transmission line. The reasoning that was used from Eq. 3.21 till Eq. 3.23 could also be applied to the case where $x_s = x_{f2}$. One would then see that the feed at x_{f2} couples to the feed

at x_{f1} also via a voltage wave propagating along a transmission line.

Based on the argument presented in this section, the equivalent circuit from Fig. 2.7 can be adjusted such that it represents the case of two photoconducting feeds within an infinite slot. The result is shown in Fig. 3.4.

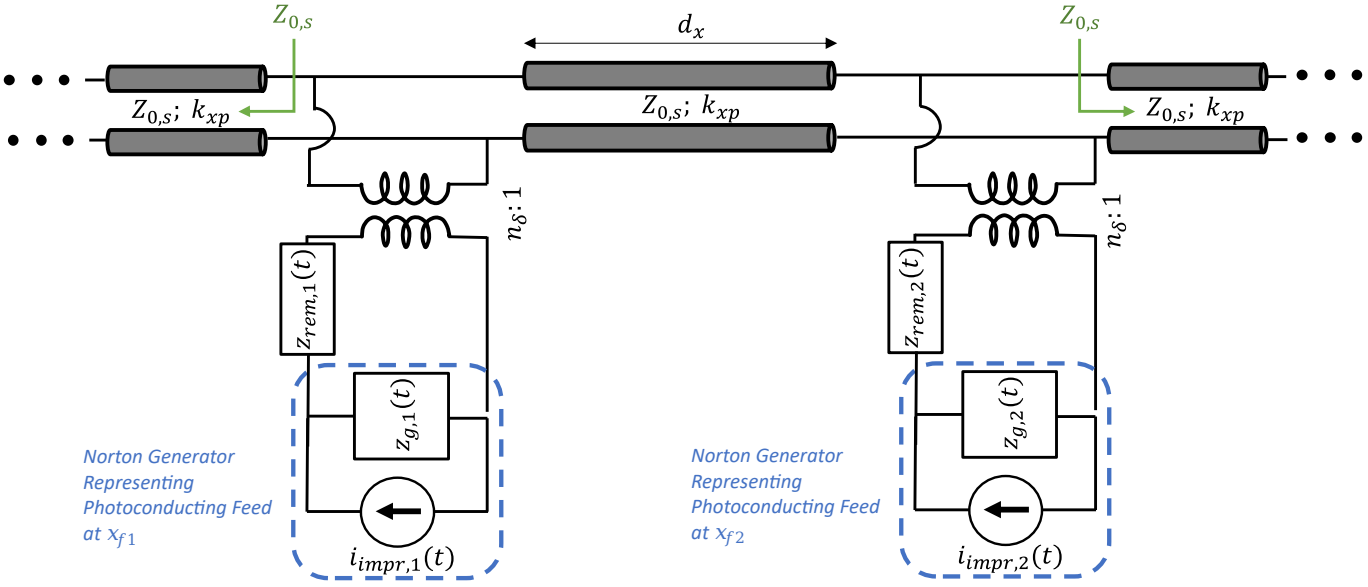

Figure 3.4: Transmission line equivalent circuit describing two photoconducting feeds placed within an infinite slot. Both feeds are represented with a Norton equivalent circuit coupled to transmission lines via a transformer. The transformer has a turns ratio n_δ. Furthermore, the transmission lines have a characteristic impedance $Z_{0,s}$ and a propagation constant k_{xp}.

Approximating the mutual impedance with its residue contribution for large distances allows for a much faster numerical implementation. Together with the associated transmission line equivalent circuit it also provides us with a mental picture which is slightly different compared to Section 2.2. Each photoconducting feeds acts as a current source that excites voltage waves. These voltage waves propagates along the slot via either an infinite transmission, or a transmission line of length d_x towards the other feed. A voltage wave that arrives at another photoconducting feed can interact with it if that feed is still conductive. This interaction entails an increase in the internal current in the photoconducting gap. Depending on how the internal current changes relative to the impressed current at the feed, a voltage reversal can occur to part of the wave. The other part of the voltage wave is transmitted and continues to propagate along an infinite transmission line. In Section 3.3 this concept regarding the voltage reversal shall be clarified with an example. The propagation itself of the voltage waves is affected in the same manner as described in Section 2.2 by the dispersivity of the slot in terms of propagation velocity and attenuation. The waves attenuate as they move, and their shape changes due to the dispersivity.

3.3 Results of the Marching-On Procedure

3.3.1 Voltage Wave Propagation Along the Slot

An example of how the voltage waves propagate when the slot is excited by both feeds is illustrated in Fig. 3.5. The photoconducting feeds have a length $\Delta = 10\,\mu m$, are excited at the same time ($t_{delay,j} = 0, j \in \{1,2\}$), with a bias of $30V$ within an infinite slot that has a width $W_y = 10\,\mu m$. One can see that from both feed locations (indicated with red dots), a wave emerges. These waves then divide themselves into two equal wavefronts, one moving to the left, one moving to the right. The wavefronts that move toward each other combine at the origin resulting in a large peak which subsequently separates itself into the original wavefronts moving away from each other.

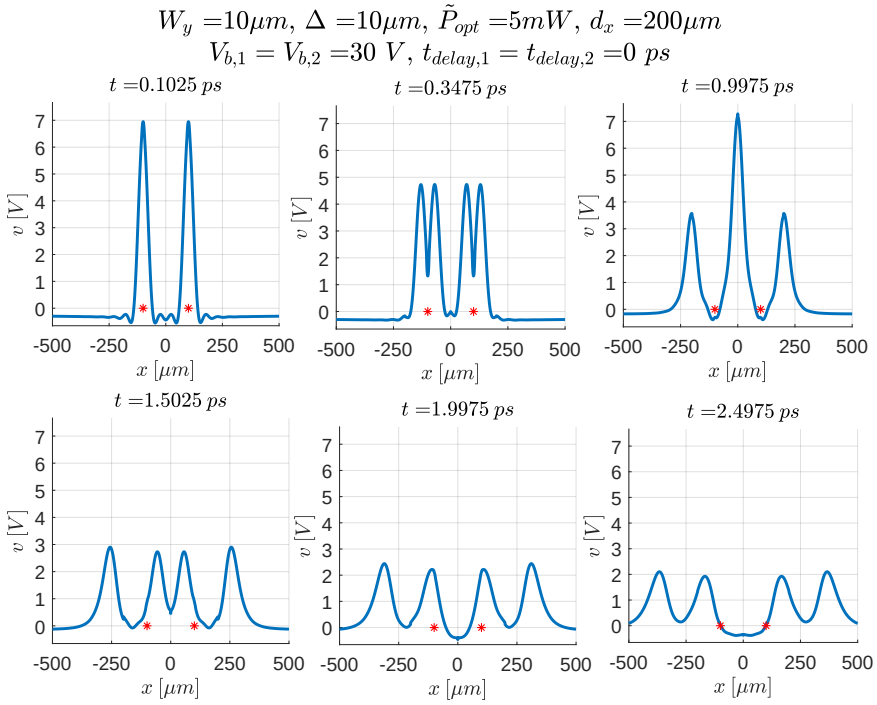

Figure 3.5: Propagation of the voltage waves in an infinite slot with a width $W_y = 10\,\mu m$, excited by two pulsed, photoconducting feeds. The feeds are separated by a distance $d_x = 200\,\mu m$, have a length $\Delta = 10\,\mu m$ and are both biased with 30 V. The locations of the feeds are indicated with red dots in the graphs.

3.3.2 Voltage and Current in the Photoconducting Gaps

For the case depicted in Fig. 3.5, the voltages and currents associated to both feeds are shown in Fig. 3.6. Since the feeds are excited in exactly the same manner, the voltages and currents at $x = x_{f1}$ and $x = x_{f2}$ are identical. Unlike a typical voltage curve for a single feed (e.g. the one in Fig. 2.11b), the voltages in Fig. 3.6 have not one but two peaks. The first peak, around $t = 0.1ps$, corresponds to the initial excitation related to the incidence of the laser pulse. The second peak, around $t = 1.9ps$, represents the (attenuated) voltage wave from another feed that has arrived as illustrated in Fig. 3.5. Notice that the current does not contain a second peak around $t = 1.9ps$. This is the case because the photoconducting material is no longer conductive at that time and therefore a current cannot flow across the slot width anymore.

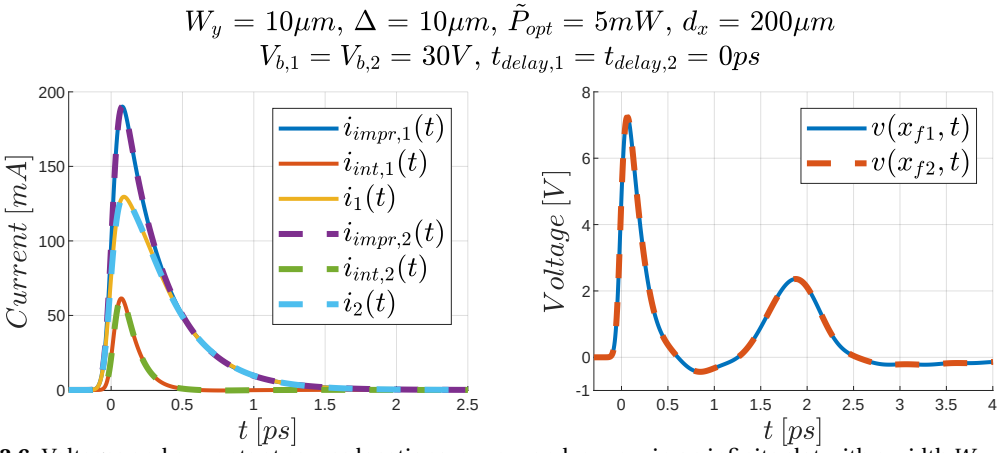

Figure 3.6: Voltages and currents at source locations $x = x_{f1}$ and $x = x_{f2}$ in an infinite slot with a width $W_y = 10\,\mu m$, excited by two pulsed, photoconducting feeds. The feeds are separated by a distance $d_x = 200\,\mu m$, have a length $\Delta = 10\,\mu m$ and are both biased with $30V$.

Also for two feeds, one can insert the Fourier transforms of the obtained time-quantities in the original equation (without weighting function), Eq. 3.4, to validate the procedure. The results of this for $x_s = x_{f1}$, with the same parameters as in Fig. 3.6, can be seen in Fig. 3.7 below. Since in this case both sources have the same currents and voltage, applying $x_s = x_{f2}$ instead would have produced identical curves as the ones in Fig. 3.7.

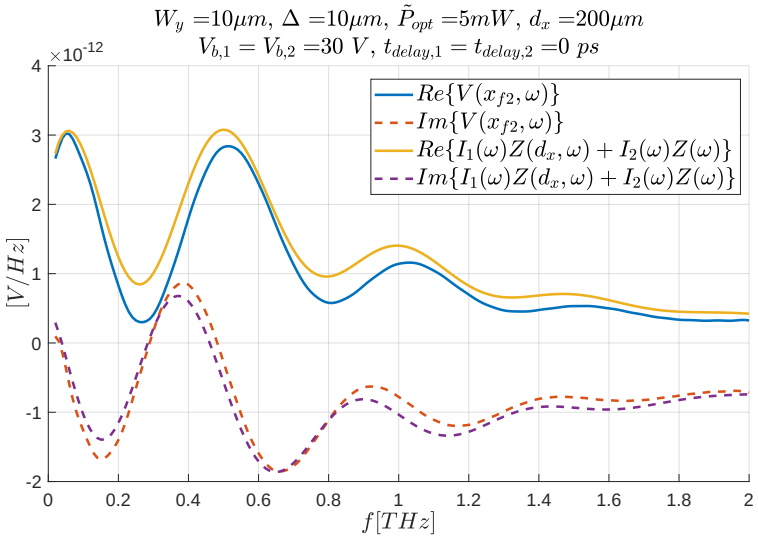

Figure 3.7: The Fourier transforms of the sources quantities, which are shown in Fig. 3.6, have been inserted in Eq. 3.4 to examine whether this original equation is satisfied.

The real part of the left-hand side and the right-hand side in Eq. 3.4 are synchronous in terms of shape across the entire band in Fig. 3.7. Ditto for the imaginary part. In terms of magnitude there are some discrepancies but overall Fig. 3.7 still indicates that Eq. 3.4 has been solved properly.

3.3.3 Voltage Reversal

It could occur that a voltage wave is (partially) reflected when it arrives at another feed. In some cases, the reflection includes a change in sign for the time-varying voltage. This phenomenon shall be referred to as "voltage reversal". For this to take place, two conditions have to be met:

1. The voltage wave arrives at a feed that is still conductive. It is necessary because in that case the two metals comprising the slot are connected with a finite conductivity. This is analogous to a wave propagating along a transmission line which encounters a non-perfect short circuit.

2. The internal current becomes higher than the impressed current at the feed that receives the wave. This entails that the direction of the (physical) load current flips with respect to the bias which allows for a voltage wave with opposite polarity (the reflected wave) to propagate.

In Fig. 3.8 a situation is depicted in which the feed at $x_{f2} = 75\mu m$ is excited $1.5ps$ later compared to the feed at $x_{f1} = -75\mu m$. The time shots show that a voltage wave moving to the right, originating from x_{f1}, arrives at x_{f2} around the time it is excited. Thus, the wave arrives when the feed is conductive (so condition 1 is met). Looking at the corresponding source voltages in Fig. 3.9, it is apparent that the voltage curve for x_{f2} contains only one peak, around $1.5ps$, instead of two. This peak has a larger amplitude compared to the excitation peak at x_{f1} around $0.1ps$. This is the case because the arrival time of the voltage wave originating from x_{f1} is such that it adds up coherently to the newly excited wave at x_{f2} as illustrated in Fig. 3.8. After the peak at x_{f2} splits itself into two, the wavefront moving to the right now has a larger amplitude compared to the one moving to the left due to this coherent addition. Furthermore, in Fig. 3.9 one can see that the internal current at x_{f2} is higher than the one at x_{f1} even though the impressed currents are equal. This is a consequence of the voltage wave from the feed at x_{f1} arriving at x_{f2} when that feed is conductive as stated earlier.

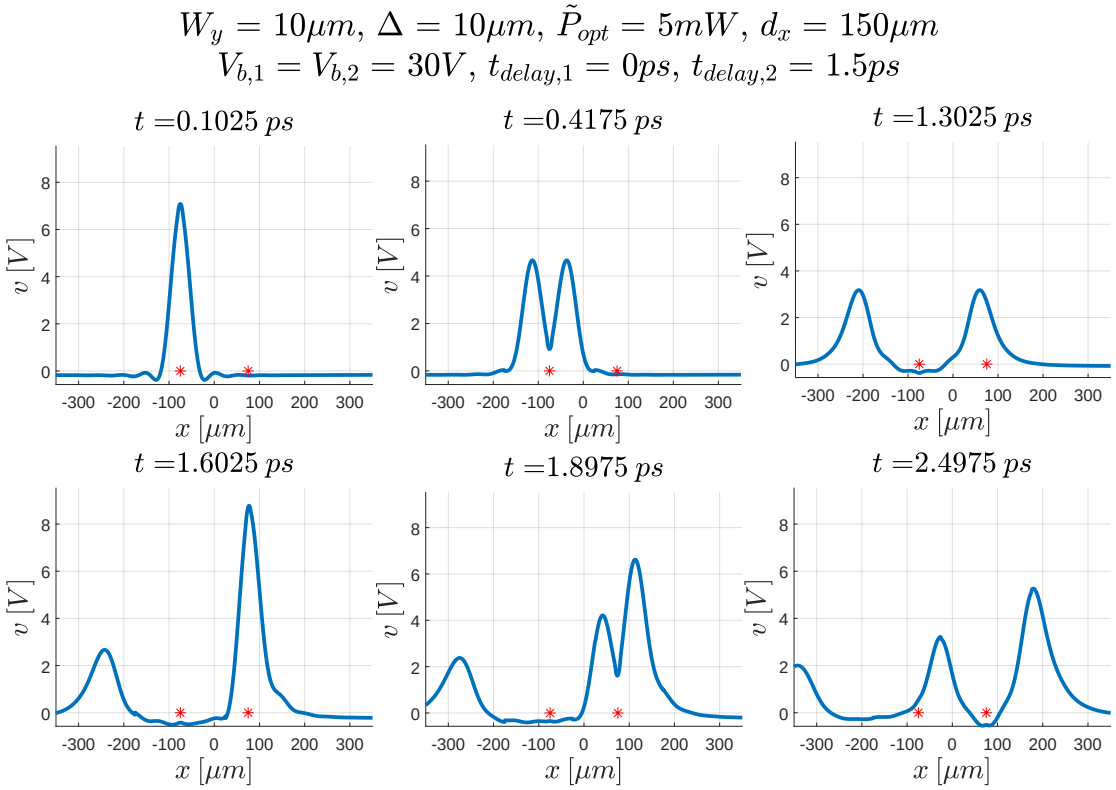

Figure 3.8: Propagation of the voltage waves in an infinite slot with a width $W_y = 10\,\mu m$, excited by two pulsed, photoconducting feeds. The feeds are separated by a distance $d_x = 200\,\mu m$, have a length $\Delta = 10\,\mu m$ and are both biased with $30V$. The locations of the feeds are indicated with red dots in the graphs. The feed at $x_{f2} = 75\mu m$ is excited with a laser centered around $t_{delay,2} = 1.5ps$.

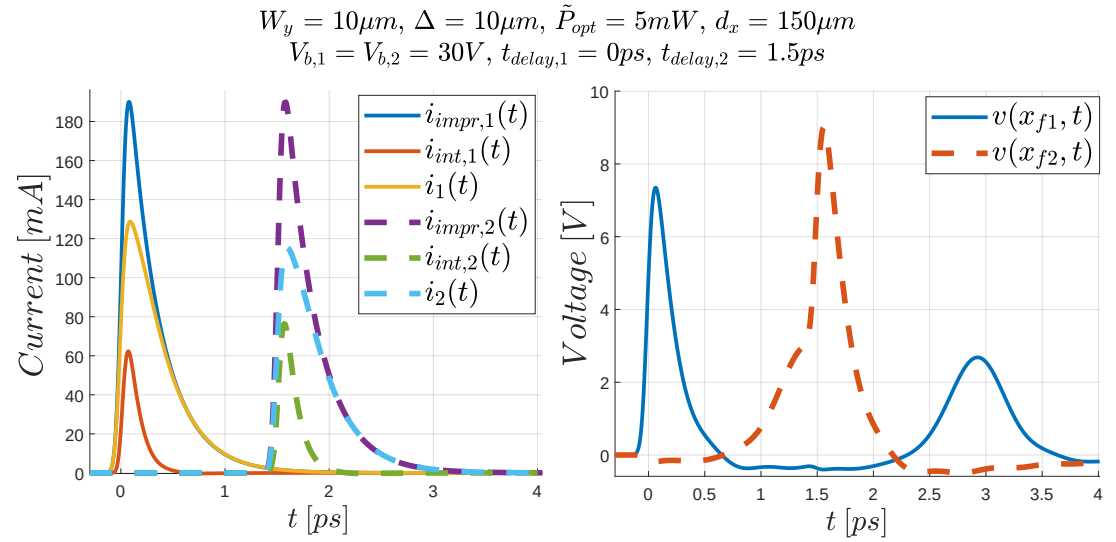

Figure 3.9: Voltages and currents at source locations $x = x_{f1}$ and $x = x_{f2}$ in an infinite slot with a width $W_y = 10\,\mu m$, excited by two pulsed, photoconducting feeds. The feeds are separated by a distance $d_x = 200\,\mu m$, have a length $\Delta = 10\,\mu m$ and are both biased with $30V$.

The example illustrated via Fig. 3.8 does not include a voltage reversal. As can be seen in Fig. 3.9, the internal current at x_{f2} does not go above the impressed current so the second condition is not met. To introduce a situation where a reversal is more likely to happen, one ought to increase the optical power. Namely, increas-

ing the optical power will decrease the generator impedance of the Norton equivalent circuit which leads to the internal current being closer to the impressed current as shown in Section 2.3.1. Furthermore, decreasing the bias at x_{f2} will also increase the likelihood of a reversal occurring. This is the case since reducing the bias diminishes the impressed current but it does not influence the conductivity. Therefore, the voltage wave emerging from x_{f1} will have a relatively higher impact with regard to enlarging the internal current at x_{f2}.

In Fig. 3.10 a situation is depicted where these changes have been applied and a voltage reversal does occur. One can observe from the figure that a voltage wave moving to the right, originating from x_{f1}, results in a reflected and a transmitted wave after an interaction with the feed at x_{f2}. The reflected wave propagates to the left with opposite polarity while the transmitted wave propagates to the right with the same polarity.
The associated currents in Fig. 3.11 reveal that indeed the internal current became higher than the impressed current at x_{f2}. The result is a load current with an opposite sign compared to the one at x_{f1}.

$$W_y = 10\mu m,\ \Delta = 10\mu m,\ \tilde{P}_{opt} = 74mW,\ d_x = 100\mu m$$
$$V_{b,1} = 30V,\ V_{b,2} = 6V,\ t_{delay,1} = 0ps,\ t_{delay,2} = 0.7ps,$$

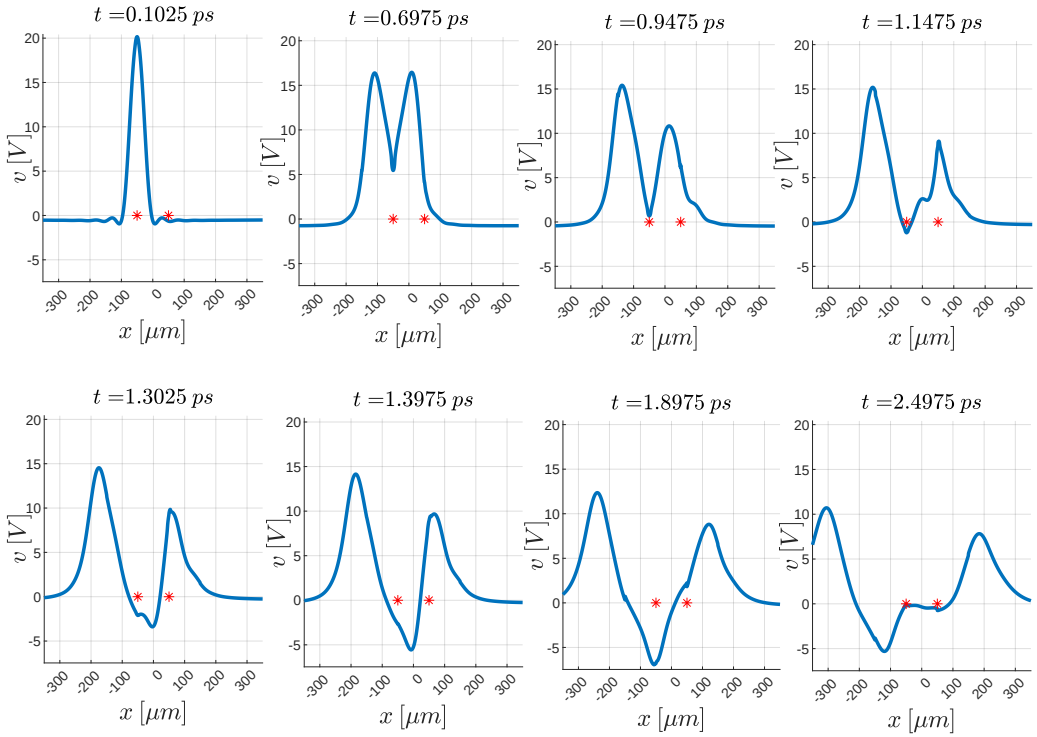

Figure 3.10: Propagation of the voltage waves in an infinite slot with a width $W_y = 10\,\mu m$, excited by two pulsed, photoconducting feeds. The feeds are separated by a distance $d_x = 100\,\mu m$ and have a length $\Delta = 10\,\mu m$. The feed at $x_{f1} = -50\mu m$ is biased with $V_{b,1} = 30V$ while the feed at $x_{f2} = 50\mu m$ is biased with $6V$. The locations of the feeds are indicated with red dots in the graphs. The feed at $x_{f2} = 50\mu m$ is excited with a laser centered around $t_{delay,2} = 0.7ps$.

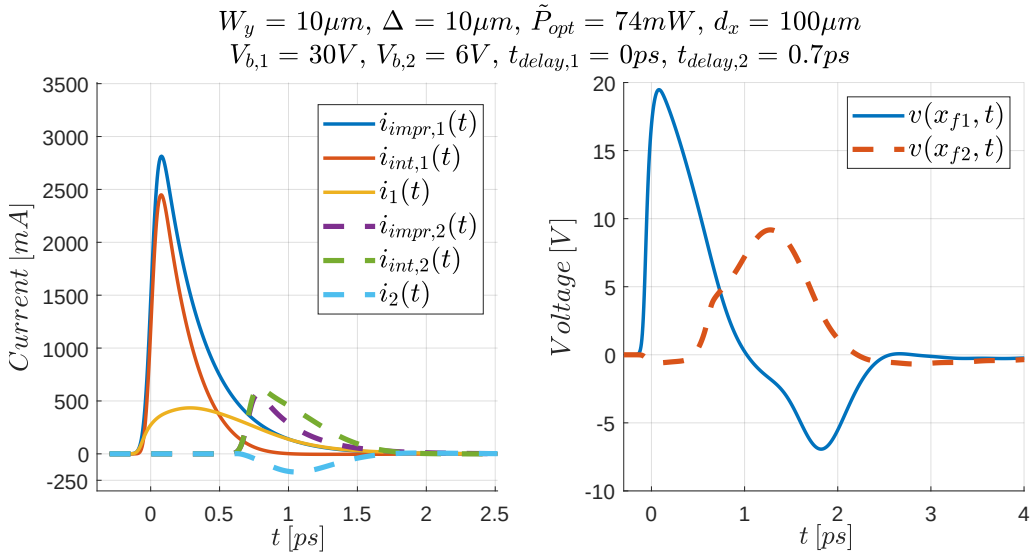

Figure 3.11: Voltages and currents at source locations $x = x_{f1}$ and $x = x_{f2}$ in an infinite slot with a width $W_y = 10\,\mu m$, excited by two pulsed, photoconducting feeds. The feeds are separated by a distance $d_x = 100\,\mu m$ and have a length $\Delta = 10\,\mu m$. The feed at $x_{f1} = -50\mu m$ is biased with $V_{b,1} = 30V$ while the feed at $x_{f2} = 50\mu m$ is biased with $6V$. The feed at $x_{f2} = 50\mu m$ is excited with a laser centered around $t_{delay,2} = 0.7ps$.

3.3.4 Limiting Behaviour for large Separation

When the separation distance d_x increases the influence of the coupling between the two feeds becomes less and less. In other words, the time-domain source quantities associated to each feed will get closer and closer to the solution of a single feed problem. This is illustrated in Fig. 3.12 and 3.13 where the internal current and voltage at x_{f2} are shown for several distances, respectively. The results for the case where the mutual coupling terms $h^{d_x}_{mutual}$ in Eq. 3.14 have been set to zero are also included. Excluding the mutual coupling produces practically the same curves that are depicted in Fig. 2.11. The sources are excited in the same manner so the results for x_{f1} are the same as the ones in Fig. 3.12 and 3.13.

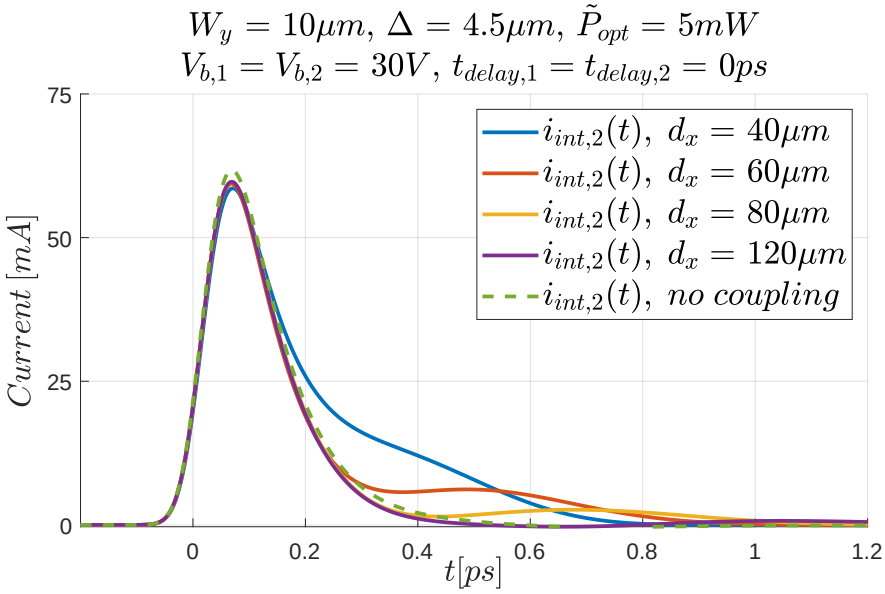

Figure 3.12: Internal current at the source location x_{f2} for several distances d_x. The internal current at x_{f2} for the case where there is no mutual coupling between the sources is also given.

The impressed current does not depend on the distance according to Eq. 3.1. Furthermore, the load current directly follows when the internal current and impressed current are known since $i_2(t) = i_{impr,2}(t) - i_{int,2}(t)$. Thus, only the internal current is shown in Fig. 3.12 for several distances d_x. It is important to realize that as the distance grows, the arrival of a voltage wave from another feed occurs at a later time. If the wave arrives when the feed is still conductive the internal current will increase as discussed earlier. This phenomenon can be recognized in Fig. 3.12. Initially, the curves behave in the same manner as the curve without mutual coupling, until the wave from another feed arrives which gives the internal current a boost (e.g. around $0.2ps$ for $d_x = 40\mu m$). For larger distances, this boost happens at a later time and it becomes less significant since the incoming wave has attenuated and the feed is less conductive.
For the voltages shown in Fig. 3.13 one can also observe that initially the curves follow the same trend as the one without mutual coupling until the voltage wave from another feed arrives. The arrival of such a wave results in an additional peak. The larger the distance, the later this peak shall arrive with a lower amplitude. Also here, as the distance grows the source quantity becomes more and more similar to the case without mutual coupling.

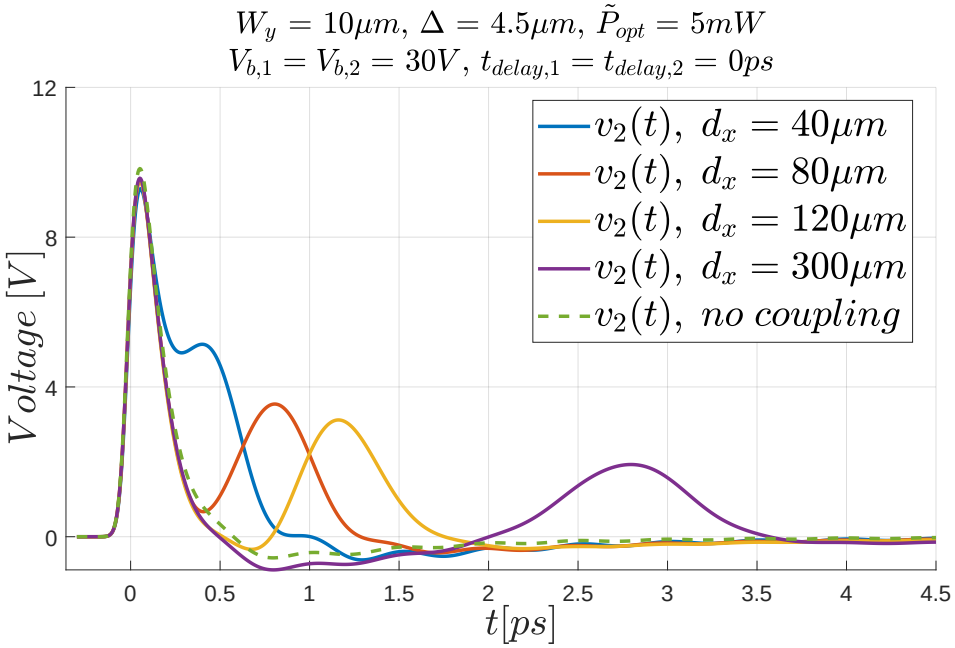

Figure 3.13: Time-varying voltage at the source location x_{f2} for several distances d_x. The voltage at x_{f2} for the case where there is no mutual coupling between the sources is also given.

Chapter 4

Slot Antenna Fed by a Pulsed Photo Conducting Source Excited over a Distributed Region

4.1 Formulation

4.1.1 Defining the Problem

In this chapter, the structure depicted in Fig. 4.1 below shall be studied. It consists of an infinite slot with a width W_y which is completely filled with photoconducting material that has a thickness W_z. The slot is placed at the interface between an air gap of length d_{air} and a semi-infinite ($z < -W_z$), non-magnetic, homogeneous medium with a relative permittivity of $\varepsilon_{r,rad}$. Above the air gap, a dielectric that's infinitely extended along the positive z-axis ($z > d_{air}$) is situated. This dielectric has a relative permittivity of $\varepsilon_{r,opt}$ and an optical, pulsed laser propagates through this medium before impinging on the photoconducting material via the air gap. The bottom of this dielectric has a saw-tooth shape cut to present a dielectric-air interface orthogonal to the laser pulse. The laser frees charged carriers which constitute a current along $\hat{y}$ because of the acceleration induced by the bias voltage V_b. Furthermore, the laser arrives with an angle θ_{opt} on the slot and it has a footprint l_x that is long in terms of the considered THz wavelengths.

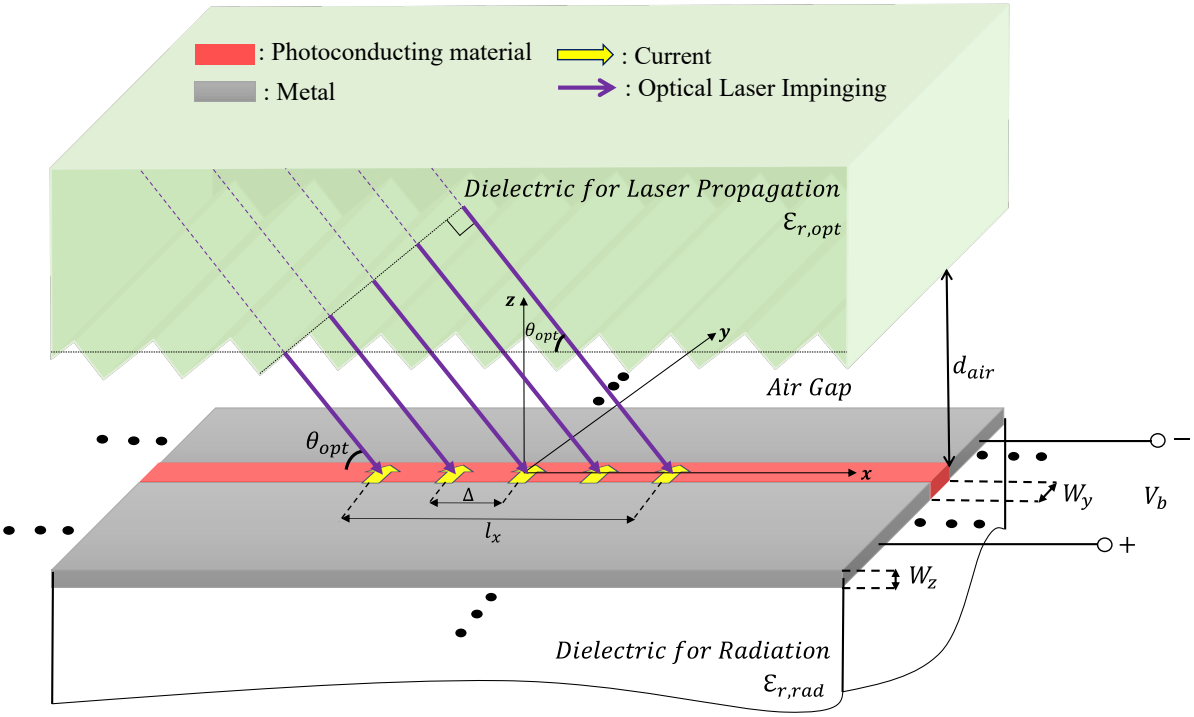

Figure 4.1: Stratification studied in this chapter consisting of an infinite slot placed between an air gap of length d_{air} and a semi-infinite medium with relative permittivity $\varepsilon_{r,rad}$. Above the air gap another semi-infinite dielectric is situated with relative permittivity $\varepsilon_{r,opt}$ through which an optical, pulsed laser propagates. The laser has a footprint l_x and it is incident onto the photoconducting material with an angle θ_{opt}.

The slot is discretized in sections, equal to length Δ as illustrated in Fig. 4.1. In this chapter, the objective is to determine the induced voltage in the active (source) region, $v(x_s, t)$, $x_s \in [-l_x/2, l_x/2]$, as well as the voltage at all other positions along the slot, represented by $v(x, t)$.

The xy-plane of the slot is shown in Fig. 4.2 below. To model the distributed excitation of the laser, the active region is divided into $N_{tot} = 2N+1, N \in \mathbb{I}$ segments along x. Each segment has a length Δ and is centered around a discretized x-coordinate $x_s = s \cdot \Delta$, $s \in \mathbb{I}$. Thus, $(2N+1) \cdot \Delta = l_x, N \in \mathbb{I}$ has to hold such that all discretization sections exactly fit within the active region. Similar to what was done in Section 3.1.1, Norton equivalent circuits are assigned to each discretization section as indicated in Fig. 4.2. The currents and impedances in each circuit can vary per section.

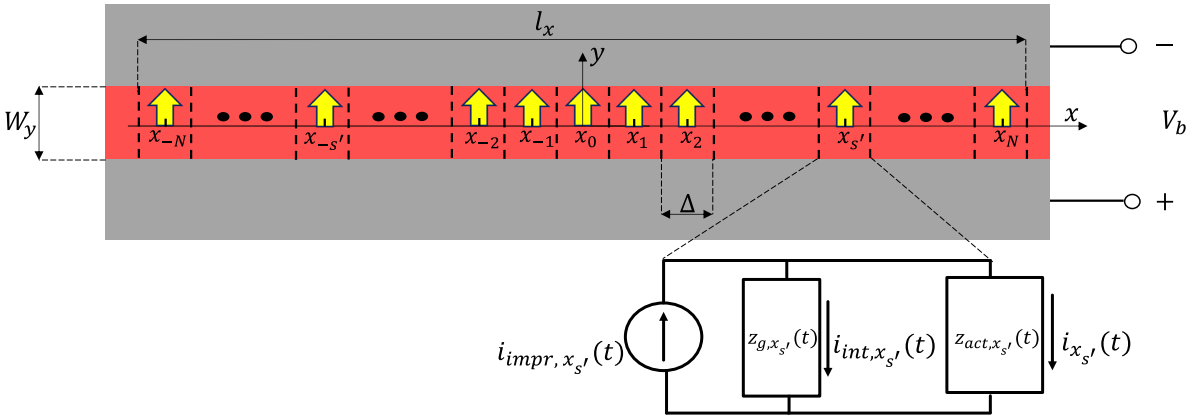

Figure 4.2: $xy-$plane of the infinite slot depicted in Fig. 4.1 with the corresponding discretized grid and the associated dimensions. Each discretization section has its own Norton equivalent circuit assigned to it.

Unlike the problem presented in Section 3.1.1, in this chapter the bias will be considered constant for all x. However, since the laser footprint l_x is long w.r.t the considered THz wavelengths, the amplitude of the laser can differ per discretization segment. Therefore, the peak rate at which charged carriers are generated becomes a function of space, $A(x_s)$. To establish a formulation for this parameter, one ought to consider Eq. 2.1c. This is obtained via spatial averaging over a volume where the dimensions are small in terms of the wavelength. In this chapter, such a description wouldn't be valid for the total volume where optical power is absorbed, $l_x W_y W_z$, since the laser footprint l_x can be long in terms of the considered THz wavelengths. However, for the volume related to a single discretization section, $\Delta W_y W_z$, which is electrically small, it would be valid given the amount of optical power absorbed in the volume, $\tilde{P}_{opt}(x_s)$.

Additionally, the moment at which the peak of the laser pulse arrives, t_{delay}, also varies over space due to the squinted incidence of the laser which is depicted in Fig. 4.1. Looking at Fig. 4.1 and 4.2, the laser coming in from the left arrives first at x_{-N}. Thus, for this location one can define $t_{delay}(x_{-N}) \equiv 0$. According to the geometries in Fig. 4.1 and 4.2, the difference in path length between two rays from neighbouring discretization sections is $cos(\theta_{opt}) \cdot \Delta$. Thus, the additional amount of path length each ray corresponding to a location x_s has to travel compared to the ray which is incident at x_{-N}, is equal to $(s+N) \cdot cos(\theta_{opt}) \cdot \Delta$, where $s = -N, -N+1, ..., N-1, N$. This additional amount of propagation occurs within the dielectric above the air gap with a velocity $\frac{c_0}{\sqrt{\varepsilon_{r,opt}}}$, where c_0 represents the speed of light in vacuum. Incorporating these parameters in Eq. 2.17 brings us to the following description for the impressed current at a location x_s:

$$i_{impr,x_s}(t_m) \equiv i_{impr}(x_s,t_m) \cong A(x_s)\cdot\delta t\frac{q_e^2}{m_{e,GaAs}}\frac{W_z\cdot\Delta}{W_y}V_b\cdot\tau_s\sum_{n=-\infty}^{m} e^{-4ln2\frac{\left(t_n-t_{delay}(x_s)\right)^2}{\tau_p^2}}\left[1-e^{-\frac{t_m-t_n}{\tau_s}}\right]e^{-\frac{t_m-t_n}{\tau_c}}, \tag{4.1a}$$

$$t_{delay}(x_s) = \frac{(s+N)\cdot cos\left(\theta_{opt}\right)\cdot\Delta}{c_0/\sqrt{\varepsilon_{r,opt}}} = \frac{(s+N)\cdot cos\left(\theta_{opt}\right)\cdot\Delta}{c_0}\sqrt{\varepsilon_{r,opt}}, \quad s=-N,-N+1,...,N-1,N, \tag{4.1b}$$

$$A(x_s) = \frac{\tilde{P}_{opt}(x_s)}{hf_c}\frac{T_L}{\tau_p}\sqrt{\frac{4ln2}{\pi}}\frac{1}{Vol'},\ Vol' = \Delta\cdot W_y\cdot W_z. \tag{4.1c}$$

There are multiple ways to divide the laser power over the active region which is embedded in the term $\tilde{P}_{opt}(x_s)$. An example of such a division will be given in Section 4.2. Also in this chapter, it is important to note that Eq. 2.5 still holds. However, the Fourier transform related to the current, $I_e(k_x,\omega)$, shall be a bit different as will be detailed in Section 4.1.2.

4.1.2 Voltages and Currents in the Source Region

Utilizing the same reasoning that was provided in previous chapters, the voltage at a location x_s is defined as the spatial average over the discretization length, Δ. Applying this to Eq. 2.5 gives

$$V(x_s,\omega) \equiv \left\{\frac{1}{\Delta}\int_{x_s-\Delta/2}^{x_s+\Delta/2} V(x,\omega)dx\right\} = \frac{1}{2\pi}\int_{-\infty}^{\infty}\frac{I_e(k_x,\omega)}{D(k_x,\omega)}sinc\left(\frac{k_x\Delta}{2}\right)e^{-jk_x\cdot x_s}dk_x. \tag{4.2}$$

Also here, spatial variations of the laser over a length Δ are considered to be small enough such that within a discretization section the induced current is considered to be constant over space but it does vary over time. Therefore, the (physical) current at a source location $x_{s'}$, indicated with yellow arrows in Fig. 4.2, is written as $i(x_{s'},t)rect\left(\frac{x-x_{s'}}{\Delta}\right)$. The quantities $i_{x_{s'}}(t) \equiv i(x_{s'},t)$ can also be viewed as the active antenna load currents from the Norton equivalent circuit in Fig. 4.2. The Fourier transform related to the total current, $I_e(k_x,\omega)$ in Eq. 2.5, then becomes equal to

$$I_e(k_x,\omega) = \frac{1}{\Delta}\mathscr{F}\left\{\mathscr{F}_{spatial}\left\{\sum_{s'=-N}^{N} i(x_{s'},t)rect\left(\frac{x-x_{s'}}{\Delta}\right)\right\}\right\} = sinc\left(\frac{k_x\Delta}{2}\right)\sum_{s'=-N}^{N} I_{s'}(\omega)e^{jk_xx_{s'}}, \tag{4.3}$$

where $I_{s'}(\omega) \equiv I(x_{s'},\omega)$ and $I(x_{s'},\omega) \overset{\mathscr{F}}{\Longleftrightarrow} i(x_{s'},t)$. Combining Eq. 4.2 and 4.3 one arrives to

$$V(x_s,\omega) = \sum_{s'=-N}^{N} I_{s'}(\omega)\cdot\frac{1}{2\pi}\int_{-\infty}^{\infty}\frac{sinc^2\left(\frac{k_x\Delta}{2}\right)}{D(k_x,\omega)}e^{-jk_x\cdot(x_s-x_{s'})}dk_x = \sum_{s'=-N}^{N} I(x_{s'},\omega)Z(x_s-x_{s'},\omega) \equiv \sum_{s'=-N}^{N} I_{s'}(\omega)Z_{ss'}(\omega),$$
$$Z_{ss'}(\omega) \equiv Z(x_s-x_{s'},\omega) = \frac{1}{2\pi}\int_{-\infty}^{\infty}\frac{sinc^2\left(\frac{k_x\Delta}{2}\right)}{D(k_x,\omega)}e^{-jk_x\cdot(x_s-x_{s'})}dk_x. \tag{4.4}$$

For similar reasons that were elaborated upon in Section 3.1.2, both sides of Eq. 4.4 shall be divided by the weighting function $Z^2(0,\omega) = (Z(0,\omega))^2$. This brings us to

$$\frac{V(x_s,\omega)}{Z^2(0,\omega)} = \sum_{s'=-N}^{N} I_{s'}(\omega)\frac{Z_{ss'}(\omega)}{Z^2(0,\omega)}. \tag{4.5}$$

The Norton circuit in Fig. 4.2 indicates that $i_{x_{s'}}(t) = i_{impr,x_{s'}}(t) - i_{int,x_{s'}}(t)$. In the frequency domain this implies $I_{s'}(\omega) = I_{impr,s'}(\omega) - I_{int,s'}(\omega)$. It produces

$$\frac{V(x_s,\omega)}{Z^2(0,\omega)} = \sum_{s'=-N}^{N} I_{impr,s'}(\omega)\frac{Z_{ss'}(\omega)}{Z^2(0,\omega)} - \sum_{s'=-N}^{N} I_{int,s'}(\omega)\frac{Z_{ss'}(\omega)}{Z^2(0,\omega)}. \tag{4.6}$$

In the following, the short-hand notations $i_{s'}(t) \equiv i_{x_{s'}}(t)$, $i_{impr,s'}(t) \equiv i_{impr,x_{s'}}(t)$ and $i_{int,s'}(t) \equiv i_{int,x_{s'}}(t)$ shall be adopted for compactness. Performing an inverse Fourier transform on both sides of Eq. 4.6 to move towards the time-domain gives

$$v(x_s,t) * h_{weight}(t) = \sum_{s'=-N}^{N} i_{impr,s'}(t) * h_{mutual}^{ss'}(t) - \sum_{s'=-N}^{N} i_{int,s'}(t) * h_{mutual}^{ss'}(t), \tag{4.7}$$

where $h_{weight}(t) \overset{\mathscr{F}}{\Longleftrightarrow} \frac{1}{Z^2(0,\omega)}$ and $h_{mutual}^{ss'}(t) \equiv h_{mutual}(x_s - x_{s'},t) \overset{\mathscr{F}}{\Longleftrightarrow} \frac{Z(x_s-x_{s'},\omega)}{Z^2(0,\omega)}$. Similar to what was done in previous chapters, Eq. 4.7 shall be evaluated at an observation time $t = t_m$ and the time-signals are discretized so the convolution becomes a summation. One arrives to

$$\delta t \sum_{n=-\infty}^{m} v(x_s,t_n) h_{weight}(t_m - t_n) = \delta t \sum_{s'=-N}^{N} \left(\sum_{n=-\infty}^{m} i_{impr,s'}(t_n) h_{mutual}^{ss'}(t_m - t_n) \right) - \delta t \sum_{s'=-N}^{N} \left(\sum_{n=-\infty}^{m} i_{int,s'}(t_n) h_{mutual}^{ss'}(t_m - t_n) \right). \tag{4.8}$$

Dividing out δt and separating the last terms ($n = m$) of the summations involving $v(x_s,t_n)$ and $i_{int,s'}(t_n)$ leads to

$$\begin{aligned} &\sum_{n=-\infty}^{m-1} v(x_s,t_n) h_{weight}(t_m - t_n) + v(x_s,t_m) h_{weight}(0) = \\ &\sum_{s'=-N}^{N} \left(\sum_{n=-\infty}^{m} i_{impr,s'}(t_n) h_{mutual}^{ss'}(t_m - t_n) \right) - \sum_{s'=-N}^{N} \left(\sum_{n=-\infty}^{m-1} i_{int,s'}(t_n) h_{mutual}^{ss'}(t_m - t_n) + i_{int,s'}(t_m) h_{mutual}^{ss'}(0) \right). \end{aligned} \tag{4.9}$$

The update rule given in Eq. 2.19 is also applicable here, after some slight adjustments. In Appendix C, one ought to replace $i_{int}(t)$, $v(t)$, A and $e^{-4ln2\frac{t''^2}{\tau_p^2}}$ with $i_{int}(x_s,t)$, $v(x_s,t)$, $A(x_s)$ and $e^{-4ln2\frac{(t''-t_{delay}(x_s))^2}{\tau_p^2}}$ respectively, in Eq. C.1. Afterwards one can perform exactly the same steps that are described in remaining parts of Appendix C to arrive to

$$i_{int}(x_s,t_m) = e^{-\frac{\delta t}{\tau_c}} e^{-\frac{\delta t}{\tau_s}} \cdot i_{int}(x_s,t_{m-1}) + v(x_s,t_m) \cdot g(x_s,t_m) \tag{4.10a}$$

$$g(x_s,t_m) = A(x_s) \cdot (\delta t)^2 \frac{q_e^2}{m_{e,GaAs}} \frac{W_z \cdot \Delta}{W_y} \sum_{n=-\infty}^{m} e^{-4ln2\frac{\left(t_n - t_{delay}(x_s)\right)^2}{\tau_p^2}} e^{-\frac{t_m - t_n}{\tau_c}}. \tag{4.10b}$$

Inserting Eq. 4.10 into Eq. 4.9 gives the following

$$\begin{aligned} &\sum_{n=-\infty}^{m-1} v(x_s,t_n) h_{weight}(t_m - t_n) + v(x_s,t_m) h_{weight}(0) = \sum_{s'=-N}^{N} \left(\sum_{n=-\infty}^{m} i_{impr,s'}(t_n) h_{mutual}^{ss'}(t_m - t_n) \right) \\ &- \sum_{s'=-N}^{N} \left(\sum_{n=-\infty}^{m-1} i_{int,s'}(t_n) h_{mutual}^{ss'}(t_m - t_n) + e^{-\frac{\delta t}{\tau_c}} e^{-\frac{\delta t}{\tau_s}} \cdot i_{int,s'}(t_{m-1}) \cdot h_{mutual}^{ss'}(0) + v(x_{s'},t_m) \cdot g(x_{s'},t_m) \cdot h_{mutual}^{ss'}(0) \right) \end{aligned} \tag{4.11}$$

Bringing all terms containing voltages at the observation time t_m to the left-hand side and the remaining terms to the right-hand side produces

$$\begin{aligned} &v(x_s,t_m) h_{weight}(0) + \sum_{s'=-N}^{N} v(x_{s'},t_m) \cdot g(x_{s'},t_m) \cdot h_{mutual}^{ss'}(0) = \sum_{s'=-N}^{N} \left(\sum_{n=-\infty}^{m} i_{impr,s'}(t_n) h_{mutual}^{ss'}(t_m - t_n) \right) \\ &- \sum_{s'=-N}^{N} \left(\sum_{n=-\infty}^{m-1} i_{int,s'}(t_n) h_{mutual}^{ss'}(t_m - t_n) + e^{-\frac{\delta t}{\tau_c}} e^{-\frac{\delta t}{\tau_s}} \cdot i_{int,s'}(t_{m-1}) \cdot h_{mutual}^{ss'}(0) \right) - \sum_{n=-\infty}^{m-1} v(x_s,t_n) h_{weight}(t_m - t_n). \end{aligned} \tag{4.12}$$

Since x_s ranges from x_{-N} until x_N, Eq. 4.12 actually represents $N_{tot} = 2N+1$ equations to take all discretization segments into account. In these equations, $v(x_s, t_m)$ represents the unknown quantities to be solved for. The system of equation from Eq. 4.12 can be compactly expressed via matrices and vectors:

$$\Big[h_{weight}(0)\boldsymbol{I} + \boldsymbol{H}(t_m)\Big]\boldsymbol{v}(t_m) = \boldsymbol{C_{impr}}(t_m) - \boldsymbol{C_{int}}(t_{m-1}) - \boldsymbol{C_{weight}}(t_{m-1}), \tag{4.13}$$

in which $\boldsymbol{I}$ indicates the N_{tot} x N_{tot} identity matrix. The other matrices and vectors are defined in the following manner

$$\boldsymbol{v}(t_m) = \begin{bmatrix} v(x_{-N}, t_m) \\ v(x_{-N+1}, t_m) \\ \vdots \\ v(x_{N-1}, t_m) \\ v(x_N, t_m) \end{bmatrix}, \boldsymbol{C_{weight}}(t_{m-1}) = \begin{bmatrix} \sum_{n=-\infty}^{m-1} v(x_{-N}, t_n) h_{weight}(t_m - t_n) \\ \sum_{n=-\infty}^{m-1} v(x_{-N+1}, t_n) h_{weight}(t_m - t_n) \\ \vdots \\ \sum_{n=-\infty}^{m-1} v(x_{N-1}, t_n) h_{weight}(t_m - t_n) \\ \sum_{n=-\infty}^{m-1} v(x_N, t_n) h_{weight}(t_m - t_n) \end{bmatrix}, \boldsymbol{C_{impr}}(t_m) = \begin{bmatrix} \sum_{s'=-N}^{N} \left(i_{impr,s'} \star h_{mutual}^{(-N)s'}\right)(t_m) \\ \sum_{s'=-N}^{N} \left(i_{impr,s'} \star h_{mutual}^{(-N+1)s'}\right)(t_m) \\ \vdots \\ \sum_{s'=-N}^{N} \left(i_{impr,s'} \star h_{mutual}^{(N-1)s'}\right)(t_m) \\ \sum_{s'=-N}^{N} \left(i_{impr,s'} \star h_{mutual}^{(N)s'}\right)(t_m) \end{bmatrix}, \tag{4.14a}$$

$$\boldsymbol{C_{int}}(t_{m-1}) = \begin{bmatrix} \sum_{s'=-N}^{N} \left[\left(i_{int,s'} \star h_{mutual}^{(-N)s'}\right)(t_{m-1}) + e^{-\frac{\delta t}{\tau_c}} e^{-\frac{\delta t}{\tau_s}} \cdot i_{int,s'}(t_{m-1}) \cdot h_{mutual}^{(-N)s'}(0)\right] \\ \sum_{s'=-N}^{N} \left[\left(i_{int,s'} \star h_{mutual}^{(-N+1)s'}\right)(t_{m-1}) + e^{-\frac{\delta t}{\tau_c}} e^{-\frac{\delta t}{\tau_s}} \cdot i_{int,s'}(t_{m-1}) \cdot h_{mutual}^{(-N+1)s'}(0)\right] \\ \vdots \\ \sum_{s'=-N}^{N} \left[\left(i_{int,s'} \star h_{mutual}^{(N-1)s'}\right)(t_{m-1}) + e^{-\frac{\delta t}{\tau_c}} e^{-\frac{\delta t}{\tau_s}} \cdot i_{int,s'}(t_{m-1}) \cdot h_{mutual}^{(N-1)s'}(0)\right] \\ \sum_{s'=-N}^{N} \left[\left(i_{int,s'} \star h_{mutual}^{(N)s'}\right)(t_{m-1}) + e^{-\frac{\delta t}{\tau_c}} e^{-\frac{\delta t}{\tau_s}} \cdot i_{int,s'}(t_{m-1}) \cdot h_{mutual}^{(N)s'}(0)\right] \end{bmatrix}, \tag{4.14b}$$

$$\boldsymbol{H}(t_m) = \begin{bmatrix} g(x_{-N}, t_m) h_{self}(0) & g(x_{-N+1}, t_m) h_{mutual}^{(-N)(-N+1)}(0) & \dots & g(x_{N-1}, t_m) h_{mutual}^{(-N)(N-1)}(0) & g(x_N, t_m) h_{mutual}^{(-N)(N)}(0) \\ g(x_{-N}, t_m) h_{mutual}^{(-N+1)(-N)}(0) & g(x_{-N+1}, t_m) h_{self}(0) & \dots & g(x_{N-1}, t_m) h_{mutual}^{(-N+1)(N-1)}(0) & g(x_N, t_m) h_{mutual}^{(-N+1)(N)}(0) \\ \vdots & \vdots & \ddots & \vdots & \vdots \\ g(x_{-N}, t_m) h_{mutual}^{(N-1)(-N)}(0) & g(x_{-N+1}, t_m) h_{mutual}^{(N-1)(-N+1)}(0) & \dots & g(x_{N-1}, t_m) h_{self}(0) & g(x_N, t_m) h_{mutual}^{(N-1)(N)}(0) \\ g(x_{-N}, t_m) h_{mutual}^{(N)(-N)}(0) & g(x_{-N+1}, t_m) h_{mutual}^{(N)(-N+1)}(0) & \dots & g(x_{N-1}, t_m) h_{mutual}^{(N)(N-1)}(0) & g(x_N, t_m) h_{self}(0) \end{bmatrix}. \tag{4.14c}$$

In Eq. 4.14, $h_{self}(t) \overset{\mathscr{F}}{\Longleftrightarrow} \frac{1}{Z(0,\omega)}$ appears because $h_{mutual}(x_s - x_{s'}, t)$ reduces to $h_{self}(t)$ when $x_s = x_{s'}$. Furthermore, the short-hand notation $(a \star b)(t_m) \equiv \sum_{n=-\infty}^{m} a(t_n) b(t_m - t_n)$ and $(a \star b)(t_{m-1}) \equiv \sum_{n=-\infty}^{m-1} a(t_n) b(t_m - t_n)$ has been adopted for brevity of the expressions in the vector elements of $\boldsymbol{C_{impr}}(t_m)$ and $\boldsymbol{C_{int}}(t_{m-1})$. The system of equations presented in Eq. 4.13 can be solved for $\boldsymbol{v}(t_m)$ by inverting the N_{tot} x N_{tot} matrix $h_{weight}(0)\boldsymbol{I} + \boldsymbol{H}(t_m)$:

$$\boldsymbol{v}(t_m) = \Big(h_{weight}(0)\boldsymbol{I} + \boldsymbol{H}(t_m)\Big)^{-1} \Big[\boldsymbol{C_{impr}}(t_m) - \boldsymbol{C_{int}}(t_{m-1}) - \boldsymbol{C_{weight}}(t_{m-1})\Big]. \tag{4.15}$$

Before the laser reaches the slot, the time-varying voltages and the internal currents in the active region ($v(x_s, t)$ and $i_{int}(x_s, t)$) are considered to be zero. Thus, if a time instance $t_m = t_{start}$ is early enough such that the laser hasn't arrived yet, $\boldsymbol{v}(t_{start})$ can be found via Eq. 4.15 by putting $\boldsymbol{C_{weight}}(t_{m-1})$ and $\boldsymbol{C_{int}}(t_{m-1})$ equal to zero. This can be done since those vectors only contain voltage terms and internal current terms related to times before $t_m = t_{start}$. Subsequently, one should apply the update rule given in Eq. 4.10 for the internal currents in the active region to obtain $i_{int}(x_s, t_{start})$. Then, $\boldsymbol{v}(t_{start})$ and $i_{int}(x_s, t_{start})$ can be combined with Eq.

4.15 to find $\boldsymbol{v}(t_{start+1})$ which can be used to acquire $i_{int}(x_s, t_{start+1})$. One can then utilize these quantities to obtain $\boldsymbol{v}(t_{start+2})$... and so on. Continuing this marching-on-in-time procedure one can fully obtain $v(x_s, t)$ and $i_{int}(x_s, t)$. Afterwards, the load currents can be found since $i(x_s, t) = i_{impr}(x_s, t) - i_{int}(x_s, t)$ (impressed currents are known beforehand via Eq. 4.1).

4.1.3 Voltage

Now that one has solved for the currents in Section 4.1.2, the voltage on the slot for all observation points, $v(x, t)$, can be determined.

The voltage shall be evaluated at discrete points along the slot: $x_k = k \cdot \delta x$, $k \in \mathbb{I}$. The voltage at a location x_k is defined as its spatial average over the discretization length δx. Thus, Eq. 2.22 still holds. However, the Fourier transform related to the current, $I_e(k_x, \omega)$, is different in this chapter and it is given by Eq. 4.3. Combining Eq. 2.22 and Eq. 4.3 produces

$$V(x_k, \omega) = \sum_{s'=-N}^{N} I_{s'}(\omega) \cdot \frac{1}{2\pi} \int_{-\infty}^{\infty} \frac{sinc\left(\frac{k_x \Delta}{2}\right) sinc\left(\frac{k_x \delta x}{2}\right)}{D(k_x, \omega)} e^{-jk_x \cdot (x_k - x_{s'})} dk_x = \sum_{s'=-N}^{N} I(x_{s'}, \omega) \tilde{Z}(x_k - x_{s'}, \omega) \equiv \sum_{s'=-N}^{N} I_{s'}(\omega) \tilde{Z}_{ks'}(\omega), \tag{4.16a}$$

$$\tilde{Z}(x_k - x_{s'}, \omega) \equiv \tilde{Z}_{ks'}(\omega) = \frac{1}{2\pi} \int_{-\infty}^{\infty} \frac{sinc\left(\frac{k_x \Delta}{2}\right) sinc\left(\frac{k_x \delta x}{2}\right)}{D(k_x, \omega)} e^{-jk_x \cdot (x_k - x_{s'})} dk_x. \tag{4.16b}$$

For similar reasons as in Section 4.1.2, both sides of Eq. 4.16 shall be divided by the weighting function $\tilde{Z}^2(0, \omega) = (\tilde{Z}(0, \omega))^2$. This gives

$$\frac{V(x_k, \omega)}{\tilde{Z}^2(0, \omega)} = \sum_{s'=-N}^{N} I_{s'}(\omega) \cdot \frac{\tilde{Z}(x_k - x_{s'}, \omega)}{\tilde{Z}^2(0, \omega)}. \tag{4.17}$$

Next, an inverse Fourier transform on both sides of Eq. 4.17 is performed to move towards the time-domain. It results in

$$v(x_k, t) * \tilde{h}_{weight}(t) = \sum_{s'=-N}^{N} i(x_{s'}, t) * \tilde{h}_{mutual}(x_k - x_{s'}, t) \tag{4.18}$$

where $\tilde{h}_{weight}(t) \overset{\mathscr{F}}{\Longleftrightarrow} \frac{1}{\tilde{Z}^2(0,\omega)}$ and $\tilde{h}_{mutual}(x_k - x_{s'}, t) \overset{\mathscr{F}}{\Longleftrightarrow} \frac{\tilde{Z}(x_k - x_{s'}, \omega)}{\tilde{Z}^2(0,\omega)}$. Also, $i(x_{s'}, t)$ represents the source currents that were obtained in Section 4.1.2. Evaluating Eq. 4.18 at an observation time $t = t_m$ and applying a time-discretization to the convolution of the signals brings us to

$$\delta t \sum_{n=-\infty}^{m} v(x_k, t_n) \tilde{h}_{weight}(t_m - t_n) = \delta t \sum_{s'=-N}^{N} \left(\sum_{n=-\infty}^{m} i(x_{s'}, t_n) \tilde{h}_{mutual}(x_k - x_{s'}, t_m - t_n) \right) \tag{4.19}$$

After dividing out δt and separating the last term of the summation involving $v(x_k, t_n)$ in Eq. 4.19 one arrives to

$$\sum_{n=-\infty}^{m-1} v(x_k, t_n) \tilde{h}_{weight}(t_m - t_n) + v(x_k, t_m) \tilde{h}_{weight}(0) = \sum_{s'=-N}^{N} \left(\sum_{n=-\infty}^{m} i(x_{s'}, t_n) \tilde{h}_{mutual}(x_k - x_{s'}, t_m - t_n) \right) \tag{4.20}$$

Finally, by rearranging terms and adopting the short-hand notations $(a \star b)(t_m) \equiv \sum_{n=-\infty}^{m} a(t_n) b(t_m - t_n)$ and $\tilde{h}^{ks'}_{mutual}(t) \equiv \tilde{h}_{mutual}(x_k - x_{s'}, t)$, an update rule for the voltage along the slot has been obtained:

$$v(x_k, t_m) = \frac{\sum_{s'=-N}^{N} \left(i_{s'} \star \tilde{h}^{ks'}_{mutual} \right)(t_m) - \sum_{n=-\infty}^{m-1} v(x_k, t_n) \tilde{h}_{weight}(t_m - t_n)}{\tilde{h}_{weight}(0)} \tag{4.21}$$

Before the laser arrives, the voltage in the active region, $v(x_s, t)$, is considered to be zero. Therefore, the time-varying voltage $v(x_k, t)$ at other locations along the slot is also zero before arrival of the laser since the voltage waves originate from the active region. Thus, if a time instance $t_m = t_{start}$ is early enough such that the

laser hasn't arrived yet, $v(x_k, t_{start})$ can be found via Eq. 4.21 by putting the summation involving $v(x_k, t_n)$ on the right-hand side equal to zero. Subsequently, $v(x_k, t_{start})$ ought to be plugged into Eq. 4.21 to obtain $v(x_k, t_{start+1})$, which can be used to find $v(x_k, t_{start+2})$... and so on. By implementing this marching-on-in-time procedure for every position x_k the voltage along the entire slot as a function of time is obtained.

4.2 Results of the Marching-On-Procedure

4.2.1 Simulation Settings & Assumptions

In the current Section, some example results of the marching-on procedures formulated in Sections 4.1.2 and 4.1.3 shall be presented. To obtain those results, the longitudinal Green's function related to two semi-infinite media given by Eq. 2.6 was used. This is a reasonable approximation for the stratification in Fig. 4.1 because of two reasons.

- The dielectric in which the laser propagates, with a relative permittivity of $\varepsilon_{r,opt}$, is above the air gap as shown in Fig. 4.1. The slot itself, is placed between the air gap and another dielectric with $\varepsilon_{r,rad}$. For a slot placed between air and a dense dielectric, most of the radiation occurs within the dielectric [11]. Since the dielectric for the laser is not in the same half-space as the dielectric in which the radiation occurs, the influence of its presence is limited.
- As can be deduced from Fig. 4.1, the laser rays in the air gap region all have an equal length of $\sqrt{d_{air}^2 + (\cot(\theta_{opt}) \cdot d_{air})^2} = d_{air} \cdot \sqrt{1 + \cot^2(\theta_{opt})}$. However, what's relevant for the formulation is the difference in path length because that determines the excitation delays as described in Section 4.1.1. The parameter d_{air} doesn't even appear in Sections 4.1.2 and 4.1.3. Therefore, one can increase the length of the air gap d_{air} such that the presence of the dielectric in which the laser propagates practically does not influence the resulting THz radiation other than the excitation delays on the slot given by Eq. 4.1.

If one still wishes to include the presence of the dielectric through which the laser propagates, then the longitudinal Green's function $D(k_x, \omega)$ can be evaluated numerically using a transmission line model [24].

Similar to earlier Chapters, for relatively large distances the mutual impedances in Eq. 4.4 and 4.16 are dominated by their residue contribution with associated propagation constants. The values given in Fig. 2.8 are not applicable here because in the current structure the dielectric where the radiation occurs has a relative permittivity of $\varepsilon_{r,rad} = 4$, instead of 11.7 which was used in previous chapters. The propagation constants found for the stratification in this chapter (again, not considering the dielectric with $\varepsilon_{r,opt}$) are shown in Fig. 4.3 below.

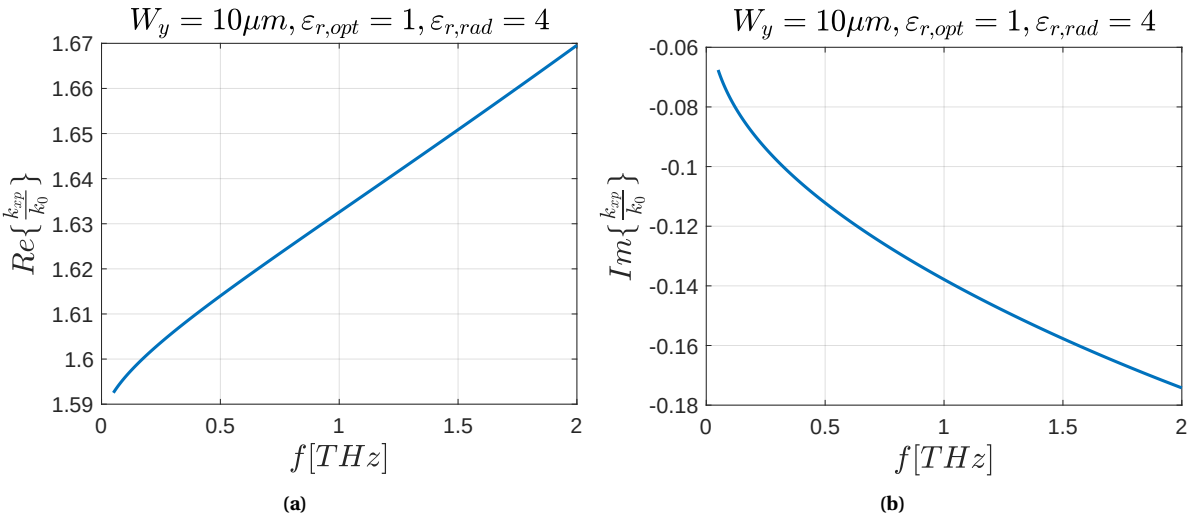

Figure 4.3: (a) Real and (b) imaginary part of the propagation constant k_{xp} versus frequency. In both graphs, $W_y = 10\mu m$, $\varepsilon_{r,opt} = 1$ and $\varepsilon_{r,rad} = 4$. The values are normalized to the free-space wavenumber k_0.

For the same reasons as mentioned earlier, the self-impedances and mutual impedances from Fig. 2.3 and 3.3 respectively are not applicable here. Impedances associated to the stratification considered in this chapter for several widths, distances and discretization lengths are given in Fig. 4.4 and 4.5 below.

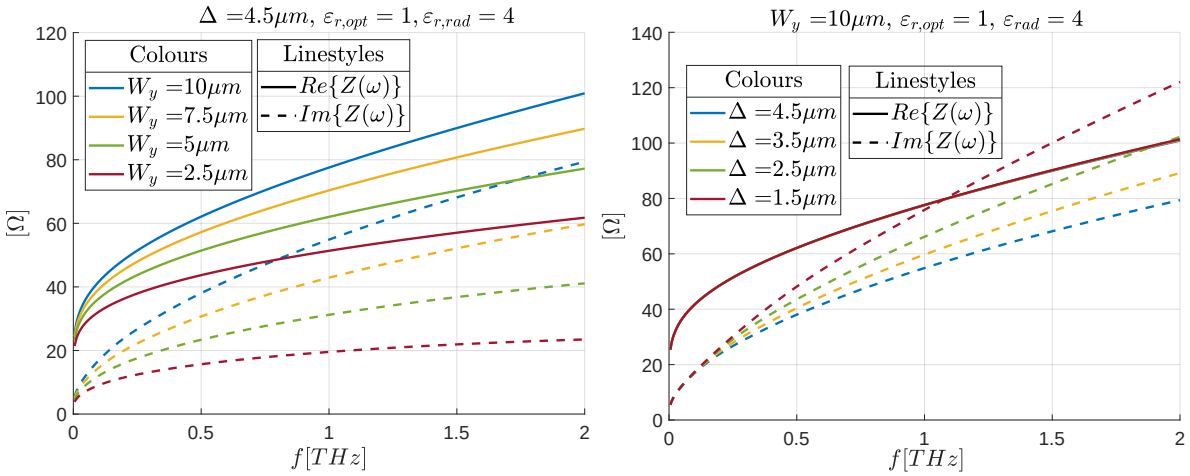

(a) **(b)**

Figure 4.4: (a) Input impedance of the slot antenna for several widths W_y and (b) different lengths of the photoconducting gap Δ.

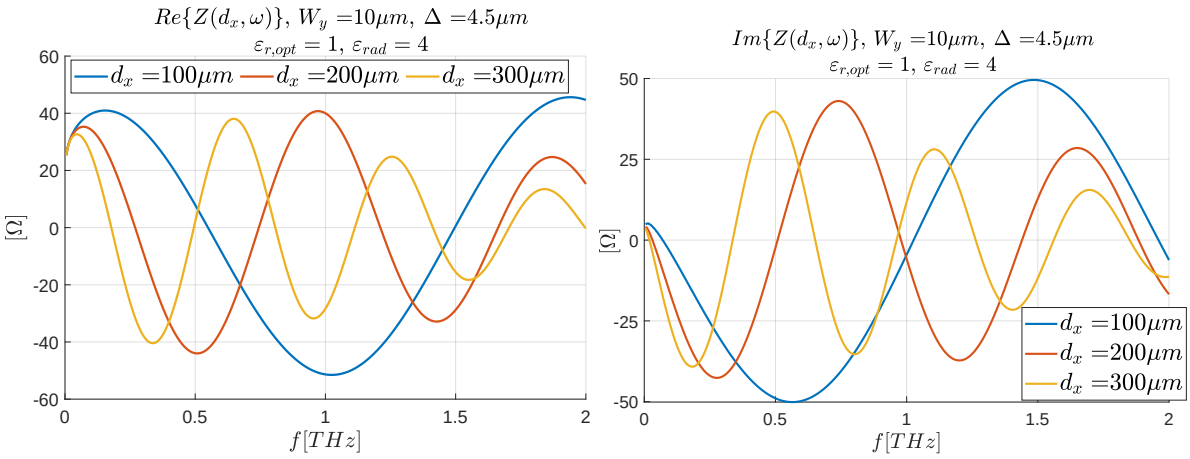

(a) **(b)**

Figure 4.5: (a) Real and (b) imaginary of the mutual impedance of an infinite slot for several distances d_x. The slot has a width $W_y = 10\,\mu m$ and the feeds have a length $\Delta = 4.5\,\mu m$.

Furthermore, in this Section the emphasis will be put on the verification of the proposed model and the influence of the laser angle of incidence. Therefore, there will be no tapered division of optical power over all the discretization sections. The total amount of average optical power absorbed will be equally divided among the structure. Thus, $\tilde{P}_{opt}(x_s) = \frac{\tilde{P}_{opt}}{N_{tot}}$, where $\tilde{P}_{opt}$ is the total amount of optical power absorbed by the active region.

4.2.2 Comparison with Non-Distributed Excitation

To verify the approach, in Fig. 4.6 a comparison is shown between the currents resulting from simulations with the single feed model presented in Chapter 2 and the formulation given in this chapter. This comparison is illustrated using two cases. One for a slot with a width $W_y = 2.5\mu m$ and one for a slot with $W_y = 7\mu m$. Since a squinted laser incidence was not taken into account in Chapter 2 the angle in the distributed model is set to $\theta_{opt} = 90°$. Furthermore, for both cases the bias is set to $V_b = 30V$, $\tilde{P}_{opt} = 9mW$ is absorbed and the slot is placed between air and a dielectric with a relative permittivity of 11.7. Since the model in Chapter 2 only holds for electrically small photoconducting volumes, l_x (which is equal to Δ in chapter 2) is set to $10\mu m$. In the distributed model, $N_{tot} = 9$ discretization sections have been used.

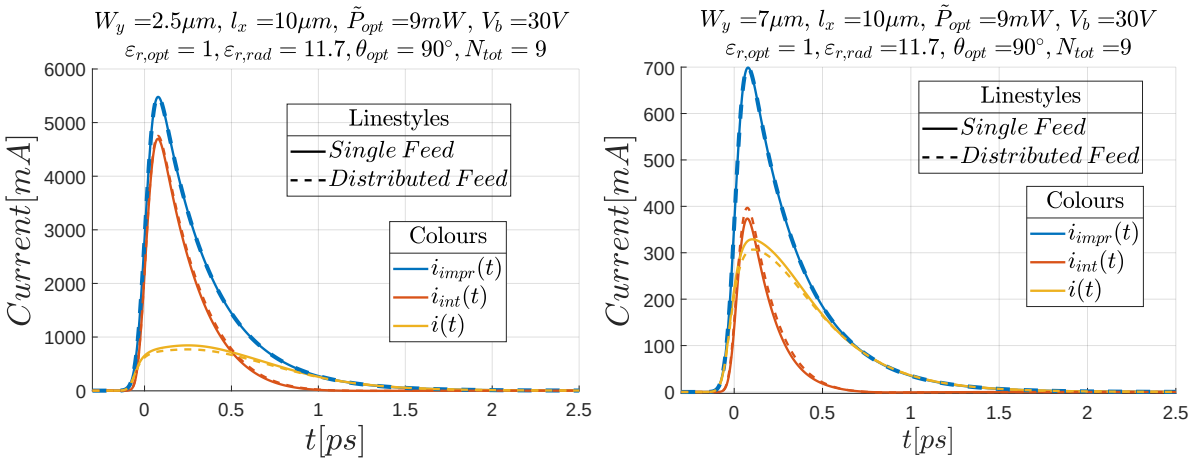

Figure 4.6: Comparison between simulation results for the single feed model and the formulation presented in this Chapter for a slot with (a) $W_y = 2.5\mu m$ and (b) $W_y = 7\mu m$. The currents related to the distributed model are the summation of the separate currents flowing through each discretization section.

The currents related to the distributed model in Fig. 4.6 are the summation of the individual currents running through each discretization section. Some of these individual currents are shown in Fig. 4.7. Since $\theta_{opt} = 90°$ and $\tilde{P}_{opt}(x_s)$ is constant the impressed current is the same for each discretization section according to Eq. 4.1 (that's why only $i_{impr}(x_{s=0}, t)$ is depicted). The internal current does vary over space, but still all the peaks occur at the same time since there's no time delay in the excitations when $\theta_{opt} = 90°$. Furthermore, due to symmetry in the array the internal current only depends on the absolute value of x_s. It is important to note that this symmetry would not have been there if each discretization section had a different moment of excitation ($\theta_{opt} < 90°$). Overall, one can see there is an excellent agreement between the two modelling approaches in Fig. 4.6. Still, there are some discrepancies around the peaks of the internal current and load current. Most likely this is related to the fact that the distributed model contains many more numerical steps (e.g. coupling between different discretization sections and matrix inversions) where these deviations might arise.

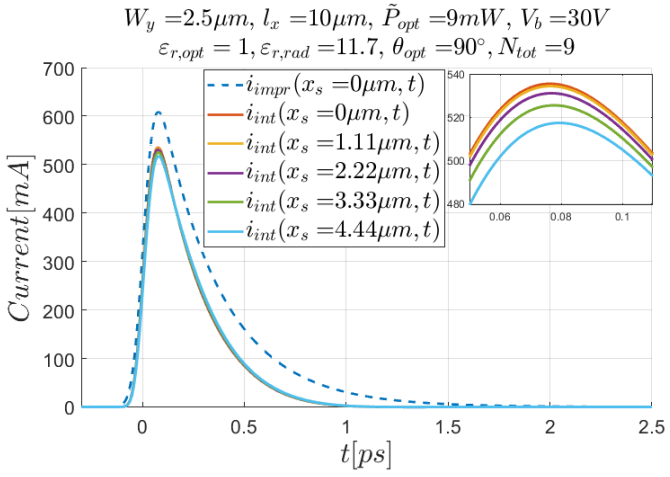

(a)

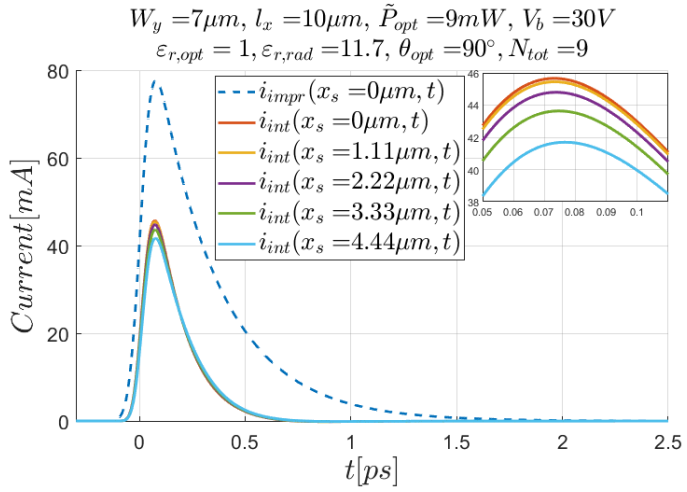

(b)

Figure 4.7: Impressed current and internal current at several positions on a slot with (a) $W_y = 2.5\mu m$ and (b) $W_y = 7\mu m$. Only the impressed current at $x_s = 0\mu m$ is shown since the impressed current is the same for all discretization sections in this case. The internal current is depicted for positive x only since the currents associated to negative x are the same due to symmetry in the array. The inset in the top right zooms in on the peaks of the internal current curves.

4.2.3 Optimum Laser Angle

In Fig. 4.8, 4.9 and 4.10 the voltage along the slot is shown for several time-instances. The dielectrics above the air gap and below the slot have a relative permittivity of $\varepsilon_{r,opt} = 12$ and $\varepsilon_{r,rad} = 4$, respectively. Furthermore, $\tilde{P}_{opt} = 75.159mW$ has been absorbed in the active region. The slot has a width $W_y = 10\mu m$ and it is biased with $V_b = 30V$. Contrary to the structures studied in Section 4.2.2, in this case the laser footprint has a length $l_x = 401\mu m$ which is not small w.r.t. the considered THz wavelengths. To model the active region, $N_{tot} = 401$ discretization sections have been used.

The difference between Fig. 4.8, 4.9 and 4.10 is the angle of incidence related to the laser, θ_{opt}. In all three graphs the voltage wave moving to the right is significantly bigger compared to the one to the left. However, in Fig. 4.8 with $\theta_{opt} = 60°$, the voltage wave to the right reaches the highest amplitude. This is the case because voltage waves moving to the right on the slot add up in a more coherent manner with newly excited voltage waves from the laser. To realize this, consider Eq. 4.1b. The delay between the excitations at x_s and x_{s+k}, where $k \in \mathbb{I}^+$, $s+k \leq N$ and $s \in \{-N, -N+1, ..., N-1\}$ with $N \in \mathbb{I}$, is equal to $t_{delay}(x_{s+k}) - t_{delay}(x_s) = k\frac{cos(\theta_{opt})\cdot\Delta}{c_0}\sqrt{\varepsilon_{r,opt}}$. In other words, the discretization section at x_{s+k} is excited $k\frac{cos(\theta_{opt})\cdot\Delta}{c_0}\sqrt{\varepsilon_{r,opt}}$ seconds

later by the laser compared to x_s. Furthermore, the voltage wave moving to the right which originates from x_s, travels a distance $k \cdot \Delta$ before arriving at x_{s+k}. According to the propagation constants from Fig. 4.3, this wave travels with a velocity $\frac{c_0}{\sqrt{\varepsilon_{r,eff}}}$, where $\sqrt{\varepsilon_{r,eff}} = \frac{Re\{k_{xp}\}}{k_0}$. Thus, it takes $\frac{k \cdot \Delta}{c_0/\sqrt{\varepsilon_{r,eff}}}$ seconds before the voltage wave originating from x_s arrives at x_{s+k}. In order for the waves moving to the right to add up coherently the excitation delay and voltage wave propagation delay between x_s and x_{s+k} need to match. Therefore, $k\frac{cos(\theta_{opt})\cdot\Delta}{c_0}\sqrt{\varepsilon_{r,opt}} = \frac{k\cdot\Delta}{c_0/\sqrt{\varepsilon_{r,eff}}}$ has to hold. Solving for θ_{opt} (where the solution is denoted with θ^*_{opt}) gives

$$\theta^*_{opt} = cos^{-1}\left(\frac{\sqrt{\varepsilon_{r,eff}}}{\sqrt{\varepsilon_{r,opt}}}\right) \tag{4.22}$$

When $\varepsilon_{r,opt} = 12$ and $1.59 < \sqrt{\varepsilon_{r,eff}} < 1.67$ according to Fig. 4.3a, then $61.2° < \theta^*_{opt} < 62.7°$. Out of the angles considered in Fig. 4.8, 4.9 and 4.10, the one in Fig. 4.8 is closest to the optimum which explains why it reaches the highest amplitude for the voltage wave propagating to the right. In Appendix E, the results for $\theta_{opt} = 40°$ and $\theta_{opt} = 80°$ (other than that same parameters as in Fig. 4.8) are depicted as well.

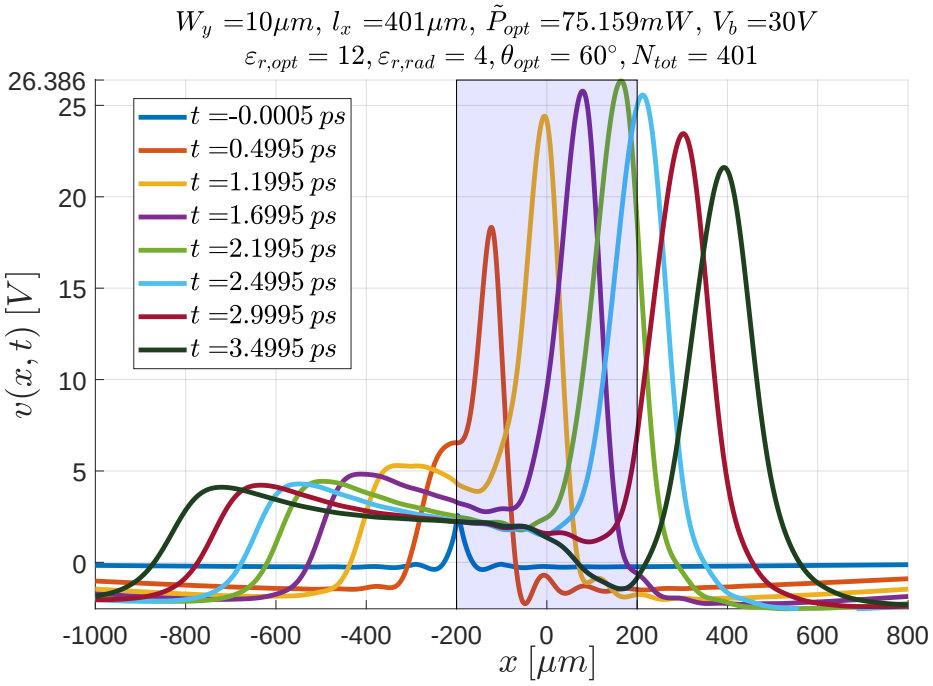

Figure 4.8: Voltage as a function of position for different time-instances. The laser has a footprint $l_x = 401\mu m$ and it is incident onto the active region (shaded in the figure) with an angle $\theta_{opt} = 60°$.

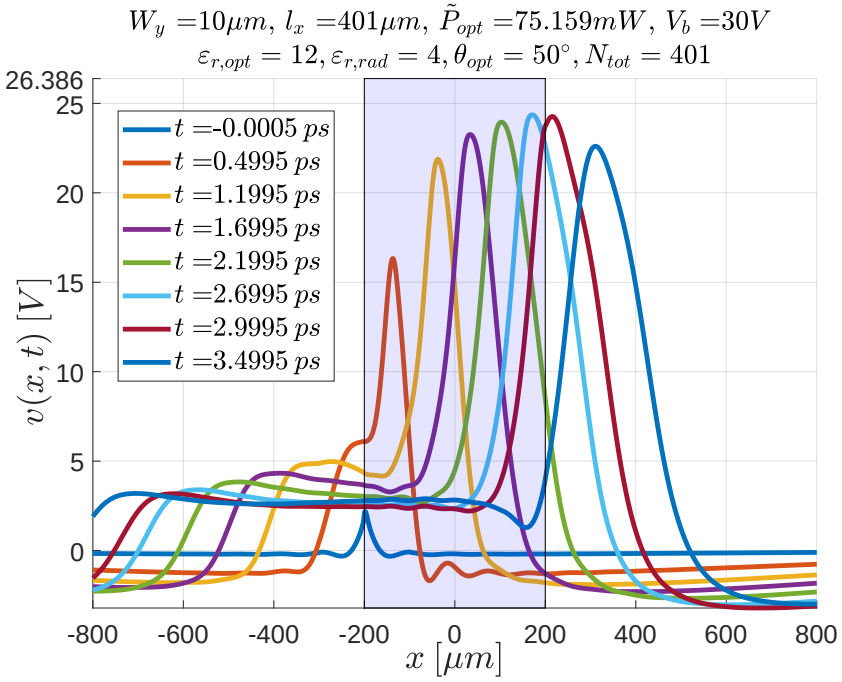

Figure 4.9: Voltage as a function of position for different time-instances. The laser has a footprint $l_x = 401\mu m$ and it is incident onto the active region (shaded in the figure) with an angle $\theta_{opt} = 50°$.

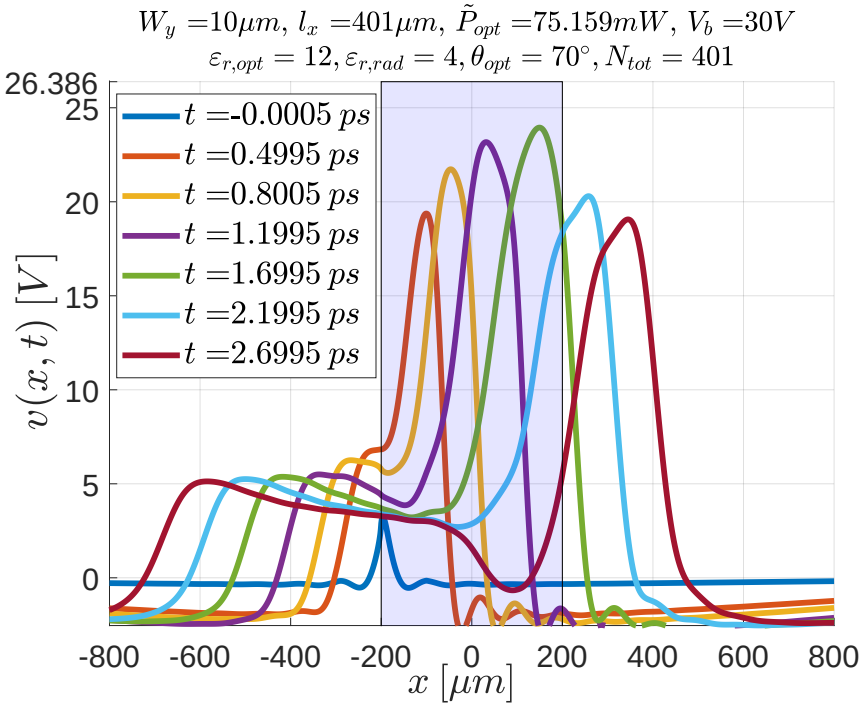

Figure 4.10: Voltage as a function of position for different time-instances. The laser has a footprint $l_x = 401\mu m$ and it is incident onto the active region (shaded in the figure) with an angle $\theta_{opt} = 70°$.

In Fig. 4.11 the voltages and current at several positions along the slot are depicted for the case in Fig. 4.8. The voltage curves further highlight the significant difference in shape and amplitude regarding the pulses moving to the left and to the right. The pulses moving to the right are much narrower and higher in amplitude. The time difference in the peaks of the currents in Fig. 4.11 are the result of the squinted incidence of the laser. One can see that locations at positive x are excited a bit later compared to negative x. Also, the phenomenon described in Section 3.3.3 becomes visible here. The excitation delay between discretization sections is set such that voltage waves moving to the right arrive at other sections when those are conductive. This leads to in increase in the internal current. This effect builds up since the voltage waves add up coherently in the active region as can be seen in Fig. 4.11. It leads to an important design rule. One should design these types of arrays such that the internal current doesn't go above the impressed current because this results in a reversal of the voltage as was shown in Section 3.3.3. In Fig. 4.11, the internal current does not go above the impressed current which allowed for the coherent addition of voltage waves illustrated in Fig. 4.8.

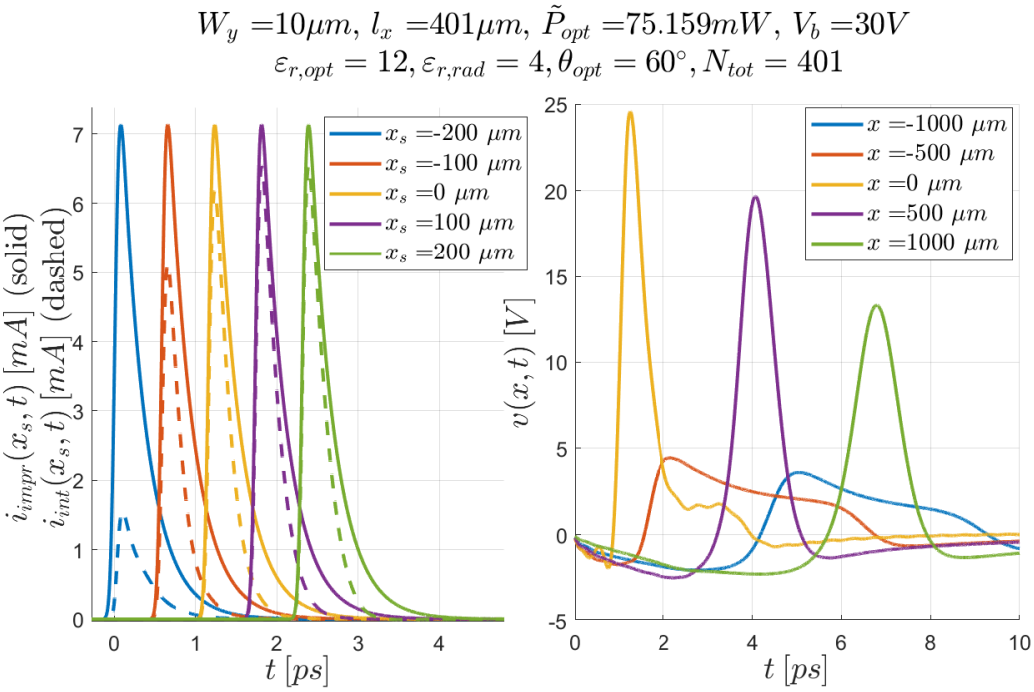

Figure 4.11: Impressed currents, internal currents and voltages versus time for several positions on the slot.

In Fig. 4.12 the dissipated power, $[V_b - v(x_s,t)] \cdot i(x_s,t)$, and power available for THz radiation, $v(x_s,t) \cdot i(x_s,t)$, [8] for several positions in the active region are shown. The figure indicates that to the left of the active region, which is excited first, there is a relatively high amount of power dissipation which rapidly decays for increasing x_s. Observing Fig. 4.8 and 4.11, one can see that as the wave moves to the right in the active region the physical current, $i(x_s,t) = i_{impr}(x_s,t) - i_{int}(x_s,t)$, decreases while the voltage across the slot width, $[V_b - v(x_s,t)]$, also decreases. This results in the rapid decay mentioned. Furthermore, from the same figures one can infer that when moving to the right $v(x_s,t)$ increases while $i(x_s,t)$ decreases. Thus, the power available varies much less compared the dissipated power as can be seen in Fig. 4.12.

To validate the procedure, the Fourier transforms of the acquired time-domain voltages and currents are plugged into Eq. 4.4. The result of this is depicted in Fig. 4.13 for several location x_s. Essentially the real and imaginary part of both sides of the equation are being compared. One can see that for all locations considered there's quite a good match indicating that the equation has been solved properly. The figure also highlights that the spectra of the voltage at positive x behave in a significantly different manner compared to the spectra at negative x. The spectra for positive x present wave-like behaviour, unlike the spectra at negative x.

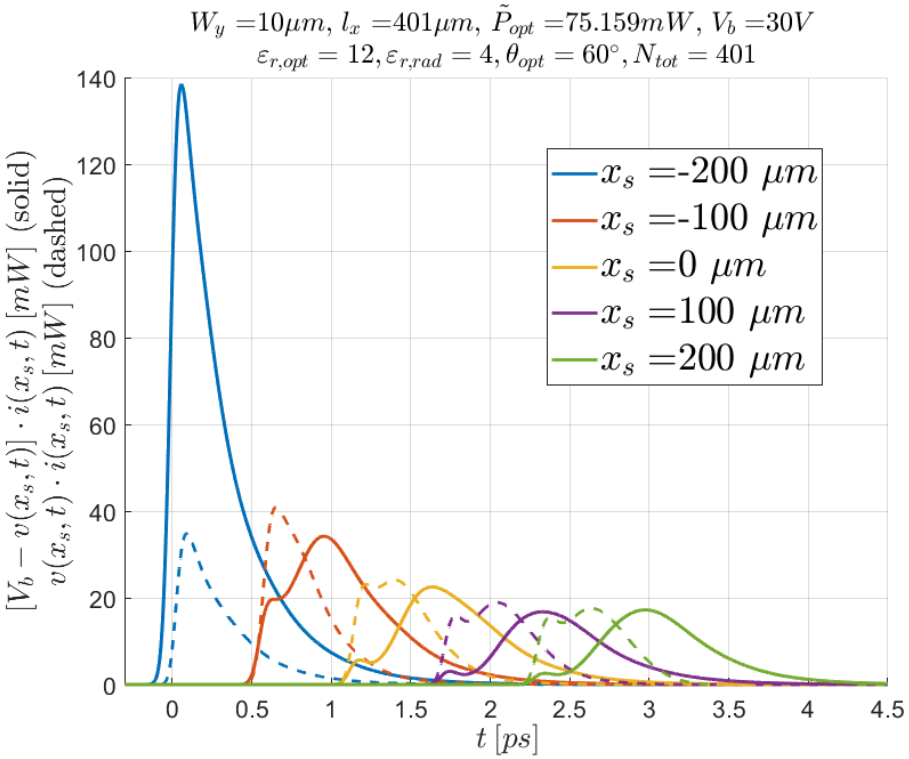

Figure 4.12: Dissipated power, $[V_b - v(x_s,t)] \cdot i(x_s,t)$, and power available for THz radiation, $v(x_s,t) \cdot i(x_s,t)$, for several positions x_s on the slot.

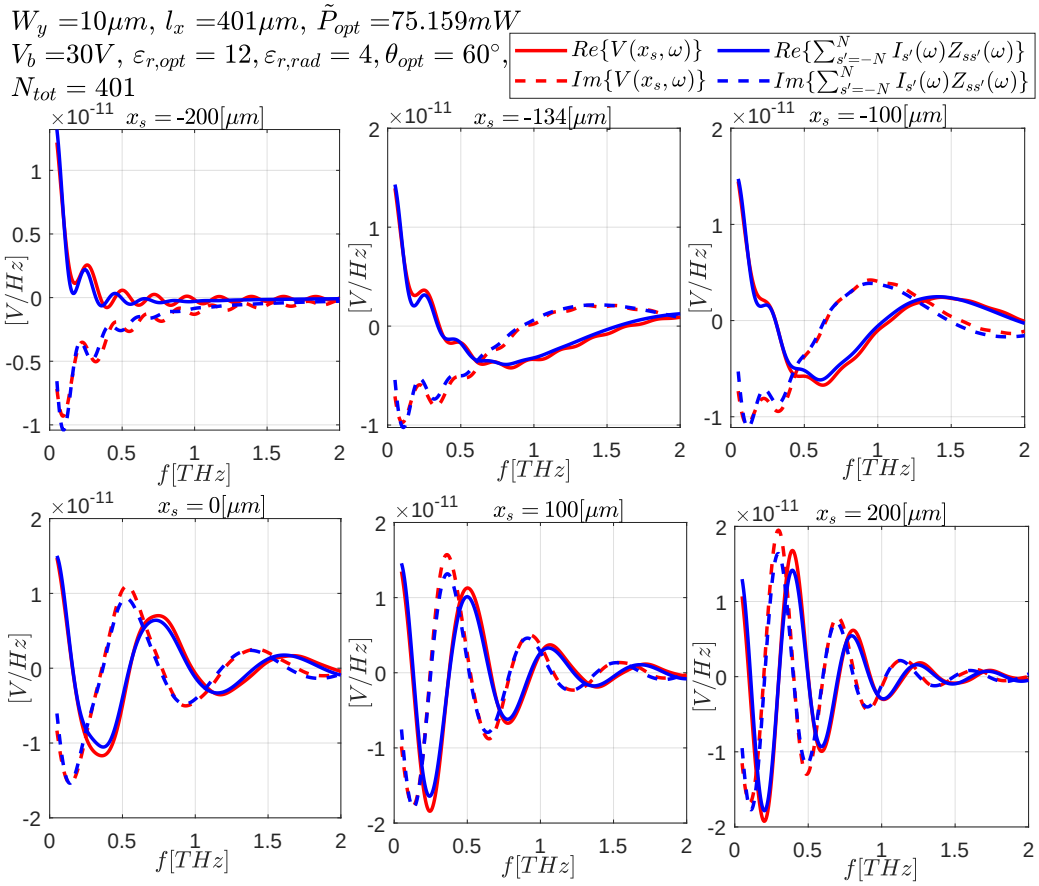

Figure 4.13: Validation of the marching-on procedure by comparing the real part and the imaginary part of both sides of Eq. 4.4 for several locations x_s.

4.2.4 Electric Vector Potential

In Section 4.2.3, it was established that the voltage wave moving towards positive x has a significantly larger amplitude compared to the wave moving towards negative x. A consequence of this is that the associated radiated fields show a similar behaviour: most of the radiation will be focused in a beam moving towards positive x. To illustrate this in a more explicit manner, the x-oriented [11] electric vector potential shall be studied in this chapter (the electric field can be readily found via the curl operation). After applying the small-width approximation, the electric vector potential in the dielectric with $\varepsilon_{r,rad}$ is given as follows [11]

$$F_{rad}(x,y,z,\omega) \cong -\int_{-\infty}^{\infty} \frac{e^{-jk_{rad}R(x-x',y,z)}}{4\pi R(x-x',y,z)} 2V(x',\omega)dx' \qquad (4.23)$$
$$R(x-x',y,z) = \sqrt{(x-x')^2+y^2+z^2}, \quad k_{rad} = k_0\sqrt{\varepsilon_{r,rad}}$$

Solving for the time-domain voltages over a large slot region to subsequently obtain $V(x',\omega)$ can be computationally expensive. Instead, one could determine the voltages and currents in the active region only and apply the right-hand side of Eq. 4.16a to find $V(x',\omega)$ at all other locations. The right-hand side of Eq. 4.16a only requires the Fourier transforms of the source currents, $I(x_{s'},\omega)$, and the mutual impedances, $\tilde{Z}_{ks'}(\omega)$. These types of mutual impedances are dominated by their residue contribution for large distances as mentioned in Section 2.2. Therefore, it is not necessary to evaluate the mutual impedance integrals numerically over a large region which allows for an efficient method to obtain $V(x',\omega)$. The result of this procedure for the case in Fig. 4.8 is given in Fig. 4.14 at several locations.

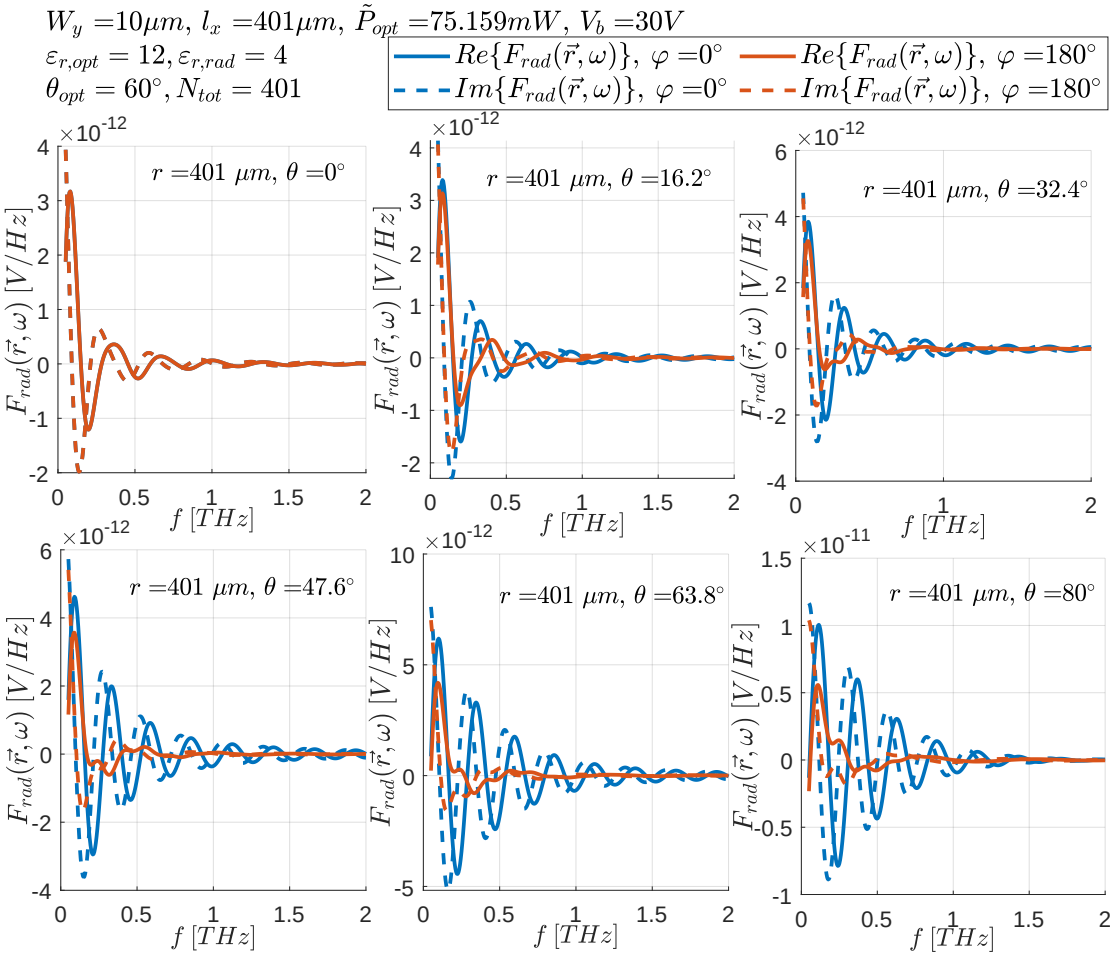

Figure 4.14: Real and imaginary part of the electric vector potential for several positions. Spherical coordinates are used such that $x = rsin(\theta)cos(\varphi)$, $y = rsin(\theta)sin(\varphi)$ and $z = -rcos(\theta)$.

One can see that when $\varphi = 0°$ (positive x) the vector potential has a larger amplitude compared to $\varphi = 180°$ (negative x). To make this even more explicit, the vector potential for different time instances in the xz-plane is shown in Fig. 4.15. This picture was obtained by taking the inverse Fourier transform of $F_{rad}(\vec{r},\omega)$ at several positions in the plane. Fig. 4.14 indicates that the spectra decrease over frequency and most of the spectral content is below 2 THz. Therefore, no weighting function was required when moving towards the time-domain. In Fig. 4.15, at each time instance the vector potential, $F_{rad}(\vec{r},t)$, is evaluated in dB relative to its maximum at that particular time within the area considered. This way, the difference in magnitude between the beam moving towards the left and the beam moving towards the right becomes visible. One can see that the waves start from the left because that's where the laser first arrives. Afterwards, a significant portion moves towards the right with more than 10 dB difference compared to the wave moving to the left.

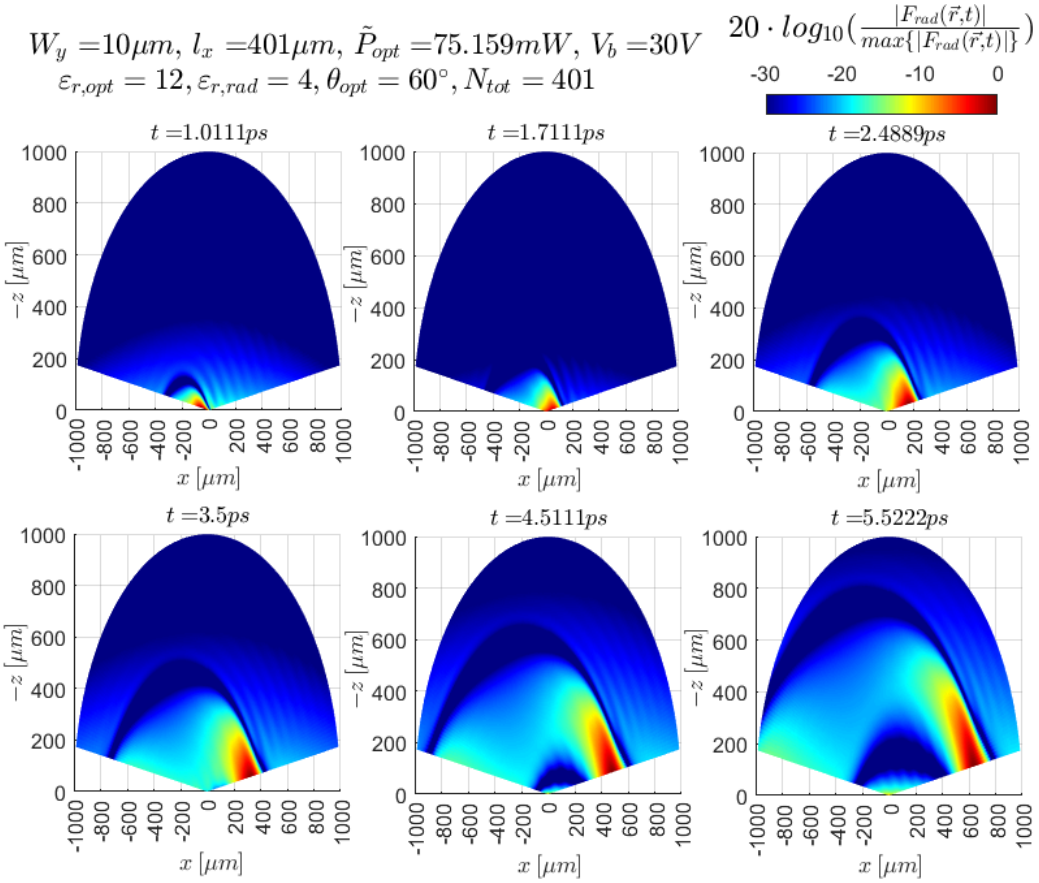

Figure 4.15: Electric vector potential at several time instances evaluated within a region in the xz-plane. For each time shot, the vector potential is evaluated in dB relative to the maximum at that particular time within the region considered.

Chapter 5

Conclusions and Future Work

5.1 Summary and Conclusions

In this work, the foundation has been laid for the modelling and design of photoconductive antennas with a distributed excitation. To arrive to that point, first the Norton equivalent circuit with associated constitutive relationships, introduced in [7] and [8], was applied to the case of an electrically small, photoconducting feed within an infinite slot in Chapter 2. Contrary to the works in [7] and [8], a frequency-dependent antenna input impedance is taken into account in the results from Chapter 2. Furthermore, it was shown that when not too close to the source, the propagation of the resulting voltage wave along the slot can be described as a voltage wave in a transmission line. The formulation was then extended to study the coupling of two photoconducting feeds in Chapter 3. An understanding of the interaction between the two feeds has been developed. Finally, in Chapter 3 the results converge to the single feed results from Chapter 2 when the distance between the feeds increases.

The insights from Chapter 2 and 3 turned out to be quite useful in Chapter 4. In Chapter 4, photoconducting material in an infinite slot is considered to be excited over a length, l_x, which can be long w.r.t. the considered THz wavelengths. However, when l_x is electrically small and one compares the obtained quantities with the curves from the single feed model, the results match. This behaviour is an important validation of the model. Furthermore, thanks to the knowledge acquired in Chapter 3, it was understood that when designing such a structure one has to make sure the internal current does not go above the impressed current in the active region to prevent a reversal of the voltage. In all Chapters mentioned, after obtaining the time-domain quantities, their corresponding Fourier transforms were plugged into the original imposed, frequency domain equation. This way, one could verify that not only the constitutive relations in the photoconducting material are satisfied but also the slot's Green's function.

The results in Chapter 4 show that by matching the velocity of the laser and the guided mode on the slot, it is possible to focus most of the energy in only one THz wave instead of equally dividing it over two. This will make it much simpler to design an efficient and non-dispersive antenna architecture. Besides effectively exciting a single THz wave instead of two, distributed feeding has more advantages. Dividing the laser power over a large region decreases the chances of the photoconducting material overheating. Thus, it allows for the usage of high-power lasers to excite the structure. A longer active region implies less optical power per section. This will lead to the undesired, regressive wave (i.e. the one moving to the left in Section 4.2.3) to be even smaller in amplitude since it does not make use of the coherent additions which result in the desired, progressive wave. Accordingly, the optimum laser angle will be better defined since the propagation associated with the residue (which was used to arrive to Eq. 4.22) becomes more dominant. Overall, one can conclude that distributed feeding is a suitable candidate to pole vault photoconductive antennas into the next generation of sensing applications. Thus, it is a concept worth exploring further.

5.2 Recommendations for Future Work

In order to move towards a practical implementation of the final structure discussed in Chapter 4, a few steps have to be taken. First of all, the model has to be extended to include the termination of a finite slot. Secondly, an array of finite slots ought to be considered to enable narrower antenna patterns, also in the plane orthogonal to the slots. This implies a study on the coupling between different slots as a function of the distance between them. Furthermore, since the radiation is based on the phenomena described in [11], a lens similar to the one in [25] should be designed to radiate the THz pulse into free space.

On the optical side, to excite the structure a lens has to be designed which is able to squeeze the laser in one dimension (the width of the slot) and spread it out along another (the slot axis). Furthermore, it would be worthwhile to study the influence of tapering the division of optical over the active region. Instead of equally dividing the power, it might be beneficial to taper the division such that the region which is excited first (e.g. at $x_s = -l_x/2$ in Chapter 4) receives less power compared to the region which is excited a bit later. This will further reduce the amplitude of the undesired, regressive wave.

Even though the stratification in Fig. 4.1 has some promising features, it's not the only option to consider. One might decide to implement a configuration as the one in Fig. 5.1 below. As an example, quartz has been used for the upper medium since it has a high transparency for optical frequencies [18]. The concepts developed in Chapter 4 still apply. However, the stratification is a bit different so the optimum angle changes depending on the relative permittivities used. The structure in Fig. 5.1 has a couple of advantages. Namely, there's no need to take an air gap into account and one doesn't need to consider losses due to reflections between a dielectric-air interface. Therefore, it's a viable option to consider in order to move towards physical implementations. Overall, there is ample space to continue the investigation on distributed feeding for photoconductive antennas.

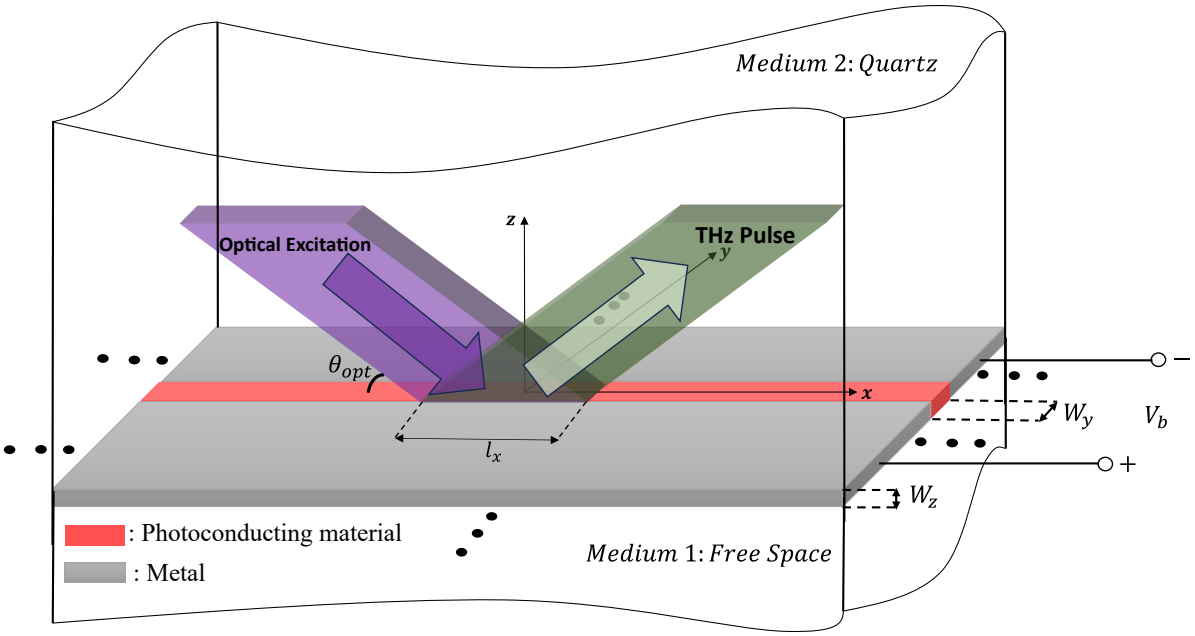

Figure 5.1: Infinite slot placed between two semi-infinite media. Air is situated below the slot while quartz is on top. In the upper medium, an optical, pulsed laser with a footprint l_x is incident from the left onto the photoconducting material. It excites a (dominant) THz pulse which propagates towards the right.

Bibliography

[1] Petrov, Vitaly and Kokkoniemi, Joonas and Moltchanov, Dmitri and Lehtomaki, Janne and Koucheryavy, Yevgeni and Juntti, Markku, "Last Meter Indoor Terahertz Wireless Access: Performance Insights and Implementation Roadmap," *IEEE Communications Magazine*, vol. 56, no. 6, 2018.

[2] P. U. Jepsen, D. G. Cooke and M. Koch, "Terahertz spectroscopy and imaging – Modern techniques and applications," *Laser Photonics Rev.*, 2011.

[3] P. F. Taday, "Applications of terahertz spectroscopy to pharmaceutical sciences," *Philosophical Transactions of the Royal Society of London. Series A: Mathematical, Physical and Engineering Sciences*, 2004.

[4] L. Yu, L. Hao, T. Meiqiong, H. Jiaoqi, L. Wei, D. Jinying, C. Xueping, F. Weiling and Z. Yang, "The medical application of terahertz technology in non-invasive detection of cells and tissues: opportunities and challenges," *RCS Advances*, 2019.

[5] L. Afsah-Hejri, P. Hajeb, P. Ara, and R. J. Ehsani, "Comprehensive Review on Food Applications of Terahertz Spectroscopy and Imaging," *Comprehensive Reviews in Food Science and Food Safety*, vol. 18, 2019.

[6] O. A. Castañeda-Uribe, C. A. Criollo, S. Winnerl, M. Helm, and A. Avila, "Comparative study of equivalent circuit models for photoconductive antennas," *Opt. Express*, 2018.

[7] A. Neto, N. Llombart and A. Freni, "Time Domain Modelling of Pulsed Photo Conducting Sources. Part I: The Norton Equivalent Circuit," *IEEE Transactions on Antennas and Propagation*, vol. 71, March 2023.

[8] A.F. Bernardis, P.M. Sberna, J. Bueno, H. Zhang, N. Llombart and A. Neto, "Time-Domain Modelling of Pulsed Photoconducting Sources—Part II: Characterization of an LT GaAs Bow-Tie Antenna," *IEEE Transactions on Antennas and Propagation*, vol. 71, March 2023.

[9] H. Zhang, N. Llombart, J. Bueno, A. Freni and A. Neto, "Time-Domain Equivalent Circuits for the Link Modelling Between Pulsed Photoconductive Sources and Receivers," *Unpublished*.

[10] A. Neto and S. Maci, "Green's Function for an Infinite Slot Printed Between Two Homogeneous Dielectrics - Part I: Magnetic Currents," *IEEE Transactions on Antennas and Propagation*, vol. 51, July 2003.

[11] S. Maci and A. Neto, "Green's Function of an Infinite Slot Printed Between Two Homogeneous Dielectrics - Part II: Asymptotic Solution," *IEEE Transactions on Antennas and Propagation*, vol. 52, March 2004.

[12] A. Neto, S. Bruni, G. Gerini and M. Sabbadini, "The Leaky Lens: A Broad-Band Fixed-Beam Leaky-Wave Antenna," *IEEE Transactions on Antennas and Propagation*, vol. 53, October 2005.

[13] S. Bruni, A. Neto and F. Marliani, "The Ultrawideband Leaky Lens Antenna," *IEEE Transactions on Antennas and Propagation*, vol. 55, October 2007.

[14] D. Pasqualini, A. Neto and R. A. Wyss, "Distributed Sources on Coplanar Waveguides: Application to Photomixers for THz Local Oscillators," *Microwave and Optical Technology Letters*, vol. 33, June 2002.

[15] J. T. Darrow, B. B. Hu, X.-C. Zhang, and D. H. Auston, "Subpicosecond electromagnetic pulses from large-aperture photoconducting antennas," *Optics Letters*, vol. 15, March 1990.

[16] B. B. Hu, J. T. Darrow, X.-C. Zhang, D. H. Auston and P. R. Smith, "Optically steerable photoconducting antennas," *Appl. Phys. Lett.*, March 1990.

[17] S. Preu, M. Mittendorff, H. Lu, H. B. Weber, S. Winnerl and A. C. Gossard, "1550 nm ErAs:In(Al)GaAs large area photoconductive emitters," *Appl. Phys. Lett.*, September 2012.

[18] D. R. Bacon, A. D. Burnett, M. Swithenbank, C. Russell, L. Li, C. D. Wood, J. Cunningham, E. H. Linfield, A. G. Davies, P. Dean and J. R. Freeman, "Free-space terahertz radiation from a LT-GaAs-on-quartz large-area photoconductive emitter," *Optics Express*, vol. 24, November 2016.

[19] L. B. Felsen and F. Capolino, "Time-Domain Green's Function for an Infinite Sequentially Excited Periodic Line Array of Dipoles," *IEEE Transactions on Antennas and Propagation*, vol. 48, June 2000.

[20] A. Neto and J. J. Lee, "Ultrawide-Band Properties of Long Slot Arrays," *IEEE Transactions on Antennas and Propagation*, vol. 54, February 2006.

[21] R.M. van Schelven, D. Cavallo and A. Neto, "Equivalent Circuit Models of Finite Slot Antennas," *IEEE Transactions on Antennas and Propagation*, vol. 67, July 2019.

[22] A. Neto, "Appendici," *Personal Communication*.

[23] A. Mehdipour, K. Mohammadpour-Aghdam and R. Faraji-Dana, "Complete Dispersion Analysis of Vivaldi Antenna for Ultra Wideband Applications," *Progress In Electromagnetics Research*, January 2007.

[24] S. van Berkel, A. Garufo, N. Llombart and A. Neto, "A Quasi-Analytical Tool for the Characterization of Transmission Lines at High Frequencies," *IEEE Antennas and Propagation Magazine*, vol. 58, June 2016.

[25] A. Neto, S. Bruni, G. Gerini and M. Sabbadini, "The Leaky Lens: A Broad-Band Fixed-Beam Antenna," *IEEE Transactions on Antennas and Propagation*, vol. 53, October 2005.

A

Evaluation of the Impressed Current

According to Eq. 2.1 and 2.2, the impressed current is given as follows

$$i_{impr}(t) = I_F^{iv}\{t, V_b, \tilde{P}_{opt}\} = A\frac{q_e^2}{m_{e,GaAs}}\frac{W_z\cdot\Delta}{W_y}\int_{-\infty}^{t} e^{-4ln2\frac{t''^2}{\tau_p^2}}\int_{t''}^{t} e^{-\frac{t-t'}{\tau_s}}V_b dt' e^{-\frac{t-t''}{\tau_c}}dt''. \tag{A.1}$$

The inner integral can be evaluated analytically

$$\int_{t''}^{t} e^{-\frac{t-t'}{\tau_s}}V_b dt' = V_b\cdot\tau_s\Big[e^{-\frac{t-t'}{\tau_s}}\Big]_{t'=t''}^{t'=t} = V_b\cdot\tau_s\Big[1-e^{-\frac{t-t''}{\tau_s}}\Big]. \tag{A.2}$$

Combining Eq. A.2 with A.1 and also imposing that the i_{impr} is evaluated at an observation time $t = t_m$ gives

$$i_{impr}(t_m) = A\frac{q_e^2}{m_{e,GaAs}}\frac{W_z\cdot\Delta}{W_y}V_b\cdot\tau_s\int_{-\infty}^{t_m} e^{-4ln2\frac{t''^2}{\tau_p^2}}\Big[1-e^{-\frac{t_m-t''}{\tau_s}}\Big]e^{-\frac{t_m-t''}{\tau_c}}dt''. \tag{A.3}$$

The discretization of Eq. 2.16 can also simply be applied to the function $f(t'') = 1$: $\sum_{n=-\infty}^{\infty} rect\Big(\frac{t''-t_n}{\delta t}\Big) = 1$. Inserting this summation in Eq. A.3 with $n = m$ for the summation upper bound gives

$$i_{impr}(t_m) = A\frac{q_e^2}{m_{e,GaAs}}\frac{W_z\cdot\Delta}{W_y}V_b\cdot\tau_s\int_{-\infty}^{t_m}\sum_{n=-\infty}^{m} rect\Big(\frac{t''-t_n}{\delta t}\Big)e^{-4ln2\frac{t''^2}{\tau_p^2}}\Big[1-e^{-\frac{t_m-t''}{\tau_s}}\Big]e^{-\frac{t_m-t''}{\tau_c}}dt''. \tag{A.4}$$

Putting the summation outside of the integral results in

$$i_{impr}(t_m) = A\frac{q_e^2}{m_{e,GaAs}}\frac{W_z\cdot\Delta}{W_y}V_b\cdot\tau_s\sum_{n=-\infty}^{m}\int_{-\infty}^{t_m} rect\Big(\frac{t''-t_n}{\delta t}\Big)e^{-4ln2\frac{t''^2}{\tau_p^2}}\Big[1-e^{-\frac{t_m-t''}{\tau_s}}\Big]e^{-\frac{t_m-t''}{\tau_c}}dt''. \tag{A.5}$$

Since $rect\Big(\frac{t''-t_n}{\delta t}\Big) = 1, |t''-t_n| < \frac{\delta t}{2}$, the integral in Eq. A.5 can be simplified accordingly

$$i_{impr}(t_m) = A\frac{q_e^2}{m_{e,GaAs}}\frac{W_z\cdot\Delta}{W_y}V_b\cdot\tau_s\sum_{n=-\infty}^{m}\int_{t_n-\frac{\delta t}{2}}^{t_n+\frac{\delta t}{2}} e^{-4ln2\frac{t''^2}{\tau_p^2}}\Big[1-e^{-\frac{t_m-t''}{\tau_s}}\Big]e^{-\frac{t_m-t''}{\tau_c}}dt''. \tag{A.6}$$

If the discretization interval, δt, is sufficiently small such that a function $f(t'')$ is approximately constant in the domain $t'' \in \Big[t_n-\frac{\delta t}{2}, t_n+\frac{\delta t}{2}\Big]$, then $\int_{t_n-\frac{\delta t}{2}}^{t_n+\frac{\delta t}{2}} f(t'')dt'' \cong \delta t\cdot f(t_n)$. Applying this to Eq. A.6 bring us to the final expression

$$i_{impr}(t_m) \cong A\cdot\delta t\frac{q_e^2}{m_{e,GaAs}}\frac{W_z\cdot\Delta}{W_y}V_b\cdot\tau_s\sum_{n=-\infty}^{m} e^{-4ln2\frac{t_n^2}{\tau_p^2}}\Big[1-e^{-\frac{t_m-t_n}{\tau_s}}\Big]e^{-\frac{t_m-t_n}{\tau_c}}. \tag{A.7}$$

B

Discrete Convolution

The continuous-time convolution of two signals, $f(t)$ and $h(t)$, is written as follows

$$f(t) * h(t) = \int_{-\infty}^{t} f(t')h(t-t')dt'. \tag{B.1}$$

The upper bound of in the integration is equal to t instead of ∞. This is the case because the convolution operations considered in this work are representative of causal input-output relations. This means that if $f(t)$ were to be the input and $h(t)$ the impulse response, then the output $f(t) * h(t)$ at a time t should not depend on input values $f(t')$ later than $t' = t$.

A time-discretization is applied to $f(t')$: $f(t') \cong \sum_{n=-\infty}^{\infty} f(t_n) rect\left(\frac{t'-t_n}{\delta t}\right)$. Furthermore, it is imposed that the convolution in Eq. B.1 is observed at a time $t = t_m$. This produces

$$f(t_m) * h(t_m) \cong \int_{-\infty}^{t_m} \sum_{n=-\infty}^{m} f(t_n) rect\left(\frac{t'-t_n}{\delta t}\right) h(t_m - t')dt'. \tag{B.2}$$

The upper bound $n = m$ is taken for the summation in correspondence with the upper bound of the integral. Putting the summation outside of the integral results in

$$f(t_m) * h(t_m) \cong \sum_{n=-\infty}^{m} \int_{-\infty}^{t_m} f(t_n) rect\left(\frac{t'-t_n}{\delta t}\right) h(t_m - t')dt'. \tag{B.3}$$

Since $rect\left(\frac{t'-t_n}{\delta t}\right) = 1, |t'-t_n| < \frac{\delta t}{2}$, the integral in Eq. B.3 can be simplified accordingly

$$f(t_m) * h(t_m) \cong \sum_{n=-\infty}^{m} \int_{t_n-\frac{\delta}{2}}^{t_n+\frac{\delta}{2}} f(t_n)h(t_m - t')dt'. \tag{B.4}$$

If the discretization interval, δt, is sufficiently small such that a function $y(t')$ is approximately constant in the domain $t' \in \left[t_n - \frac{\delta t}{2}, t_n + \frac{\delta t}{2}\right]$, then $\int_{t_n-\frac{\delta t}{2}}^{t_n+\frac{\delta t}{2}} y(t')dt' \cong \delta t \cdot y(t_n)$. Applying this to Eq. B.4 bring us to the final expression

$$f(t_m) * h(t_m) \cong \delta t \sum_{n=-\infty}^{m} f(t_n)h(t_m - t_n). \tag{B.5}$$

C

Internal Current Update Rule

According to Eq. 2.1 and 2.2, the internal current is given as follows

$$i_{int}(t) = I_F^{iv}\{t, v(t), \tilde{P}_{opt}\} = A\frac{q_e^2}{m_{e,GaAs}}\frac{W_z\cdot\Delta}{W_y}\int_{-\infty}^{t} e^{-4ln2\frac{t''^2}{\tau_p^2}}\int_{t''}^{t} e^{-\frac{t-t'}{\tau_s}}v(t')dt'e^{-\frac{t-t''}{\tau_c}}dt''. \tag{C.1}$$

This can be seen as an integration of "partial current" [8] contributions induced by the impinging laser

$$i_{int}(t) = \int_{-\infty}^{t} i_{partial}(t,t'')dt'' \tag{C.2a}$$

$$i_{partial}(t,t'') = A\frac{q_e^2}{m_{e,GaAs}}\frac{W_z\cdot\Delta}{W_y}e^{-4ln2\frac{t''^2}{\tau_p^2}}\int_{t''}^{t} e^{-\frac{t-t'}{\tau_s}}v(t')dt'e^{-\frac{t-t''}{\tau_c}}. \tag{C.2b}$$

One can then apply a time-discretization for $i_{partial}(t,t'')$ w.r.t. t'': $i_{partial}(t,t'') \cong \sum_{n=-\infty}^{\infty} i_{partial}(t,t_n)rect\Big(\frac{t''-t_n}{\delta t}\Big)$. This shall be combined with Eq. C.2a. Moreover, an observation time of $t = t_m$ is imposed and $n = m$ is taken as the upper bound for the summation (this corresponds with the integral upper bound). One arrives to

$$i_{int}(t_m) = \int_{-\infty}^{t_m}\sum_{n=-\infty}^{m} i_{partial}(t_m,t_n)rect\Big(\frac{t''-t_n}{\delta t}\Big)dt''. \tag{C.3}$$

Putting the summation outside of the integral and utilizing that $rect\Big(\frac{t''-t_n}{\delta t}\Big) = 1, |t''-t_n| < \frac{\delta t}{2}$ results in

$$i_{int}(t_m) = \sum_{n=-\infty}^{m}\int_{t_n-\frac{\delta t}{2}}^{t_n+\frac{\delta t}{2}} i_{partial}(t_m,t_n)dt''. \tag{C.4}$$

If the discretization interval, δt, is sufficiently small such that a function $f(t'')$ is approximately constant in the domain $t'' \in \Big[t_n-\frac{\delta t}{2}, t_n+\frac{\delta t}{2}\Big]$, then $\int_{t_n-\frac{\delta t}{2}}^{t_n+\frac{\delta t}{2}} f(t'')dt'' \cong \delta t\cdot f(t_n)$. Applying this to Eq. C.4 produces

$$i_{int}(t_m) = \delta t\sum_{n=-\infty}^{m} i_{partial}(t_m,t_n) \tag{C.5a}$$

$$i_{partial}(t_m,t_n) = A\frac{q_e^2}{m_{e,GaAs}}\frac{W_z\cdot\Delta}{W_y}e^{-4ln2\frac{t_n^2}{\tau_p^2}}\int_{t_n}^{t_m} e^{-\frac{t_m-t'}{\tau_s}}v(t')dt'e^{-\frac{t_m-t_n}{\tau_c}}. \tag{C.5b}$$

Using $v(t') \cong \sum_{q=-\infty}^{\infty} v(t_q)rect\Big(\frac{t'-t_q}{\delta t}\Big)$, the integral over t' in Eq. C.5 can be evaluated with the same type of steps as in Eq. C.3 until C.5

$$\begin{aligned}
\int_{t_n}^{t_m} e^{-\frac{t_m-t'}{\tau_s}}v(t')dt' &\cong \int_{t_n}^{t_m} e^{-\frac{t_m-t'}{\tau_s}}\sum_{q=n}^{m} v(t_q)rect\Big(\frac{t'-t_q}{\delta t}\Big)dt' \\
&= \sum_{q=n}^{m} v(t_q)\int_{t_n}^{t_m} e^{-\frac{t_m-t'}{\tau_s}}rect\Big(\frac{t'-t_q}{\delta t}\Big)dt' \\
&= \sum_{q=n}^{m} v(t_q)\int_{t_q-\frac{\delta t}{2}}^{t_q+\frac{\delta t}{2}} e^{-\frac{t_m-t'}{\tau_s}}dt' \\
&\cong \delta t\sum_{q=n}^{m} v(t_q)e^{-\frac{t_m-t_q}{\tau_s}}.
\end{aligned} \tag{C.6}$$

Together with Eq. C.5 this brings us to

$$\begin{aligned} i_{int}(t_m) &= A\cdot(\delta t)^2 \frac{q_e^2}{m_{e,GaAs}} \frac{W_z\cdot\Delta}{W_y} \sum_{n=-\infty}^{m} e^{-4ln2\frac{t_n^2}{\tau_p^2}} e^{-\frac{t_m-t_n}{\tau_c}} \sum_{q=n}^{m} v(t_q) e^{-\frac{t_m-t_q}{\tau_s}} \\ &= Y_0 \sum_{n=-\infty}^{m} e^{-4ln2\frac{t_n^2}{\tau_p^2}} e^{-\frac{t_m-t_n}{\tau_c}} \sum_{q=n}^{m} v(t_q) e^{-\frac{t_m-t_q}{\tau_s}} \\ &= Y_0 e^{\frac{-t_m}{\tau_c}} e^{\frac{-t_m}{\tau_s}} \sum_{n=-\infty}^{m} e^{-4ln2\frac{t_n^2}{\tau_p^2}} e^{\frac{t_n}{\tau_c}} \sum_{q=n}^{m} v(t_q) e^{\frac{t_q}{\tau_s}}, \end{aligned} \tag{C.7}$$

where $Y_0 \equiv A\cdot(\delta t)^2 \frac{q_e^2}{m_{e,GaAs}} \frac{W_z\cdot\Delta}{W_y} \left[\frac{A}{V}\right]$. Furthermore, the exponential terms $e^{\frac{-t_m}{\tau_c}}$ and $e^{\frac{-t_m}{\tau_s}}$ which do not depend on the indices n and q have been taken outside the summations. By additionally defining $\alpha_n = e^{-4ln2\frac{t_n^2}{\tau_p^2}} e^{\frac{t_n}{\tau_c}}$ and $\beta_q = v(t_q) e^{\frac{t_q}{\tau_s}}$ the double summation in Eq. C.7 can be written out as

$$\begin{aligned} \sum_{n=-\infty}^{m} \alpha_n \sum_{q=n}^{m} \beta_q &= \alpha_{-\infty}(\beta_{-\infty} + \beta_{-\infty+1} + \beta_{-\infty+2} + ... + \beta_m) \\ &\quad + \alpha_{-\infty+1}(\beta_{-\infty+1} + \beta_{-\infty+2} + ... + \beta_m) \\ &\quad + \alpha_{-\infty+2}(\beta_{-\infty+2} + ... + \beta_m) \\ &\quad + .. + \alpha_{m-1}(\beta_{m-1} + \beta_m) \\ &\quad + \alpha_m \beta_m \\ &= \sum_{n=-\infty}^{m-1} \alpha_n \sum_{q=n}^{m-1} \beta_q + \beta_m \sum_{n=-\infty}^{m} \alpha_n. \end{aligned} \tag{C.8}$$

Utilizing this decomposition, Eq. C.7 can be expressed in the following manner

$$\begin{aligned} i_{int}(t_m) &= Y_0 e^{\frac{-t_m}{\tau_c}} e^{\frac{-t_m}{\tau_s}} \sum_{n=-\infty}^{m} \alpha_n \sum_{q=n}^{m} \beta_q \\ &= Y_0 e^{\frac{-t_m}{\tau_c}} e^{\frac{-t_m}{\tau_s}} \sum_{n=-\infty}^{m-1} \alpha_n \sum_{q=n}^{m-1} \beta_q + Y_0 e^{\frac{-t_m}{\tau_c}} e^{\frac{-t_m}{\tau_s}} \beta_m \sum_{n=-\infty}^{m} \alpha_n \\ &= Y_0 e^{\frac{-t_m}{\tau_c}} e^{\frac{-t_m}{\tau_s}} \sum_{n=-\infty}^{m-1} e^{-4ln2\frac{t_n^2}{\tau_p^2}} e^{\frac{t_n}{\tau_c}} \sum_{q=n}^{m-1} v(t_q) e^{\frac{t_q}{\tau_s}} + Y_0 e^{\frac{-t_m}{\tau_c}} e^{\frac{-t_m}{\tau_s}} v(t_m) e^{\frac{t_m}{\tau_s}} \sum_{n=-\infty}^{m} e^{-4ln2\frac{t_n^2}{\tau_p^2}} e^{\frac{t_n}{\tau_c}} \\ &= Y_0 e^{\frac{-t_m}{\tau_c}} e^{\frac{-t_m}{\tau_s}} \sum_{n=-\infty}^{m-1} e^{-4ln2\frac{t_n^2}{\tau_p^2}} e^{\frac{t_n}{\tau_c}} \sum_{q=n}^{m-1} v(t_q) e^{\frac{t_q}{\tau_s}} + Y_0 v(t_m) \sum_{n=-\infty}^{m} e^{-4ln2\frac{t_n^2}{\tau_p^2}} e^{-\frac{t_m-t_n}{\tau_c}}. \end{aligned} \tag{C.9}$$

Since $t_m = m\cdot\delta t - \frac{\delta t}{2}$, it also holds that $t_m = t_{m-1} + \delta t$. Incorporating this in the term $e^{\frac{-t_m}{\tau_c}} e^{\frac{-t_m}{\tau_s}}$ in Eq. C.9 gives

$$i_{int}(t_m) = Y_0 e^{-\frac{\delta t}{\tau_c}} e^{-\frac{\delta t}{\tau_s}} e^{-\frac{t_{m-1}}{\tau_c}} e^{-\frac{t_{m-1}}{\tau_s}} \sum_{n=-\infty}^{m-1} e^{-4ln2\frac{t_n^2}{\tau_p^2}} e^{\frac{t_n}{\tau_c}} \sum_{q=n}^{m-1} v(t_q) e^{\frac{t_q}{\tau_s}} + Y_0 v(t_m) \sum_{n=-\infty}^{m} e^{-4ln2\frac{t_n^2}{\tau_p^2}} e^{-\frac{t_m-t_n}{\tau_c}}. \tag{C.10}$$

Realizing that $Y_0 e^{-\frac{t_{m-1}}{\tau_c}} e^{-\frac{t_{m-1}}{\tau_s}} \sum_{n=-\infty}^{m-1} e^{-4ln2\frac{t_n^2}{\tau_p^2}} e^{\frac{t_n}{\tau_c}} \sum_{q=n}^{m-1} v(t_q) e^{\frac{t_q}{\tau_s}} = i_{int}(t_{m-1})$ (compare with Eq. C.7) and the second term in Eq. C.10 represents a voltage multiplied with a conductance brings us to the final expression

$$i_{int}(t_m) = e^{-\frac{\delta t}{\tau_c}} e^{-\frac{\delta t}{\tau_s}} \cdot i_{int}(t_{m-1}) + v(t_m)\cdot g(t_m) \tag{C.11a}$$

$$g(t_m) = A\cdot(\delta t)^2 \frac{q_e^2}{m_{e,GaAs}} \frac{W_z\cdot\Delta}{W_y} \sum_{n=-\infty}^{m} e^{-4ln2\frac{t_n^2}{\tau_p^2}} e^{-\frac{t_m-t_n}{\tau_c}}. \tag{C.11b}$$

D

Mutual Impedance Dependence on Spatial Argument

The following mutual impedance shall be studied in this Appendix

$$\tilde{Z}(x,\omega) = \frac{1}{2\pi}\int_{-\infty}^{\infty} \frac{sinc\left(\frac{k_x\Delta}{2}\right)sinc\left(\frac{k_x\delta x}{2}\right)}{D(k_x,\omega)} e^{-jk_x\cdot x} dk_x \tag{D.1}$$

$$D(k_x,\omega) = \frac{1}{2k_0\zeta_0}\sum_{i=1}^{2}(k_i^2-k_x^2)\,J_0\Big(\frac{W_y}{4}\sqrt{k_i^2-k_x^2}\Big)\,H_0^2\Big(\frac{W_y}{4}\sqrt{k_i^2-k_x^2}\Big), \quad k_i = k_0\sqrt{\varepsilon_{r,i}}. \tag{D.2}$$

When the sign of the spatial argument, x is changed, it becomes

$$\tilde{Z}(-x,\omega) = \frac{1}{2\pi}\int_{-\infty}^{\infty} \frac{sinc\left(\frac{k_x\Delta}{2}\right)sinc\left(\frac{k_x\delta x}{2}\right)}{D(k_x,\omega)} e^{jk_x\cdot x} dk_x. \tag{D.3}$$

Next, a change of variables in the integral shall applied with $k_x' = -k_x$. Implementing this substitution in the exponent, integration bounds and differential of Eq. D.3, together with realizing that $sinc\left(\frac{k_x\Delta}{2}\right) = sinc\left(\frac{-k_x\Delta}{2}\right)$, $sinc\left(\frac{k_x\delta x}{2}\right) = sinc\left(\frac{-k_x\delta x}{2}\right)$ and $D(k_x,\omega) = D(-k_x,\omega)$ gives

$$\begin{aligned}
\tilde{Z}(-x,\omega) &= -\frac{1}{2\pi}\int_{\infty}^{-\infty} \frac{sinc\left(\frac{k_x'\Delta}{2}\right)sinc\left(\frac{k_x'\delta x}{2}\right)}{D(k_x',\omega)} e^{-jk_x'\cdot x} dk_x' \\
&= \frac{1}{2\pi}\int_{-\infty}^{\infty} \frac{sinc\left(\frac{k_x'\Delta}{2}\right)sinc\left(\frac{k_x'\delta x}{2}\right)}{D(k_x',\omega)} e^{-jk_x'\cdot x} dk_x' \\
&= \tilde{Z}(x,\omega) = \tilde{Z}(|x|,\omega).
\end{aligned} \tag{D.4}$$

E

Voltage on the Slot for other Angles of Incidence

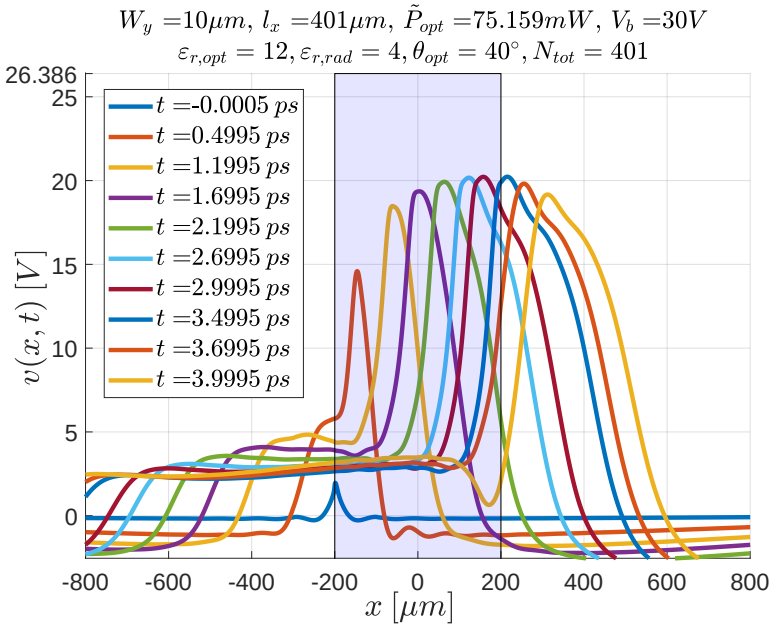

Figure E.1: Voltage as a function of position for different time-instances. The laser has a footprint $l_x = 401\mu m$ and it is incident onto the active region (shaded in the figure) with an angle $\theta_{opt} = 40°$.

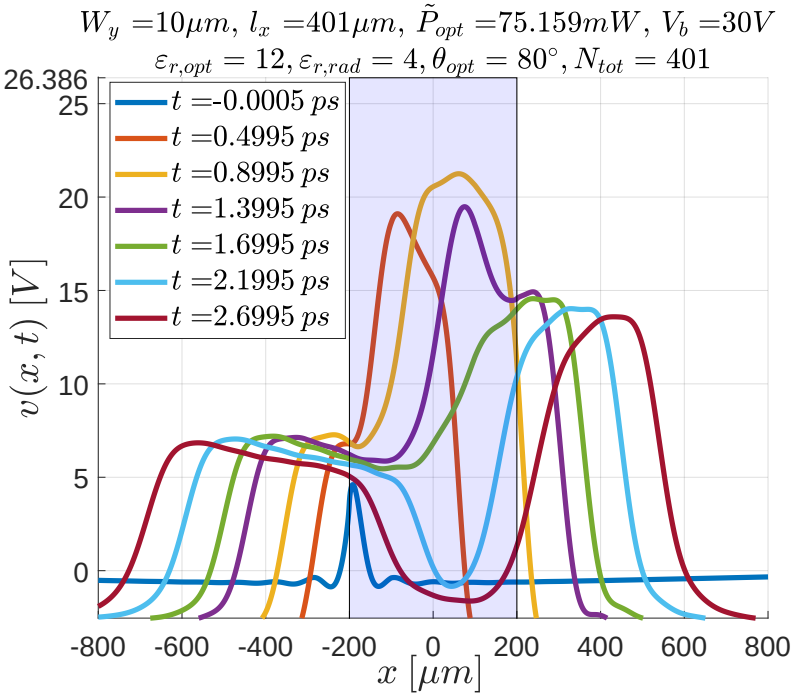

Figure E.2: Voltage as a function of position for different time-instances. The laser has a footprint $l_x = 401\mu m$ and it is incident onto the active region (shaded in the figure) with an angle $\theta_{opt} = 80°$.